UNIVERSITÀ DI PARMA

UNIVERSITA' DEGLI STUDI DI PARMA

DOTTORATO DI RICERCA IN
Fisica

CICLO XXXIV

Photochromic probes for novel photoacoustic microscopy approaches

Coordinatore:
Chiar.mo Prof. Stefano Carretta

Tutore:
Chiar.mo Prof. Cristiano Viappiani
Chiar.mo Dott. Paolo Bianchini

Dottorando: Francesco Garzella

Anni Accademici 2018/2019 – 2020/2021

Ai miei genitori

Acknowledgments

At the end of this long journey, I would like to thank all the people that supported and guided me through this long adventure, from far and from near. I would like to start with my supervisors, who helped me in these three years of scientific and personal growth.
First, I would like to thank Prof. Cristiano Viappiani, professor at the University of Parma, who supervised my work carefully, even if the distance made everything harder. Thanks for proposing me this work to me, and thanks for all the scientific and technical teachings. Thanks for your patience with all my mistakes.
Thanks to Dr. Paolo Bianchini for supervising me during these years at IIT. Thanks for all teachings about everything related to optics, from samples preparation to optical devices and optical alignment. Thanks for all your suggestions on how to deal with the scientific world. And most of all, thanks for pushing me when I was too passive.
Thanks to Prof. Alberto, head of Nanoscopy and NIC@IIT group, for hosting me in one of the best optical microscopy research groups, where I learned all the things I know about microscopy. Thanks for all the human and scientific suggestions and for all the passion you put into this group.
I would like then to thank Dr. Ranieri Bizzari and Dr. Barbara Storti, that helped me in the very first part of my Ph.D. and suggested I join this amazing group.
I would like then to thank all the other people in our group. Thanks to Dr. Salvatore Surdo for helping me to deal with electronics in our “acousto-lab”. Thanks to our technicians, Michele Oneto, Marco Scotto and Mattia Pesce, for solving all my issues and for helping me to survive in the laboratory. Thanks to our computer technician Giorgio Rapallo for helping me with all my computer issues, and thanks to our administrative secretary Manuela Salvatori for her organizational skills and her solution for all my administrative troubles. I know I am terrible with this stuff. Moreover, thanks to all the Ph.D. students and all the post-docs of our group for having a good time together.
When I first arrived in Genova, I felt lost and alone for my first experience far from my hometown, but my life here really improved thanks to all the friends that science brought to me. I would thank my closest friends Alberta, Andrea, Riccardo. You have been a second family to me in these years, and we have been “almost-flat mates” during the pandemic, and I think I could not ask for more. We shared adventures, trips, joys, sorrows, concerns, successes, failures and even food during these intense years, and I thank you for all your love and patience for my continuous flaking. I also thank my other friends in IIT and Mura dello Zerbino: thanks to Silvia, Stefano, Chantal, Sabrina, Fabio, Matteo, Alessandro and Ruggero, for all the time we spent together and for all the parties at Zerbino’s Terrace.
Thanks then to all the people in Pisa who supported me from far. The biggest thanks are

to my beloved parents: Angela and Gianfranco. They are the first people waiting for me at Pisa Centrale and the last I see when I take the train for Genova. They suffered my absence, but they always gave me all their support; when I was sad, when I was happy, when I was tired, they were with me. These years have been an important period of personal growth also for them, and I think I will never thank them enough. Then I would like to thank all my relatives in Pisa for their wise advice and their warm embraces.
Last but not least, thanks to all my affections in Pisa: Lorenzo, Alice, Giovanni, Beatrice, Alberto and Sara. I think that suggestions given by people who know you deeply are important, and you always make me feel your support. You guided me during these three years, accepting my flaking. But you were always happy for your prodigal son to come back.
These three years split between Genova and Pisa have been intense and full of emotions, but all the things I did would not be possible without you.

Table of Contents

Table of Figures

Table of Abbreviations

General Concepts	
1D	One-Dimensional
2D	Two-Dimensional
3D	Three-Dimensional
BW	Beam Waist
CW	Continuous Wave
DoF	Depth-of-Field
EDoF	Extended Depth-of-Field
FoV	Field-of-View
FWHM	Full Width at Half Maximum
NA	Numerical Aperture
NIR	Near Infra-Red
PSF	Point Spread Function
SNR	Signal-to-Noise Ratio
UV	Ultraviolet
Vis	Visible
Photophysical Processes	
1PA/OPA	One-Photon Absorption
2P	Two-Photon
2PA/OPA	Two-Photon Absorption
FRET	Forster Resonance Energy Transfer
IC	Internal Conversion
ISC	Intersystem Crossing
PA	Photoacoustic
Fluorescent Proteins (GFP Derivatives)	
CFP	Cyan Fluorescent Protein
EGFP	Enhanced Fluorescent Protein
FP	Fluorescent Protein
GFP	Green Fluorescent Protein
PAFP	Photoactivable Fluorescent Protein
p-HBI	4-(p-hydroxybenzyliden)-imidazolid-5-one
RFP	Red Fluorescent Protein
rsFP	Reversibly Switchable Fluorescent Protein
YFP	Yellow Fluorescent Protein
Fluorescent Proteins (phytochromes and cyanobacteriochromes)	
BphPs	Bacterial Phytochromes
BV	Biliverdin
CBCR	Cyanobacteriochromes
Cph1s/Cph2s	cyanobacterial phytochromes

Fphs	Fungal phytochromes
GAF	cGMP-specific phosphodiesterases, adenylyl cyclases and FhlA
HKRD	Histidine Kinase-Related Domain
HO1	Heme Oxygenase 1
PAS	Per-Arnt-Sim
PCB	phycocyanobilin
Phys	Plants phytochromes
PVB	phycoviolobilin
PφB	phytochromobilin
Fluorescence Microscopy Techniques	
gSTED	Gated Stimulated Emission Depletion
LSFM	Light-Sheet Fluorescence Microscopy
MELM	Multiplane Encoded Lightsheet Microscopy
PALM	PhotoActivated Photolocalization Microscopy
qOLID	Quantitative Optical Lock-In Detection
RESOLFT	REversible Saturable Optical Fluorescence Transitions
SIM	Structured Illumination Microscopy
SMLM	Single Molecule Localization Methods
SPIM	Selective Plane Illumination Microscope
STED	Stimulated Emission Depletion
STORM	STochastic Optical Reconstruction Microscopy
Acoustic Microscopy Techniques	
2P-PAM	Two-Photon Photoacoustic Microscopy
AR-PAM	Acoustic Resolved Photoacoustic Microscopy
BSI-PAM	Blind Structured Illumination PhotoAcoustic Microscopy
OR-PAM	Optical Resolved Photoacoustic Microscopy
PACT	Photoacoustic Computed Tomography
PAM	Photoacoustic Microscopy
RS-PAM	Reversibly Switchable Photoacoustic Microscopy
SAM	Scanning Acoustic Microscopy
TAUM	Transient Absorption Ultrasound Microscopy
UHF-PAM	Ultra High Frequency Photoacoustic Microscopy
UV-PAM	Ultraviolet Photoacoustic Microscopy
Optical and Acoustic Components	
AMP	Amplifier
AOD	Acousto-Optic Deflector
AOS	Acousto-Optic Scanner
BS	Beam Splitter
DM	Dichroic Mirror
DSO	Digital OSciloscope

EM	Energy Meter
EOM	Electro-Optic Modulator
HWP	Half Waveplate
LIA	Lock-In Amplifier
M	Mirror
OPO	Optical Parametric Oscillator
PC	Personal Computer
PMT	Photon Multiplier Tube
QWP	Quarter Waveplate
SP	Shortpass Filter
TAG Lens	Tunable Acoustic Gradient Lens
UST	Ultrasound Transducer
Chemical and Biological	
BBBN	Brilliant Black BN
DNA	DeoxyriboNucleic Acid
H&E	Hematoxylin and Eosin
HEK	Human Embryonic Kidney
LB	Luria Broth
OD	Optical Density
PBS	Phospate-Buffered Saline
PCR	Polymerase Chain Reaction
RBC	Red Blood Cells
RNA	RiboNucleic Acid

Summary

Optical microscopy provides a vast toolbox of solutions to study essential challenges in life sciences. The light-matter interaction can provide a large amount of information about the biological specimen, e.g., structural, dynamic, chemical and physical properties. Among optical microscopy techniques, fluorescence microscopy is the most widely used due to its intrinsic ability to visualize the molecules of interest with high contrast, high specificity, and high spatial and temporal resolution. In the last decades, research focused on developing advanced super-resolution fluorescence microscopy techniques to overcome the diffraction limit and create images with unprecedented spatial resolution. STED, RESOLFT, SIM, PALM, and STORM brought live-cell imaging at the nanoscale, improving the quality and extending the number of information we can collect.

Nevertheless, fluorescence microscopy suffers intensely from the strong attenuation of light through tissues. As a possible solution, approaches that combine the resolution advantages of light with the penetration depth of sound waves have been proposed in the last years. Techniques based on detecting the acoustic waves generated after light absorption from the sample are called Photoacoustic Microscopies (PAM). PAM has several declinations: Optical Resolved PAM (OR-PAM), Acoustic Resolved PAM (AR-PAM), Ultra High-Frequency PAM (UHF-PAM) and Photoacoustic Computed Tomography (PACT). All these techniques take advantage of the acoustic wave as a detected quantity. As a drawback, they suffer from poor spatial resolution and contrast. This thesis proposes a series of approaches borrowed from fluorescence microscopy devoted to improving the Signal-to-Noise Ratio (SNR) in PAM.

We structured this work in two parts: **Part 1** gives an overview of the theoretical aspects of fluorescence and photoacoustic microscopy. In **Part 2,** we will present experimental applications of the theoretical concepts presented in Part 1.

In the first part of the work, in **Chapter 1**, we report a theoretical overview of the photophysical phenomena due to light-matter interactions focusing on those leading to PA emission. The PA effect is a physical phenomenon based on the emission of sound waves following light absorption in material samples. The photon absorption and subsequent non-radiative relaxation of the excited states of the chromophores rapidly raise the temperature within the sample. The temperature increase induces a volumetric expansion, which generates a pressure wave. Fluorescence emission competes with non-radiative relaxations of the excited states; thus, bright fluorophores are poor sources of photoacoustic signals. **Chapter 2** focuses mainly on the probes studied. The discovery and the development of the Green Fluorescent Protein (GFP) led to the award of the Nobel Prize in Chemistry in 2008 to Osamu Shimomura, Martin Chalfie, and Roger Tsien. The GFP discovery prompted the massive application of genetically encoded probes in fluorescence microscopy and life sciences in general. This chapter presents a systematic review of the Fluorescent Proteins (FPs), starting from the more canonical GFP-like FPs,

massively used in fluorescence microscopy, to more recent proteins of the phytochrome and cyanobacteriochrome families. We classify the FPs on their origin and their chromophores structures. The first group we described are the proteins coming from marine organisms (GFPs and reefGFPs). These proteins are endowed with a chromophore generated in an autocatalytic way and show an absorption mainly in the blue/green region of the visible spectra. We move then our review to proteins coming from plants, fungi and bacteria (phytochromes, cyanobacteriochromes) that show an absorption mainly localized in the green/red and even far-red region of the visible spectra. These proteins also show substantial differences in their chromophore structure compared to GFP derivatives: the protein's backbone binds a derivative of the heme group (BV, PCB, PVB and PϕB) covalently. The combination of GFPs derivatives and phytochromes/cyanobacteriochromes forms a palette of genetically encodable fluorescent probes covering the whole visible spectrum range that widely expands our capability to perform fluorescence microscopy. We then focused on a subgroup of fluorescent proteins, showing reversible switching between two different optical states: these proteins are called reversibly switchable fluorescent proteins (rsFPs). Regarding GFPs derivatives, only a subgroup of these proteins shows photochromism between a dark (non-fluorescent) and a bright (fluorescent) state. We also report the possibility to add punctual mutation capable of making a non-switchable GFP an rsFPs expanding then the palette of genetically encodable probes based on this protein architecture. On the other hand, phytochromes and cyanobacteriochromes show photochromism between two bright states, generally green/red-(far-red)-absorbing. We then comment on the possible application of FPs and rsFPs to life sciences, highlighting their great improvements brought to fluorescence as a reporter gene or for labeling target structures. In **Chapter 3**, we present a review of the canonical approaches in fluorescence microscopy. We start with a theoretical description of fluorescence microscopy and widefield microscopy, the ancestor of all modern microscopy techniques. We moved then to the description of modern microscopy approaches like the confocal microscope, which is the most common architecture for a fluorescence microscope and the more recent light-sheet microscopy, tool-of-choice for studying thick biological samples. As the last point, we review the newest super-resolution techniques overcoming the diffraction limit affecting fluorescence microscopy. We point out that RESOLFT, PALM and qOLID make extensive use of photochromic probes for enhancing resolution and signal-to-noise ratio (SNR). We borrowed the idea from this evidence to introduce photochromic proteins in Photoacoustic Microscopy (PAM) to increase SNR. In **Chapter 4**, we present a systematic review of the state-of-art of PAM. We start from a theoretical description of signal generation in PAM, taking advantage of the concepts exploited in Chapter 1. We highlight the main sources contributing to reducing SNR and contrast, pointing out the thermal origin of the noise. We then characterize the detection system and the lateral resolution: we have systems where the acoustic components drive the lateral resolution (AR-PAM),

or the optical components drive the lateral resolution (OR-PAM). At first glance, we notice that AR-PAM is more suitable to study thick samples with good resolution while OR-PAM provides high resolution in thinner samples showing a tradeoff between lateral resolution and penetration depth. We then review approaches to avoid this tradeoff: we focused mainly on Two-Photon Photoacoustic Microscopy (2P-PAM), which combines the two-photon excitation's advantages in terms of penetration depth whit the same properties in detection offered by photoacoustic microscopy. We complete the description with a review of the main approaches to achieving super-resolution in PAM: we move from non-linear approaches (2P-PAM, PAM nanoscopy) to approaches using structured illumination or photochromic probes (used both to enhance lateral resolution and contrast). In this work, we take advantage of rsFPs to enhance contrast in photoacoustic spectroscopy and microscopy.

The second part of the thesis contains the experimental results. **Chapter 5** explains the engineering, expression, and purification processes of FPs; we focused mainly on two mutants of GFPs and a cyanobacteriochrome. We prepared the GFP's derivatives at the laboratories of the National Enterprise for nanoScience and nanotechnology laboratory in Pisa, under the supervision of Dr.Ranieri Bizzari and Dr.Barbara Storti. We designed two mutants of GFP, including two punctual mutations: one for the photoswitching and one for lowering the fluorescence quantum yield. The cyanobacteriochrome protein (GAF3 from slr1393) was expressed and purified in the group of Dr. Wolfgang Gaertner at the University of Leipzig, Germany. The latter protein was the core of the experiments in **Chapter 6**, where it was studied extensively from a spectroscopic point of view showing better results than GFP derivatives. We characterized GAF3 through optical and photoacoustic spectroscopy. This chapter points out the usefulness of photoacoustic spectroscopy to retrieve time-resolved thermodynamic information from the sample. We designed a 1D experiment to show the contrast enhancement brought by GAF3 in PAM. In **Chapter 7**, we present preliminary results on a more advanced application of PAM for which we built a 2P-PAM setup. The setup shows a high lateral resolution and provides a good penetration depth in samples. We acquired images of a biological sample, showing an improved resolution given by this approach and poor contrast and intense background noise due to the modulated CW excitation. We suggest that the application of rsFPs may improve contrast in 2P-PAM. **Chapter 8** presents an alternative methodology to improve SNR, not involving rsFPs. We show results firstly obtained in optical microscopy. The idea is to parallelize the illumination on a sample to improve the SNR by sharing the noise content among different sample portions. We implement this approach on a light-sheet microscope where we shine the light on different portions of the samples with an encoded parallel illumination pattern. We collect the light coming from different planes by extending the depth-of-field. We reconstruct the single plane after a decoding process. It is crucial to notice that we can vary both encoding sequence and extending depth-of-field methods, adapting to experimental needs. Since the architecture of the light sheet

is similar to the one of the photoacoustic spectroscope previously mentioned, in the last part, we postulate the feasibility of a parallelized photoacoustic spectroscopy to enhance contrast. We propose synthetic data to validate our hypothesis.

PART ONE: THEORETICAL BACKGROUND

1 Light-Matter Interactions

Light plays a crucial role in our everyday life, providing us the information on the surrounding. The first theories on the eye working with the light belong to the ancient Greeks and Pythagoras, which supported the possibility that the eye sends visual rays to explore the surroundings. Nowadays, we can use the dual nature of light, corpuscular or wave, to describe the optical phenomena like reflection, refraction, and absorption that permit us to see the colors. We can describe the behavior of a light wave crossing a material through a set of optical parameters related both to the light itself and the material. If this set of parameters remains constant and independent of the intensity of light, like the phenomena we use to observe, we are working in the field of linear optics. The development of the first laser in the 1960s allowed to confine a high light intensity in a small spot, leading to the study of new optical phenomena. At such high power, the optical parameters are not constant anymore and may become dependent on light intensity: we are in the field of non-linear optics.

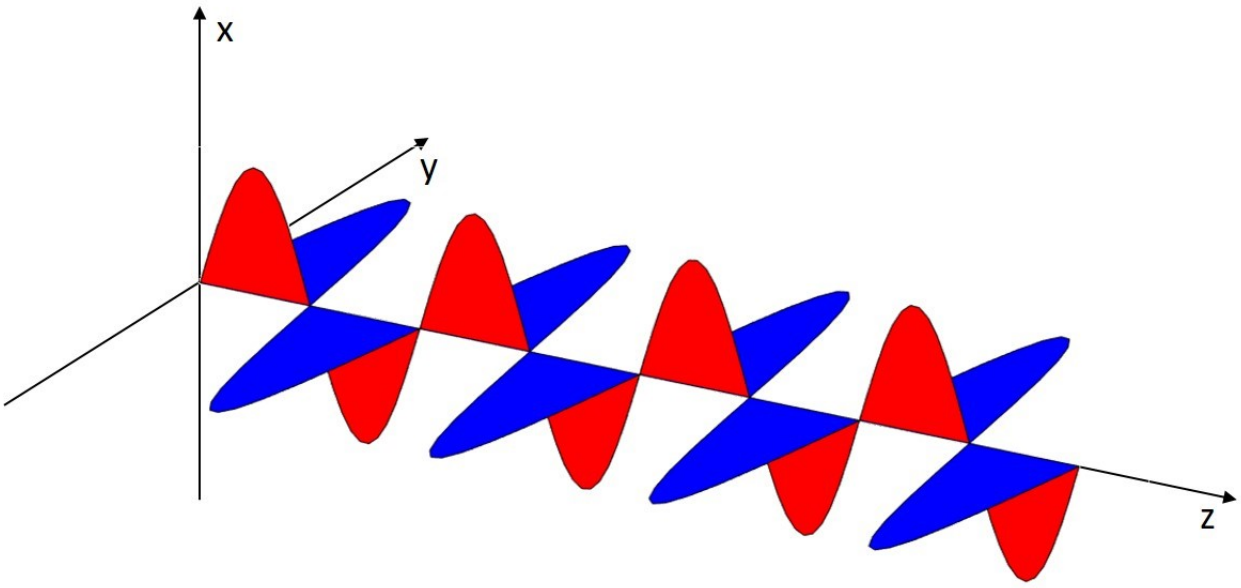

Figure 1.1. The representation of light as an electromagnetic field. In blue is the electric field, and in red is the magnetic one.

To explain both linear and non-linear effects, we start by considering a non-conducting dielectric medium with a total neutral charge. If we apply an oscillating electric field like the electric component of the light $\boldsymbol{E}(\boldsymbol{r},t) = \boldsymbol{E}_0(\boldsymbol{k}\cdot\boldsymbol{r} - \omega t)$(Reported as a blue wave in **Figure 1.1)** we produce deformation through a forced oscillation of the electrons orbitals that leads to the generation of a microscopic dipole moment $\boldsymbol{p}(t) = -e\cdot\boldsymbol{d}(t)$; where $\boldsymbol{E}_0$ is the amplitude, $\boldsymbol{k}$ the wave vector ω the angular frequency, e the charge of the electron, and $\boldsymbol{d}(t)$ is the time-variant displacement from the original position. If the

frequency ω (Notice that $\omega = c/\lambda$ where c is the speed of light in the vacuum and λ the wavelength) of the electric field matches one of the atom's natural frequencies, then we have a resonance phenomenon leading to the absorption of energy by the molecule from the light. The energy absorbed promotes an electron to a quantum state with higher energy (*excited state*) than the previous one (*fundamental state*). The excited state generally has a very short lifetime and many processes, summarized by the Jablonsky diagram (**Figure 1.2**), lead to the depletion of the excited state energy and the restoration of the fundamental state. We can distinguish between non-radiative (e.g., heat release) and radiative (e.g., light emission like fluorescence) decays. There are also processes depleting the energy through long-living paths like inter-system crossing and phosphorescence. The absorption coefficient $\boldsymbol{\alpha(\omega)}$ describes the absorption strength. If ω is not in resonance, the medium will not absorb the energy and, in this case, will be transparent to that radiation that will then propagates through with a lower velocity compared with the free space. The refractive index $\boldsymbol{n(\omega)}$ governs this process and it is intimately linked to the absorption coefficient. The two parameters are the main properties that optically characterize a medium.

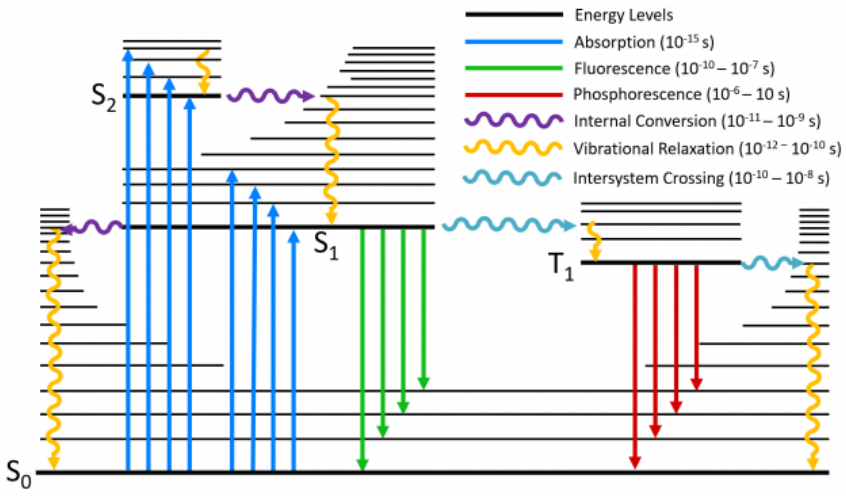

Figure 1.2. Jablonski diagram showing the major transitions between electronic (thick horizontal lines) and vibrational (thin horizontal lines) states. Straight arrows represent the radiative transitions (absorption, fluorescence, and phosphorescence). Wavy arrows represent non-radiative transitions (Vibrational Relaxation, Internal Conversion, Intersystem Crossing). Image adapted from Edinburgh Instruments Ltd, https://www.edinst.com/.

We consider a dielectric medium to understand better how linear and non-linear optics work. An external oscillating electric field would locally generate a dipole that macroscopically will contribute to the vector $\boldsymbol{E}$. We can quantify this process through the vector $\boldsymbol{D}$ that represents the electric field inside the material, written as follows:

$$\boldsymbol{D} = \varepsilon_0 \boldsymbol{E} + \boldsymbol{P}$$

Equation 1.1

Where ε_0 is the electric permittivity of free space, and $\boldsymbol{P}$ is the macroscopic polarization vector of the medium defined as the net average dipole moment per unit of volume:

$$\boldsymbol{P}(t) = N\langle \boldsymbol{p}(t) \rangle$$

Equation 1.2

Where N is the number of macroscopic dipoles per unit of volume, and the brackets are the average over all the dipoles in the medium. By expanding $\boldsymbol{P}$ in powers of the electric field, we can classify linear and non-linear processes through their power-law dependence.

1.1 Linear optics

While applying weak electric fields, we can consider the electron binding potential harmonic and the dipole as a damped harmonic oscillator. Under this condition, the resulting displacement $\boldsymbol{d}(t)$ acts in the same direction of the electric field, and so the polarization could be written as:

$$\boldsymbol{P}(t) = \varepsilon_0 \boldsymbol{\chi}^{(1)} \cdot \boldsymbol{E}$$

Equation 1.3

Where $\boldsymbol{\chi}^{(1)}$ is the linear electric susceptibility tensor of the medium that, for isotropic, is reduced to a scalar quantity $\chi^{(1)}$. The relation $\varepsilon_r = 1 + \chi^{(1)}$ then relates the susceptibility to the relative dielectric constant (ε_r) of the medium. From the following **Equation 1.4**, we can derive both terms as complex and frequency-dependent quantities:

$$\begin{cases} \sqrt{\varepsilon_r(\omega)} = n(\omega) + i\dfrac{\alpha(\omega)}{4\pi} \\ \chi^{(1)} = \chi_R^{(1)} + i\chi_I^{(1)} \end{cases}$$

Equation 1.4

The refractive index $n(\omega)$ governs the real part, which characterizes the dispersive behavior of the material, while the absorption coefficient $\alpha(\omega)$ governs the imaginary part, which represents the absorption properties.

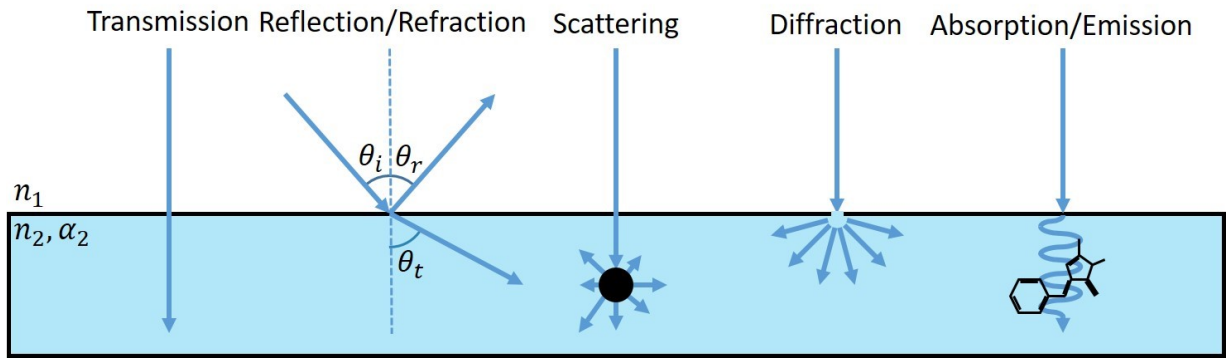

Figure 1.3. Schematic representation of the main linear interactions involving a light beam incident on an optical medium.

As we said at the beginning, linear optics involves the propagation of a weak electromagnetic field through an optical medium. **Figure 1.3** represents these optical processes, categorized as follows:

- Parametric, if the light interacts instantaneously with the matter, without any net transfer of energy, momentum, or angular momentum between the field and the material. This is the case of reflection, refraction, diffraction, and elastic scattering. The real part of the susceptibility rules these processes.
- Non-parametric, if the processes involve a change in quantum states. In this case, examples are absorption, emission, heat release, and inelastic scattering. The imaginary part of the susceptibility rules these processes.

1.1.1 Reflection, Refraction, Diffraction, and Scattering

Reflection is the direction change of a wavefront at an interface between two different media so that the wavefront returns to the medium from which it originated. The law of reflection says that for specular reflection, the angle at which the wave is incident on the surface equals the reflection angle $\Theta_r = \Theta_i$. This behavior is typical of the mirrors.

Refraction is the change in the direction of a wave passing the interface between two media. The portion of light not reflected passes through the material with a velocity $v = c/n\,(\omega)$, where c is the speed of light in the vacuum. Snell's law describes the change in direction due to the change in velocity $n_i \sin(\theta_i) = n_t \sin(\Theta_t)$ where i stands for "incident" and t for "transmitted". Refraction is the typical process associated with the lenses.

Diffraction is the waves bending around the corners of an obstacle or through an aperture into the region of geometrical shadow of the obstacle/aperture. We explain this process as the result of interference of waves since the diffracting object or aperture effectively becomes a secondary source of the propagating wave according to the Huygens-Fresnel

principle. The Diffraction is more pronounced when the size of the obstacle or the crack is comparable to the radiation wavelength. The Diffraction of light by small structures governs the image formation in light microscopy. Diffraction is also the Acousto-Optic Deflectors (AOD) critical process.

Scattering is a term that includes a wide range of physical phenomena where localized non-uniformities force moving particles (like light) to deviate from their original trajector. We classify scattering events on the ratio between entering and scattered wavelengths: if the two-wavelength matches, we are talking about elastic scattering. Otherwise, we are in a regime of inelastic scattering. The first group is the one we are interested in the most, and we can further divide it depending on the dimension α of the scattering center: if $\alpha \gg \lambda$ is called geometric scattering. If $\alpha \sim \lambda$ is called Mie scattering and is dominant in tissues light diffusion, particles of comparable size diffuse the light in the same order as the wavelength of light: cells, nuclei, and organelles all fit in this category. If $\alpha \ll \lambda$ is called Rayleigh scattering (which is responsible for the blue color of the sky). The Rayleigh scattering goes approximately as $1/\lambda^4$ while the Mie Scattering is proportional to the inverse of the wavelength. We will not comment on the inelastic scattering group.

1.1.2 Absorption and Fluorescence

As we said at the beginning of this paragraph, if $\alpha(\omega)$ is non-zero, the electric field of light transfers energy to the electrons and atoms of the medium. In the absorption process, the electromagnetic energy is converted into the system's internal energy. In 1917, in the paper "On the Quantum Theory of Radiation," Albert Einstein proposed a solution for the radiation-matter interaction, starting from the black body radiation, based on three coefficients called "Einstein's phenomenological coefficients".

Let us consider a system having two energy levels, S_0 and S_1 (**Figure 1.2**). Three coefficients describe the induced absorption process (B_{01}), the induced emission process (B_{10}), and the spontaneous emission process (A_{10}). The induced emission process $S_1 \rightarrow S_0$ occurs at *exactly* the same rate as the induced absorption process $S_0 \rightarrow S_1$, so that $B_{10} = B_{01}$. For the absorption process, we define the Lambert-Beer Law to describe the decay of the absorbed light.

$$I(x) = I_0 e^{-\alpha x}$$

Equation 1.5

Where α is the absorption coefficient, x is the optical path, and I_0 is the initial intensity of the light. Let us now consider the population of the two states, N_0 and N_1, respectively. These two numbers will satisfy the Boltzmann Law described in the following **Equation 1.6**.

$$\frac{N_0}{N_1} = e^{-(S_0 - S_1)/kT} = e^{h\nu/kT}$$

Equation 1.6

Where h is the Planck constant, $\nu = 2\pi c/\lambda$ and E_0 and E_1 are the energies of S_0 and S_1, respectively. The rate of absorption from state 0 to state 1 is $N_0 B_{01}\rho(\nu)$, where $\rho(\nu)$ is the energy density incident on the sample at a given frequency. The rate of emission from state 1 to state 0, indeed, is $N_1[A_{10} + B_{10}\rho(\nu)]$. At the equilibrium, these two quantities are equal:

$$\frac{N_0}{N_1} = \frac{B_{10}\rho(\nu) + A_{10}}{B_{01}\rho(\nu)} = 1 + \frac{A_{10}}{B_{10}\rho(\nu)}$$

Equation 1.7

By substituting the density obtained by black body radiation, $\rho(\nu) = 8\pi h\nu^3/(c^3 e^{h\nu/kT} - 1)$ we reduce the **Equation 1.7** in the following form:

$$A_{10} = \frac{8\pi h\nu^3}{c^3} B_{01}$$

Equation 1.8

It is interesting to note that the ratio A_{10}/B_{10} is proportional to the cube of the frequency. For this reason, while in the visible region, essentially all emission is spontaneous for the normal radiation levels, the same is not valid for longer wavelengths (e.g., radiofrequency), where spontaneous emission is negligible.

The coefficient A_{10} summarizes the spontaneous emission, including fluorescence (process at the base of the modern optical microscopy techniques) and phosphorescence. We can go deeper in the analysis, pointing out the main properties of fluorescence. We consider the spontaneous emission independent of the wavelength and, from a kinetic point of view, as a unimolecular process. Given N the number of emitting sources, we can write the following equation:

$$\frac{dN(t)}{dt} = -A_{10}N(t)$$

Equation 1.9

The solution of the **Equation 1.9** leads to the following result:

$$N(t) = N_0 e^{-A_{10}t}$$

Equation 1.10

The constant A_{10} is inversely proportional to the lifetime of the process $\tau_{10} = {A_{10}}^{-1}$. More generally, we can state that a system excited by a photon will drop to the ground state with a certain probability based on the decay rates through several different (radiative or non-radiative) decay pathways, of which fluorescence (A_{10}) is one of the possible ways.

$$N(t) = N_0 e^{-t/\tau}$$

Equation 1.11

We can see that the decay rate of the excited singlet state is proportional to the sum of the rates for all decay pathways $\tau^{-1} = \sum k_i$.

We must comment on two decay pathways: the first one is the internal conversion (IC, **Figure 1.2**), which is a non-radiative transition between two electronic states of the same spin multiplicity. A vibrational relaxation towards the lowest vibrational level of the final electronic state follows the latter process. The excess vibrational energy that can be transferred to the solvent during collisions of the excited molecule with the surrounding solvent molecules is the base of the heating process that we will treat more in detail in **paragraph 1.3**. The second pathway is intersystem crossing (ISC, **Figure 1.2**) between two isoenergetic vibrational states of two electronic levels with different spin multiplicity, like a singlet S_1 to a triplet T_1. Even if the transition ($T_1 \rightarrow S_0$) is forbidden, it is observed for the spin-orbit coupling. In solution at room temperature, non-radiative de-excitation from the triplet state T_1 is predominant over radiative de-excitation called phosphorescence, but at low temperatures or in a rigid medium, we can observe phosphorescence.

1.2 Non-linear optics

The spreading of new powerful sources such as lasers boosted the study of non-linear phenomena in light-matter interaction. Let now consider the equation of the polarization vector. The considerably high oscillation induced by a higher electric field causes a stronger distortion in the electron structure, inducing inharmonic effects. Since the electric fields of focused light are still small compared to interatomic forces, we can expand $\boldsymbol{P}$ to $\boldsymbol{E}$ in a Taylor series:

$$\boldsymbol{P}(t) = \varepsilon_0(\boldsymbol{\chi}^{(1)} \cdot \boldsymbol{E} + \boldsymbol{\chi}^{(2)} \cdot \boldsymbol{E^2} + \boldsymbol{\chi}^{(3)} \cdot \boldsymbol{E^3} + \cdots)$$

Equation 1.12

Here we show the high-order susceptibility tensors $\boldsymbol{\chi}^{(i)}$. Most of the non-linear phenomena involve the second-and the third-order susceptibilities. Generally, the non-linear coefficients are many orders of magnitude smaller than the linear ones, which

means that non-linear optical effects require high incident powers to become relevant. In this work, we will focus only on one non-linear process.

1.2.1 Two-Photon Absorption (2PA)

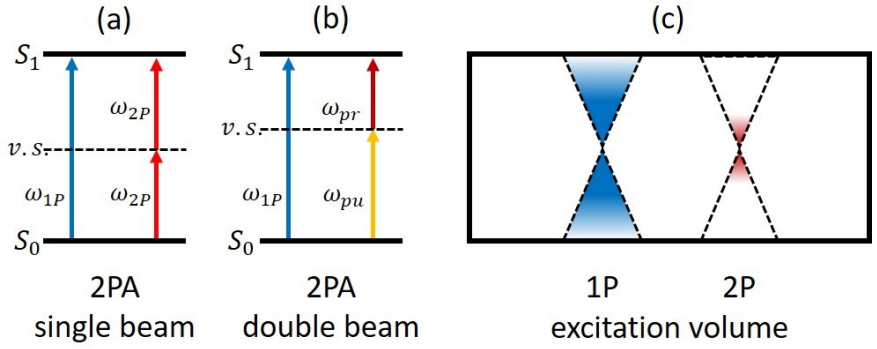

Figure 1.4. The scheme represents the two-photon absorption of two identical wavelengths (a) and two photons with different frequencies (b), in (c) the different excitation volumes in both one-photon (1P) and two-photon (2P) processes.

The process is governed by the imaginary part of the third-order susceptibility $\chi_I^{(3)}$. Two-photon absorption consists of two photons' simultaneous absorption to match the (usual) one-photon transition energy between the ground and the excited state. The "simultaneity" is achieved within a time window of the order of 10^{-16} s (1,2), which is the scale of molecular energy fluctuations (**Figure 1.4**). The system will pass through a virtual intermediate state (*v.s.*). The 2PA could be achieved by absorbing two photons with equal wavelengths, doubling the single photon's energy or through the absorption of two photons with different wavelengths. However, many molecules exhibit deviations from this rule because the selection rules for 2P processes are different from single-photon ones (2). Since the one-photon transition is achieved via the absorption of a UV-VIS photon, it means that longer wavelengths (smaller frequencies) towards the near-infrared (NIR) part of the spectrum need to be used for a 2PA process to occur. As stated in **paragraph 1.1.1**, Mie Scattering in tissues decreases linearly with the increase of the wavelength; for this reason, the use of NIR wavelength has a relevant interest in the study of thick biological samples. As we did in **paragraph 1.1.2**, we can define an absorption law also for the 2PA:

$$I(x) = \frac{I_0}{1 + \sigma x I_0}$$

Equation 1.13

Where σ is now the two-photon absorption coefficient, x is the optical path, and I_0 is the initial intensity of the light.

1.3 Photoacoustic Effect

This phenomenon will play a prominent role in this work. The photoacoustic effect (PA) is a photophysical phenomenon involving the generation of sound waves following light absorption by a sample (3). The PA wave is then quantified by measuring the outcoming sound with an appropriate detector (e.g., ultrasound transducers). As we stated in **paragraph 1.1.2**, many processes concur to deplete the energy of an excited state; internal conversion and vibrational relaxation (**Figure 1.2**) are the two involved in the generation of heat. In the scheme below, we can observe the processes occurring during the photoacoustic generation:

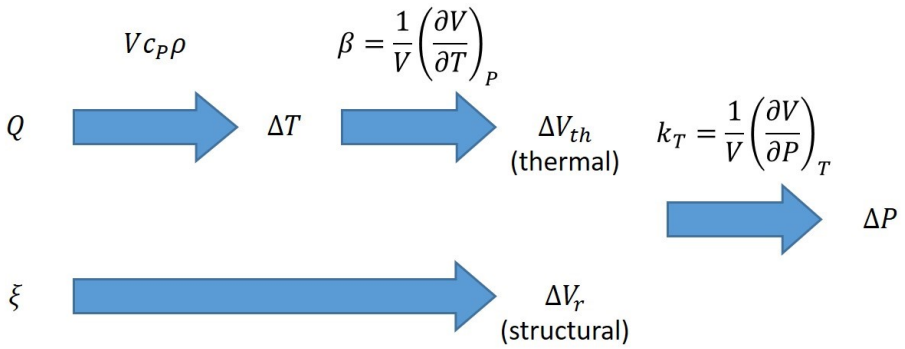

Figure 1.5. Scheme representing the P.A. wave generation. Q is the heating, V is the volume, T is the temperature, c_p is the specific heat at a constant temperature, ρ is the density, β is the isobaric expansion coefficient, and k_T is the isothermal compressibility. ξ stands for all the molecular, atomic, and electronic rearrangements of solute and solvents molecules leading to a structural volume change.

As we can see from **Figure 1.5**, two main processes are leading to PA wave generation:

- The photothermal mechanism consists of three steps: (i) conversion of the absorbed (pulsed or modulated) radiation into heat; (ii) temperature increase through the heat capacity $Vc_p\rho$; (iii) Temperature changes are "translated" to volumetric changes through the isobaric expansion coefficient (β) and finally to pressure changes through the isothermal compressibility (k_T).
- The molecular structural changes may affect the solvent organization, leading to a pressure wave.

The amplitude of the traveling thermal wave decreases strongly (exponentially) along its propagation direction. Since the temperature and pressure changes involved are minute, the standard order of magnitude for the temperature changes, using ordinary light intensities, is about micro to millidegrees and for the resulting pressure changes are about nano-to microbars. The pressure change is typically detected by using an ultrasound

transducer. We will present a detailed review of PA microscopy in **Chapter 4**. We can write the overall pressure variation as follows:

$$\Delta P = -\frac{1}{k_T}\left(\frac{\Delta V}{V}\right) = -\frac{1}{k_T}\left(\frac{\Delta V_{th} + \Delta \mathrm{V}_r}{V}\right)$$

Equation 1.14

In this equation, ΔP is the pressure change, V is the illuminated volume and k_T is the isothermal compressibility. The transducer will measure an electric signal related to the pressure that is linearly related to the number of absorbed photons:

$$n_{abs} = \frac{N_{ph}}{N_A}(1 - 10^{-A})$$

Equation 1.15

Where A is the absorbance of the solution at the wavelength λ, N_A is the Avogadro's constant and N_{ph} the number of incident photons. We can write the total signal as follows:

$$H^S = kn_{abs}^S\left(\alpha\frac{\beta}{C_P\rho}E_\lambda + \Delta V_e\right)$$

Equation 1.16

Here we define $E_\lambda = N_A hc/\lambda$ as the energy of one mole of photons of wavelength λ (=one Einstein), $\alpha = Q/E_\lambda$ as the fraction of the absorbed energy, E_λ released as heat, Q, ΔV_e as the structural volume change per absorbed Einstein, C_P as the specific heat capacity, ρ the density, and β the cubic thermal expansion coefficient. k is an instrumental constant, and its determination plays a crucial role in measuring the other parameters.

We define a class of compounds called "photocalorimetric references" that show the following properties: Photocalorimetric reference compounds are non-fluorescent substances, show no transients with a lifetime longer than a few nanoseconds, are photochemically stable, and are 100% efficient in delivering the absorbed energy to the medium as heat when the excited molecules return to their ground state. In this case, **Equation 1.16** is reduced as follows, neglecting the contribution due to structural volume changes:

$$H^R = kn_{abs}^R\frac{\beta}{C_P\rho}E_\lambda$$

Equation 1.17

These compounds are used to eliminate the instrumental constant by taking the ratio in **Equation 1.18**:

$$H = \frac{H_n^S}{H_n^R} = \alpha + \frac{\Delta V_e}{E_\lambda}\frac{C_P \rho}{\beta}$$

Equation 1.18

For transient species with lifetimes within the pressure integration time, we write the signal as the convolution between the transfer function of the instrument $H_n^R(t)$, obtained through the calorimetric reference and the time-dependent ratio $H(t)$. We write the following equation:

$$H_n^S(t) = \int_0^t H_n^R(t) H(t - t') dt'$$

Equation 1.19

In **paragraph 6.2.3.5**, we will explain experimentally how to retrieve information about the enthalpy changes.

2 The GFP and the autofluorescent proteins

In the last 50 years, bioanalytical techniques have gone deeper into the main biochemical processes occurring inside the cells. The possibility of studying dynamically the molecular processes occurring at the sub-cellular scale represents the new frontier of biochemical analysis. For this reason, imaging techniques with the sub-micrometer resolution are requested. Among these techniques, fluorescence microscopy (**paragraph 3.1**) plays a prominent role thanks to its intrinsic sensitivity, spatial resolution, and biocompatibility due to the emission process. However, fluorescence microscopy requests suitable molecular probes capable of emitting fluorescence even if linked to other macromolecules. From a photophysical point of view, a protein that includes at least one of the three aromatic amino acids (Phenylalanine, Tyrosine, and Tryptophan) characterized by a weak fluorescence emission under UV excitation could be considered (auto)-fluorescent. However, UV excitation is not compatible with biological systems and provides lower penetration depth. There are then proteins based on redox coenzymes NADH/NADPH (ex. 340 nm, em. 460 nm) and FAD (ex. ≈450 nm, em. ≈525 nm) or porphyrin systems (ex. ≈400 nm, em. >600 nm) that emit in the visible region but do not solve the issue of the fluorescent tag (4). In the last 30 years, the discovery of a new class of fluorescent proteins emitting in the visible region of the electromagnetic spectrum not requiring any cofactor has significantly changed the scenario with a new class of probes generically called FP, "fluorescent proteins". These proteins show interesting and complex photochemistry and, through bioengineering processes (that will be further described in **Chapter 5**), could be tailored to several applications, including photoacoustic microscopy (we will describe the principles in **Chapter 6**). This work of thesis will mainly focus on the latter application of FPs.

2.1 The origin of the autofluorescent proteins

In this chapter, we comment on the main classes of fluorescent proteins depending on their original host and the characteristics of their chromophores.

2.1.1 The GFP and the bioluminescence in *Aequorea victoria* and other marine species

Many living organisms show bioluminescence as a defense or a tool to attract partners or quarries; among these bioluminescent organisms, *Aequorea victoria* showed a system of organelles that, in particular conditions, emits green light. Thanks to O. Shimomura (Chemistry Nobel Laureate in 2008 for discovering the GFP), we have been able to retrieve the mechanism of this process (5–7). The primary source of light is a protein called *aequorin* that releases energy as a blue light in the presence of calcium ions, while a green protein modifies its emission spectrum through a resonance transfer of the excitation.

This last protein is called Green Fluorescent Protein (GFP) and is the ancestor of the whole family of FPs. These proteins were first discovered in two Cnidaria classes: *Hydrozoa* and *Anthozoa* (8,9), that use GFP for bioluminescence or fluorescent/non-fluorescent coloring. Recently GFPs from other marine organisms evolutionarily far from *Cnidaria* have been reported. The *Arthropoda* uses fluorescent proteins for choosing the partner.

Color Diversity. The natural diversity of FPs was firstly discovered in non-bioluminescent species of the *Anthozoa* (9), where homologs of the GFP were used as a colorizing system. There were classified five main classes of colors depending on their emission: cyan (CFP), green (GFP), yellow (YFP), orange/red (RFP), and blue-violet non-fluorescent chromoproteins. Nowadays, including artificial mutants, FPs are available in a wide range covering the whole visible spectrum, from ≈450 nm to 650 nm, and the Near Infrared region.

2.1.2 Fluorescent proteins in photosynthetic bacteria

Marine organisms are not the only source of FPs; we can find another class of fluorescent proteins different in structure from GFP derivatives in photosynthetic bacteria. Protein complexes, called phytochromes, binding a linear tetrapyrrole (10), are responsible for photoreception in these latter organisms. Among the photosynthetic bacteria, the cyanobacteria (improperly called blue-green algae) are the most intriguing, giving rise to two classes of fluorescent proteins: the cyanobacterial phytochromes and the cyanobacteriochromes (10). This last group is peculiar to the cyanobacteria and shows different properties than the other bacterial phytochromes. Cyanobacteria *Synechocystis* and *Cyanothece* are essential to model organisms with potential applications in biotechnology.

2.2 Structure and Chromophore of the FPs

In this paragraph, we describe the molecular structure and chromophore of the fluorescent proteins belonging to the GFP-like family and the phytochromes.

2.2.1 Folding and structure stability of GFP

The sequence of the GFP contains 238 amino acids for a molecular weight of 27 kDa. From X-ray diffraction studies of crystallized GFP, this sequence is compacted in a cylindrical structure of 42 Å height and 24 Å diameter containing various secondary structure motifs. This tertiary structure, called β-barrel, derives from a three-dimensional arrangement of eleven strands, antiparallel β-sheets. This tertiary structure is unique for GFP and is represented in **Figure 2.1** (11).

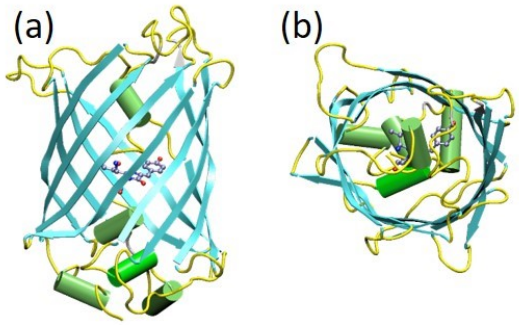

Figure 2.1. The β-barrel tertiary structure of GFP side (**a**) and top-view (**b**). The chromophore, here represented in ball and sticks mode, is located in the core of the protein. Copyright (2003) National Academy of Sciences.

α-helix stretches close to the β-barrel on both sides, while another α-helix stretch crossing the interior of the barrel contains a sequence of three amino acids that form the chromophore upon maturation. We can see from **Figure 2.1** that this arrangement protects the chromophore located in the protein's core from the external solvent and other quenchers like molecular oxygen. The highly compact structure of the protein allows high thermal stability (denaturation occurring at 83°C) and the capability of recovering the tertiary structure after warming/cooling cycles (12).

2.2.2 Structure and autocatalytic formation of GFP and GFP-like chromophore

We will distinguish between proteins emitting in the region of the spectrum going from cyan to green/yellow (480-560 nm) that own chromophores chemically identical to the original GFP's one and proteins emitting in the region of the spectrum going from yellow to red (560-700 nm) that undergo an extra step during the maturation process. We briefly commented on this last class since yellow-red GFPs will not be central in this work.

Wilde-Type GFP. The chromophore of the original GFP (wild-type GFP or wtGFP) is a 4-(p-hydroxybenzyliden)-imidazolid-5-one (p-HBI) and is formed after the cyclization of three adjacent amino acids: Ser65, Tyr66, Gly67. It is demonstrated that the expression of the gene coding for GFP in other organisms leads to fluorescence, meaning that no cofactor, apart from oxygen, is requested for the complete maturation of the chromophore, being the core of the unique feature of this protein. The protein formation mechanism is described in (13) and is shown in **Figure 2.2**. After the β-barrel formation, the imidazolidone (the five-term ring) is formed by the nucleophilic attack of Gly67 on the carbonyl of Ser65 following dehydration. After, the molecular oxygen dehydrogenates the β-carbon of Tyr66, leading to the formation of the conjugated system responsible for the absorption and the fluorescence in the visible.

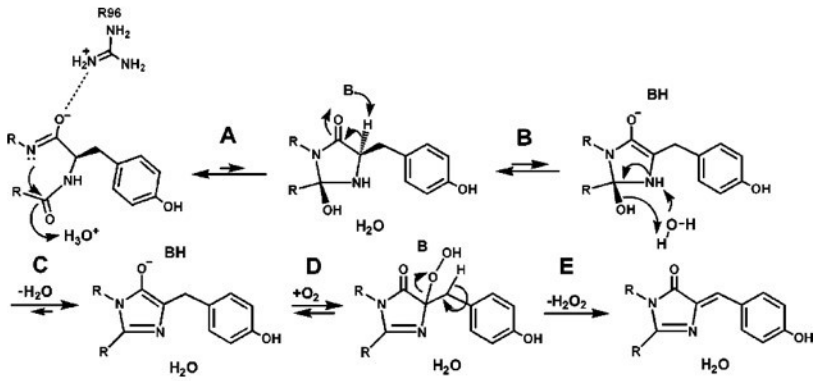

Figure 2.2. Biosynthetic scheme for GFP chromophore's formation. (**A**) Cyclization of the backbone through a nucleophilic attack by nitrogen of Gly67 to the carbonyl of Ser65. (**B**) Deprotonation of the α-carbon of Tyr66 and enolate's formation. (**C**) Reversibly dehydration of the main chain. Arg96 stabilizes both this and the previous intermediate. (**D**) Addition of oxygen and formation of the adduct with hydroperoxide. (**E**) Oxidation by deprotonation of the β-carbon of Tyr66 and formation of hydrogen peroxide. Image adapted from (11). Copyright (2003) National Academy of Sciences.

It is important to notice that if we denature the β-barrel after chromophore formation, we lose the fluorescence, while a subsequent renaturation will restore the original condition. That means that the β-barrel is necessary to have fluorescence, so the tertiary structure must be complete. It is possible to operate punctual mutation to modulate the properties of the protein and tag the protein to other structures not compromising correct functioning. Among the three functional amino acids, only Gly67 is essential since the nucleophile needs space and flexibility to work. Ser65 could be variously substituted (Thr65 instead of Ser65 brings to the Enhanced GFP, EGFP), while Tyr66 could be substituted with aromatic amino acids, leading to a change in color (Y66W, Trp instead of Tyr, brings to aquamarine, cyan fluorescent protein (14). A group of mutations across the backbone has different features to the protein, preserving the primary structure's effectiveness.

Reef GFP. In the second class of GFP-like FPs, we have proteins belonging to organisms mainly coming from the coral reef that is sometimes indicated as reefGFP. In these proteins, after the chromophore's maturation, an oxidation process forms an acilimine. The protein DsRed ($\lambda^{max} = 583\ nm$, **Figure 2.3**, **IV**) was the first protein undergoing these processes discovered. Here dehydrogenation occurs at α-carbon of Gln66 (in DsRed, position 66 corresponds to position 65 of GFP). The extended conjugation onto the backbone redshift the emission of the protein. The acilimine could undergo other reactions, giving rise to other classes of chromophores. In zFP538 ($\lambda^{max} = 538\ nm$, **Figure 2.3**), the first amino acid of the chromophore (lysine) undergoes a cyclization onto

its α-carbon. In mOrange ($\lambda^{max} = 562\ nm$) threonine cyclizes with the carbonyl forming a ring (**Figure 2.3**, **VIII**). In Kaede protein, irreversible photoconversion cleavages the chromophore generating a new red-emitting one (**Figure 2.3**, **V**). In protein KFP (kindling fluorescent protein, asFP595), the autocatalytic hydrolysis forms a ketone (**Figure 2.3**, **VII**). **Figure 2.3** reports a schematic representation of the main processes described in reference (13).

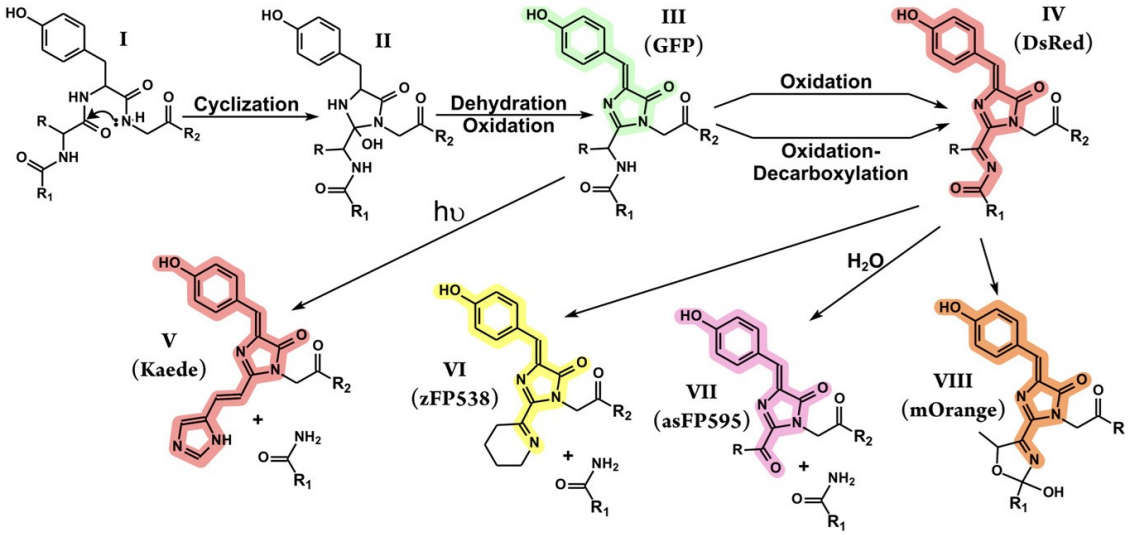

Figure 2.3. The chromophores in FPs and their synthetic steps. The π-conjugation is reported in color. Reprinted from Chemistry & Biology, Vol 15, Alexey A. Pakhomov, Vladimir I. Martynov, GFP Family: Structural Insights into Spectral Tuning, Pages No. (13), Copyright (2008), with permission from Elsevier.

2.2.3 Proteins binding heme derivatives

As we mentioned in **paragraph 2.1.2**, we will comment on another group of fluorescent proteins having different origins and spectral/structural properties than GFPs. These proteins bind a tetrapyrrole derivative (bilin) as a chromophore, and we refer to them as "phytochromes". They are a widespread family of red/far-red responsive photoreceptors first discovered in plants in 1959 (15), where they constitute one of the three main classes of photomorphogenesis regulators (16). Phytochromes bind covalently bilin chromophores that enable photoconversion between red-absorbing (Pr) and far-red-absorbing (Pfr) forms through *cis-trans* isomerization. In plants, phytochromes measure the ratio of red light and far-red light, allowing the plant to assess the quantity of photosynthetically active light (17). New members of the phytochromes family were then discovered in fungi, bacteria and cyanobacteria, demonstrating that these proteins are not limited to photosynthetic organisms (18). Generally, the cofactor is produced from the heme group through enzymatic processes and is covalently acquired by the backbone

at a later stage, differently from the autocatalytic formation of p-HBI in GFPs. **Figure 2.4** (Adapted from reference (10)) shows some of the main chromophores and their color.

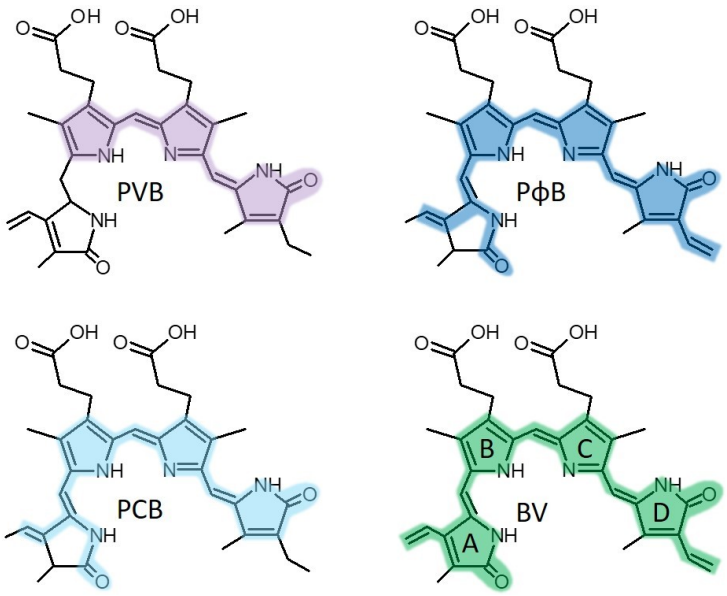

Figure 2.4. Four different kinds of tetrapyrrole chromophores: phycoviolobilin (**PVB**), phycocyanobilin (**PCB**), phytochromobilin (**PϕB**) and biliverdin (**BV**). The chromophores' colors highlight conjugated regions.

The architecture of the phytochromes is usually modular and is made of a PAS-GAF-PHY module for the N-terminal photosensory core (19). The first part of the backbone is a PAS domain whose name belongs to the first proteins in which this motif was discovered (**P**er-**A**rnt-**S**im). The PAS domain acts as a molecular sensor, whereby small molecules and other proteins associate via binding of the PAS domain (20–22). Due to this sensing capability, the PAS domain is also a common motif found in signaling proteins, where it works as a signaling sensor (23,24). The GAF domain is the sole portion of the molecules that bind the chromophore. This motif's name comes from the three first proteins in which it was discovered: c**G**MP-specific phosphodiesterases, **a**denylyl cyclases and **F**hlA. The last domain, PHY (phytochrome-specific domain), connects the chromophore binding domains PAS-GAF with the output kinase (25) and helps the photoconversion. The photochromic N-terminal module is typically combined with a C-terminal **h**istidine **k**inase-**r**elated **d**omain (HKRD). Interestingly, PAS and GAF domains can be present in other signaling domains like Lov domains of the phototropin (23,27,28), while GAF domains take

part in cyclic nucleotides regulation in cyanobacteria and even mammals. **Figure 2.5** reports the canonical structure of plants' phytochrome (26).

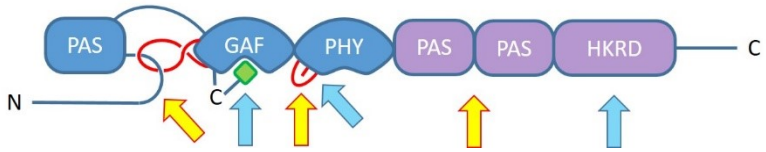

Figure 2.5. Structural domains of a plant phytochrome and their role in perceiving environmental signals and downstream signals. In lavender, the C-terminal module is involved in PIF binding, photo body formation and nuclear localization. In blue, the Photosensory Module is involved in light perception, signal transduction and interaction with the chromophore (BV, represented by the green square). The cyan arrows indicated the portions of the phytochrome dedicated to photoconversion, and the yellow ones the portion dedicated to thermal reversion. In red are represented the knot lasso of the GAF domain and the hairpin of the PHY domain.

In general, plants phytochromes (Phys), fungal phytochromes (Fphs), bacterial phytochromes (BphPs) and cyanobacterial phytochromes (Cph1s/Cph2s) show similarities in their modular architecture. Phys possess two additional PAS domains constituting the part of the photoreceptor involved in PIF (Phytochrome Interacting Factors) binding, while the first portion (PAS-GAF-PHY) binds the bilin chromophore. As we will see, bacterial and cyanobacterial phytochromes show slight differences. The nature of the chromophores depends on the specimen: Phys bind PϕB, Cph1s and Cph2s bind PCB, while BphPs and Fphs bind BV.

2.2.3.1 Phytochromes binding biliverdin

These are the most common proteins among the Phytochromes. The crystal structure of BrBphP and RpBphP3 shows that the biliverdin is embedded in the GAF domain, while a Cys residue preceding the PAS domain ligates the pyrrole ring A of biliverdin (BV). As a main difference, the Phytochromes from plants (Phys) own another Cys residue that binds the phytochromobilin (10). The phytochrome GAF domain shows a *knot lasso* sequence, part of a unique figure-of-eight knot that connects PAS and GAF domains in Phys (**Figure 2.5**) and BphPs. Moreover, in BrBphP and RpBphP3, the 3D structure reveals that the three pyrrole rings A, B and C of BV (**Figure 2.4**, **BV**) are connected to the GAF domain by a hydrogen bond via a specific water molecule and an aspartate residue. The co-planarity of the three rings is critical for the absorption of the phytochrome in the red/far-red light region, while a possible distortion would be responsible for some variation in spectral properties.

2.2.3.2 Phytochromes binding phycocyanobilin

As we mentioned, phycocyanobilin (PCB) binding phytochromes are mainly found in cyanobacteria. The PCB is a derivative of the heme group, generated by the following

mechanism: Heme oxygenase 1 (HO1) catalyzes stereospecific cleavage of heme to yield BV IXα that PCB:ferredoxin oxidoreductase further reduces to phycocyanobilin (**Figure 2.6**, adapted from (27)).

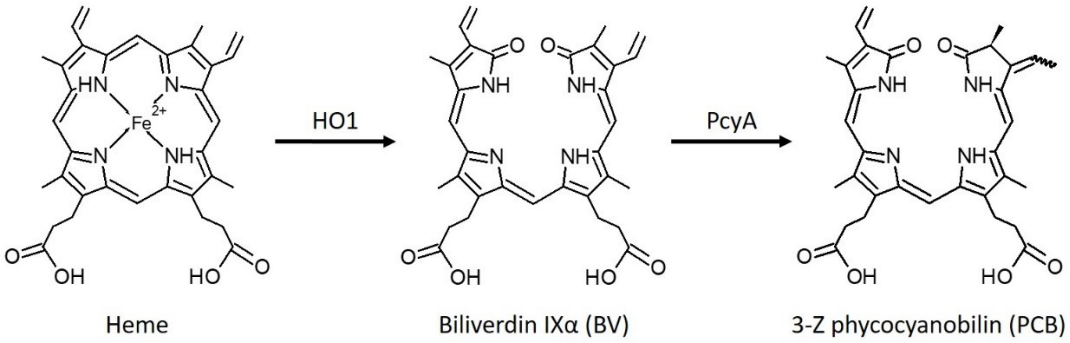

Figure 2.6. Pathway of PCB biosynthesis in cyanobacteria. Heme oxygenase 1 (HO1) catalyzes stereospecific cleavage of heme to yield biliverdin IXα that PCB: ferredoxin oxidoreductase further reduces to PCB. Image adapted from reference (27).

Here we must specify a distinction between three main groups of phytochromes based on the 3D structure: cyanobacterial phytochromes knotted (Cph1s) and knotless (Cph2s) and cyanobacteriochromes (CBCR).

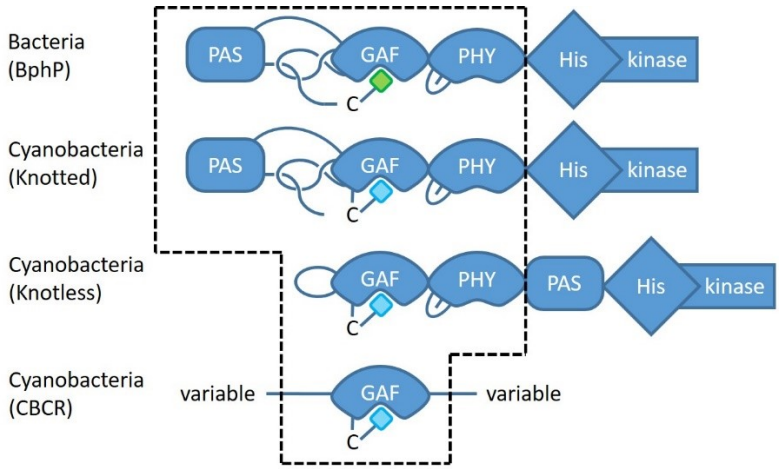

Figure 2.7. Representative architectures for bacterial phytochromes with histidine kinase domain output from different lineages. The tetrapyrrole chromophore is shown as a green (BV) or cyan (PCB) polygon. Protein domains are shown as carton shapes. The region highlighted by dashed lines represents the portion of the phytochrome involved in light perception. Image adapted from (28)

For their structure, Cph1s represent the prokaryotic phytochromes with the greatest similarity to plant phytochromes. As a general feature, we can see that the Cys residual binding the PCB in Cph1s (and Cph2s) is located directly on the GAF domain (**Figure 2.7**),

while in BphPs, BV is bound to the PAS domain, a fact that constitutes the main difference with other bacterial phytochromes. BphPs and Cph1s show high similarities in the *knot lasso* sequence and the PAS domain, preserved in both species. In the knotless cyanobacterial phytochromes (Cph2s), there is a complete lack of the PAS domain and the *lasso* sequence present in Cph1s. The third class of cyanobacterial phytochromes, called cyanobacteriochromes, is a far relative of the other phytochromes. The main feature of this protein is the complete lack of the PHY domain; only a GAF domain binding PCB is present. In this class of protein, the lasso sequence present in the bacterial one is absent and is consistent with the absence of the PAS domain. Among the cyanobacteriochromes, the one that plays a prominent role in this work is the third GAF domain (GAF3) from *Synechocystis* PCC6803. This molecule has a size of 155 amino acids, slightly smaller than GFPs (29). Recently some cyanobacteriochromes expressing BV have been reported as a source of FPs in the NIR region (30).

2.3 Photochromic proteins

Recently, the photoactivable proteins family, referred to as PAFPs (Photoactivable Fluorescent Proteins), has attracted high interest. The PAFPs own two or more stable optical states, where transitions can be induced reversibly or irreversibly upon appropriate light irradiation (31–33). The most interesting among these are the reversibly switchable Fluorescent Proteins (rsFPs), also called "photochromic proteins". These proteins mainly work on the *cis-trans* photoisomerization of the chromophore, inducing a structural change of the protein conformation leading to changes in spectral properties (**Figure 2.9**). In GFP-like proteins, the chromophore (p-HBI) generally switches between a cis-neutral and a trans-anionic form (**Figure 2.8**, **a**); punctual mutations can modify the spectral and switching properties of the proteins, also affecting the pKa of the cis/trans-forms. This latter is the case of the proteins Padron and Dronpa (34). Padron is obtained from Dronpa by adding V167G and M159Y mutations that give the protein opposite properties compared to the parental one: while Dronpa is fluorescent (*on*) in the rest state, Padron is not fluorescent (*off*) in the rest state (respectively negative and positive switching). For these proteins, irradiation with appropriate wavelengths (405/488 nm) raises a non-fluorescent band centered at 400 nm. The fluorescent band centered on 490 nm can then be restored. Mutation Y66W in protein Aquamarine (14) strongly changes the spectral properties: in this case, the illumination with 405/448 nm does not rise a second absorption band, but it modifies the only main absorption band. As we will see in Absorption/Fluorescence Spectra mutation Y145W shows a similar effect. Storti *et al*. (35) demonstrated that the mutation E222Q induces a photochromic behavior between an *off*-state and an *on*-state by modulating the chromophore's electronic properties via H-bonds that stabilize largely twisted structures around the double bond of p-HBI.

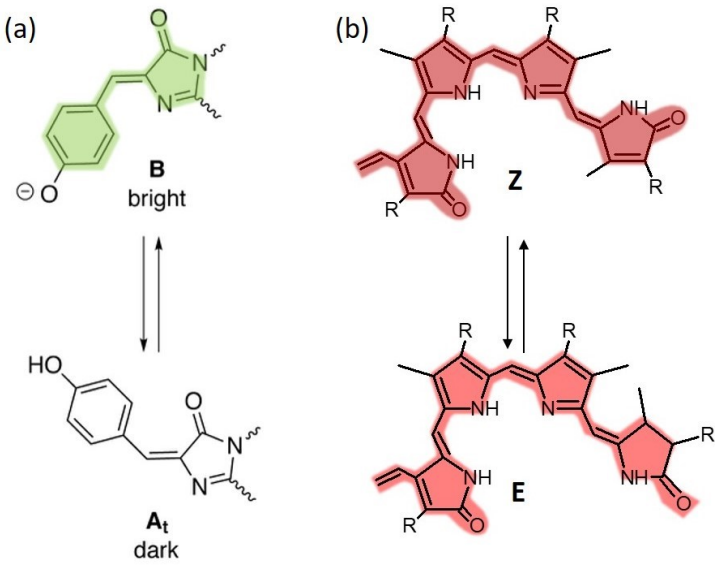

Figure 2.8. Schematic comparison of the cis-trans isomerization of (**a**) p-HBI (image adapted from (35)) and (**b**) PCB. Chromophores' color highlight conjugated regions.

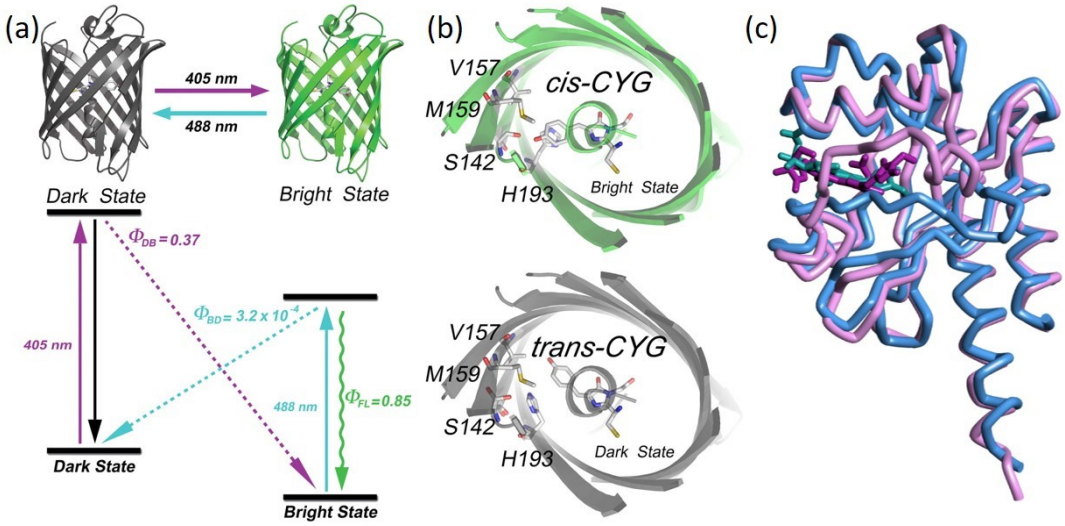

Figure 2.9. The figure shows two different photochromic proteins. (**a**) Dronpa protein from reference (36). The proteins show a photochromism *off→on*. The dark state is shown in gray (PDB: 2POX) and the bright one in green (PDB: 2IOV). Below we show the photoswitching scheme. (**b**) Representative views of the chromophore and its nearby residues. The CYG chromophore in Dronpa adapts distinct *cis* and *trans* conformations in the bright (*Upper*) and dark state (*Lower*), respectively. (**c**) Superposition of the three-dimensional structures of the parental state ($GAF3_R$, tube, light blue, PDB: 5dfx)(37) and the photoproduct state ($GAF3_G$, tube, magenta, PDB: 5m82)(37) of the cyanobacteriochrome GAF3 from Slr1393 of Synechocystis sp. PCC6803 (in vivo assembled protein/chromophore). The phycocyanobilin chromophore is shown as sticks in cyan for $GAF3_R$ and purple for $GAF3_G$.

Chromophores based on bilin derivatives show isomerization at carbon 15 (15Z-to-15E). The Cys binding C10 seems to be not a prerequisite for photoconversion. **Figure 2.8** (**b**) reports the isomerization scheme for PCB. Most phytochromes show a photochromism between two optical states, both fluorescent in red/far-red, while the GFP-like proteins cover a more comprehensive range of the visible spectrum but often have only one fluorescent state (off→on). In **Figure 2.9** is possible to see the structural changes induced on the proteic backbone by chromophore's isomerization for a GFP-like protein (**b**, Dronpa) and a bacterial phytochrome domain (**c**, GAF3). **Figure 2.9** (**a**) shows a canonical photoconversion diagram for a GFP-like protein (Dronpa).

2.4 Application of the FPs

The GFP and its mutants have been widely used as non-invasive intracellular probes to study processes related to proteins expression, localization and interactions from their first discovery.

2.4.1 Protein tagging

Protein tagging is probably the most used application of the FPs. Nowadays, many studies aim to develop intracellular genetically encoded probes to determine analytes concentrations (Ca^{2+}, pH, Cl^-) or to track enzymatic activity. To this aim, a cell line or a transgenic animal is transformed to express fluorescent probes, targeting a specific organelle not achievable by exogenous labels. This approach uses FPs, where the fluorescence is sensitive to the environment. Other possibilities involve the application of FPs fused to a protein able to detect the phenomenon of interest; the structural changes of the target protein modify the emission of the FP.

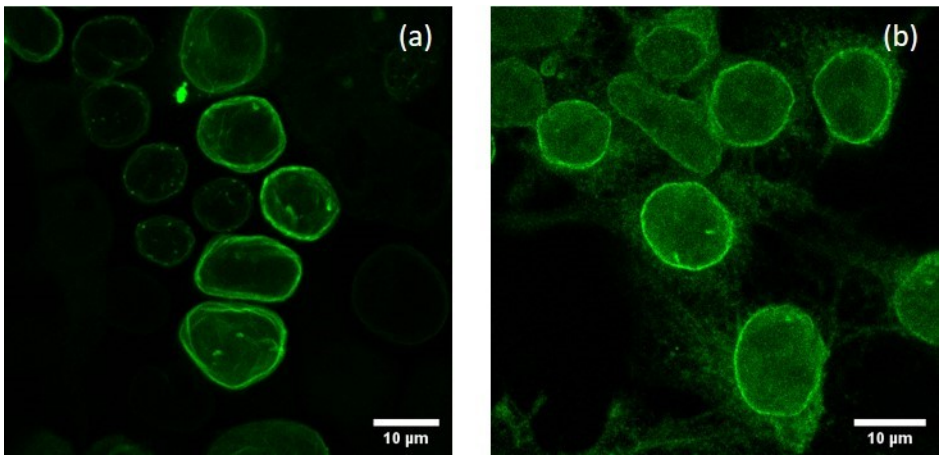

Figure 2.10. (**a**) HEK cells expressing EGFP-Δ50 lamin-A (the mutation associated with Progeria). (b) HEK cell with lamin-A stained through Syto staining. Both images are acquired using a confocal microscope (LEICA SP5) and edited through Fiji imaging processing package (38).

From **Figure 2.10** is evident that the genetically encoded label of the FP is more precise and localized than the one provided by other approaches, making protein tagging a good choice for investigating cellular processes. **Figure 2.10** compares, through a fluorescent tag, the features of the nuclear membrane in cells affected (**a**) or not (**b**) by Progeria disease. **Figure 2.10** highlights that the nuclear membrane of Progeria cells (**a**) appears stiffer than the other cells. In general, due to the reduced dimensions of the tagging FP, the fusion proteins do not undergo any loss of functionality. Nevertheless, one should evaluate each case of FP's fusion reminding that one important aspect is that the FP should be monomeric.

2.4.2 Detection of protein-protein interaction

Since the resolution of diffraction-limited optical microscopes is too low to indicate if two tagged proteins are interacting or co-localizing new methods based on Förster Resonance Energy Transfer (FRET) are used. FRET is a spectroscopic technique, easily implementable in fluorescence microscopy, which is ideally suited to study biomolecular interactions in solution, live cells, and tissues (39). FRET has its basis on the non-radiative transfer of energy from an excited molecular fluorophore (donor, D) to a chromophore (acceptor, A) via long-range dipole-dipole coupling (40). In most applications, also the acceptor is fluorescent, although it need not be so for FRET to occur. According to Förster's theory (40,41), the efficiency E of FRET is inversely proportional to the sixth power of the donor-acceptor separation (r) according to:

$$E = \frac{R_0^6}{R_0^6 + r^6}$$

Equation 2.1

where R_0 is a parameter named Förster's radius, which accounts for all the other contributions to the energy transfer process and represents the distance between donor and acceptor at which FRET's efficiency is equal to 0.5. Among these stands the so-called overlap integral, i.e., the spectral integral of the product of donor's emission and acceptor's absorption weighted by the fourth power of wavelength (40). FRET detects the interaction between fluorophores when they are close enough (<10 nm). It is interesting to notice that the original GFP is involved in a FRET mechanism in *Aequorea Victoria*. This method is helpful to track interactions between proteins tagged with FPs of two different colors and monitor the variation of the ratio of the two emissions. This approach is used to study protein-protein interactions and design intracellular genetically encoded probes.

2.4.3 Application of rsFPs

The application of rsFPs in microscopy is another crucial point of this work. There are mainly two ways to use these proteins: (i) they can be exploited to strongly improve the imaging contrast-to-noise ratio due to modulation and locked-in detection, and (ii) they can be employed to boost spatial resolution (42). For this latter application, we refer to **paragraph 3.4**. For what concerns the first point, each rsFPs is studied as a modulable signal over a constant fluorescent and consequently filterable background. Besides the classical applications of rsPFs in the super-resolution field, rsFPs can be usefully applied to Quantitative Optical Lock-In Detection (qOLID) (43). In short, qOLID quantitatively separates the modulated and the non-modulated signals deriving from photochromic and non-photochromic fluorophores emitting in the same spectral range, allowing for quantitative interpretation of overlapping signals (44). For this reason, qOLID has been applied to photochromic FRET (pcFRET) in a relevant imaging technique to probe the formation of protein complexes in vivo.

2.4.4 Cyanobacteriochromes as a source of fluorescent probes

The previous applications (protein tagging and dynamics) were made possible by discovering the GFP and the GFP-like proteins. In general, for the choice of FP for a specific application, there are many parameters to consider, such as molecular weight, oligomeric state, availability of chromophore and tissue penetration of exciting and emitted light. As stated in **paragraph 1.1.1**, visible light suffers from a higher tissue scattering and a competitive absorption of many components like hemoglobin and melanin. This issue restricts the application of GFP-like FPs in tissue (45) due to their absorption/emission mainly localized in the visible region. Various natural photoreceptors were employed as molecular templates for FP engineering to overcome these limitations. The photoreceptor-derived FPs have been successfully applied to report dynamics and interaction signaling molecules in time and space (46). The far-red to near-infrared (NIR) light within the 650-900 nm region is the "NIR tissue transparency window" and penetrates significantly deeper into tissues. Although some GFP-like FPs exhibit substantially red-shifted emission, their excitation light is still strongly absorbed by tissues. One way to overcome that is to use two-photon excitation (**paragraph 1.1.2**). Many bacterial phytochromes (BphPs) show emission/absorption lying in NIR (47–49), complementing the existing palette of GFP-like proteins.

3 Optical Microscopy

The possibility of studying small size objects is the key to the comprehension of most biological processes. The first microscope is ascribed to the Dutch draper Antoni Philips von Leeuwenhoek around 1670s. A single lens made of transparent glass is interposed between the eye and the object. The light comes from the object and is collected, forming an enlarged virtual image projected onto the retina according to the rules of geometrical optics. In the 17th century, mainly thanks to the work of the Dutch spectacle-makers Hans and Zacharias Janssen, the English natural philosopher Robert Hooke and the Italian astronomer Galileo Galilei further improvements in the architecture of the microscope have been added: the objective that is the optical element gathering and focusing the light from the object producing the real image. One of the fundamental properties of the objective is the Numerical Aperture (NA), defined as $NA = nsin\alpha$, where n is the refractive index of the medium and α is the maximal half-angle of the cone of light that can enter or exit the lens. A high NA means that the objective can focus and collect light efficiently. The second addition was the eyepiece (or ocular lens), so named because it is usually the closest lens to the eye, is placed in the focal point of the objective to magnify the image. The amount of magnification depends on the objective focal length. The total magnification is given by $M_{tot} = M_{obj} \cdot M_{eye}$. This architecture was preserved for centuries, with the leading innovation mainly concerning the mechanical part of the instrument. From the first half of the 19th century, improvements raised exponentially, leading to the current microscopy techniques. Improvements in the optical components permitted the correction of the optical aberrations. Meaningful improvements were made to the light sources (lamps and lasers) and the detection systems (cameras, photosensitive devices). Among these, one of the major advancements was fluorescence microscopy, which significantly expanded the application of optical microscopy and led to the development of super-resolution microscopy.

3.1 Fluorescence Microscopy

The history of modern fluorescence microscopy started in 1845 when Sir Frederik William Herschel first described the process. He noticed that a quinine sulfate solution (e.g., tonic water) exhibits a “vivid and beautiful celestial blue color” when illuminated and observed under certain incidences of UV light coming from sunlight (50). Starting from this evidence, the British Scientist Sir George G. Stokes observed that fluorescence emission has a longer wavelength than the UV light that originally excited the object (Stokes Shift, red-shift). The first commercial fluorescence microscope development is due by Carl Zeiss and Carl Reichert companies (51–53). Ellinger and Hirt that in the early 1940s, made another important step forward in achieving fluorescence labeling. They devised

“intravital microscopes” to examine thick and opaque living organisms by implementing incident instead of transmitted light. They implemented their setup using a UV-light source and interposed filters between objective and eyepiece, reflecting the UV rays and transmitting the red-shifted fluorescence. They treated the samples, generally living organisms, with fluorescent substances to have the source of light emission inside the sample; this was the first attempt at fluorescence labeling. The ways of labeling a specimen widely expanded over the next decades. In the 1940s, Coons *et al*. developed fluorescent antibody labeling (direct immunofluorescence), directly testing a specific antigen's presence (54). As we mentioned in **Chapter 2**, the cloning of GFP (55,56) and the development of spectral variants (57) added another important element to the toolbox of fluorescent labels. In the early 2000s, the development of modern immunostaining (indirect immunostaining) occurred. Fritschy *et al*. (58) used an unlabeled primary antibody, specifically binding the target antigen. A secondary antibody carrying the fluorophore then recognized the primary antibody and bound to it. The indirect immunostaining protocol is more complex than the direct one, but it allows more flexibility since we can use various secondary antibodies and detection techniques for a given primary antibody. Generally, fluorescence labeling of target cellular structures allows significant background noise reduction, bringing out the object of interest; due to its intrinsic sensitivity and specificity (59), fluorescence microscopy provides a high **S**ignal-to-**N**oise **R**atio (**SNR**), making this microscopy approach successful. The simplest fluorescence microscope is the so-called widefield, where the entire specimen of interest is exposed to the light source, with the resulting light forming an image that can be further viewed either by the observer or a camera. **Figure 3.2** (**a**) shows a typical widefield architecture that can be upright or inverted depending on the illumination coming below or above. If the excitation and the emitted light share the same objective lens, we use the term “Epi-Fluorescence”. In this case, light travels from the light source through a set of filters and through a dichromatic mirror with the shorter wavelength light (excitation) reflected onto the samples. The longer wavelength light emitted from the samples then travels back passing the dichroic mirror being imaged by the eyepiece or collected by a camera. Epi-fluorescence microscopes represents the majority of available microscopes. Widefield microscopy ensures high-speed performances and good spatial resolution while it suffers from the out-of-focus fluorescence background (60). It results in images showing poor contrast between optical planes, with this phenomenon becoming severe in thick samples (61). To overcome these limitations, we can use contrast methods, including differential interference contrast (DIC) Microscopy and phase contrast microscopy in conjunction with widefield fluorescence microscopy. The introduction of fluorescence confocal microscopy addressed the poor SNR issue of the latter method. This

technique was developed during the 50s by Marvin Lee Minsky and then applied to biological samples during the 70s (62). Different from widefield microscopy, confocal microscopy uses a point scanning illumination pattern. The out-of-focus fluorescence is efficiently removed by a pinhole placed in the image plane of the microscope, **Figure 3.2** (**b**). Such a spatial filter enables a good optical sectioning of the sample (63) that allows performing z-stacks of samples to generate 3D images. In **Figure 3.1**, we report a 3D image of a HEK cell expressing EGFP-Δ50 lamin-A, codifying for Progeria.

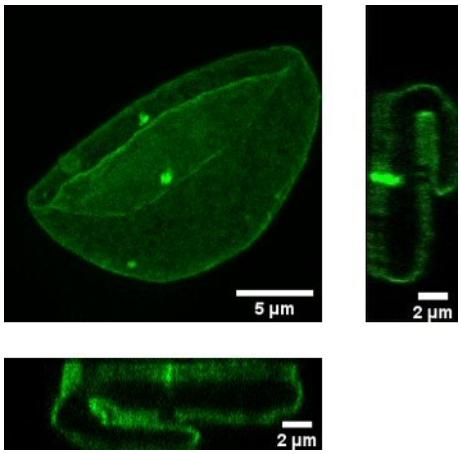

Figure 3.1. z-stack of HEK cell expressing EGFP-Δ50 lamin-A. On the sides, we report lateral views. It is easy to visualize the 3D structure of the cell and the invaginations due to the disease. Images are acquired using a confocal microscope (LEICA SP5) and edited through Fiji imaging processing package (38).

Since only one point at a time is illuminated, it is necessary to perform a raster scanning to obtain a whole image of the sample, thus strongly increasing the image acquisition time compared to a widefield microscope. Nowadays, scanning is performed by using one or more galvanometric mirrors or other approaches with low latency (**paragraph 8.1.1**). After the pinhole, a sensitive detector, usually a photomultiplier tube (PMT) or an avalanche photodiode, detects the light intensity, transforming the light signal into an electrical one.

Since the pinhole selects the fluorescence at the focal plane, the image's optical resolution (the capability of distinguishing two objects) is enhanced compared to widefield microscopes. However, signal intensity is less at a given position in the sample for the same reason. Long exposures time or high light intensity may often be required to improve the signal-to-noise ratio (SNR). A confocal implementation that reduces these limits is referred to as Spinning Disk. It uses a series of moving pinholes on a disc to scan light spots. The parallel scanning of the pinholes across an area, each of their hooves over a specific portion for a longer time, then reduces the excitation energy needed to illuminate a sample compared to the simple confocal microscope. Decreased excitation

energy reduces phototoxicity and photobleaching onto a sample, making a confocal/spinning disk microscope the preferred system for imaging live cells or organisms. It is important to point out that decreasing phototoxicity nowadays is one of the main challenges in microscopy since damages to cellular macromolecules upon light illumination can impair sample physiology and even lead to sample death. Another important advantage of confocal microscopy and fluorescence microscopy, in general, is that the fluorescence phenomenon accesses many spatial and functional information obtained through specific absorption, emission, lifetimes, photodecay, diffusion and other contrast mechanisms.

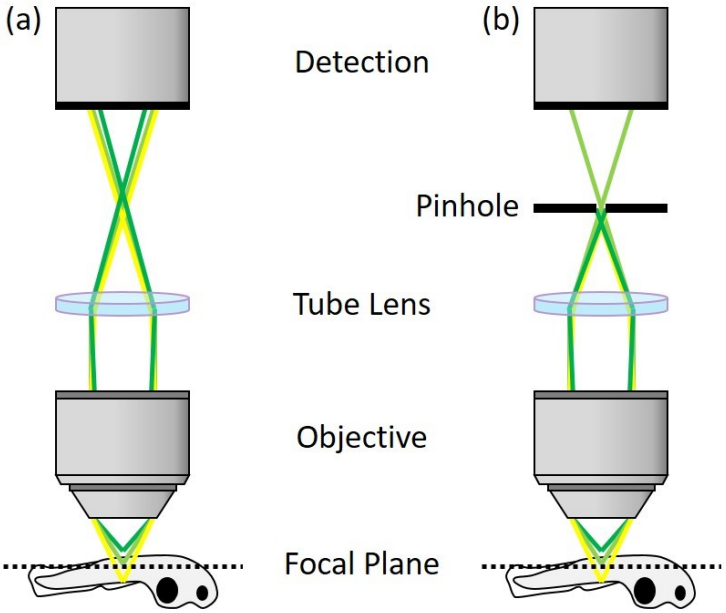

Figure 3.2. Schematic representation of a widefield (**a**) and a confocal (**b**) microscope. In confocal detection, the pinhole cuts off the contribution of the out-of-focus planes. The light-green ray is the on-focus fluorescence.

3.2 Principles of Light-Sheet Microscopy

However, confocal microscopy presents several drawbacks; one of the main is the poor intrinsic capability of studying thick samples and the poor acquisition speed. A new microscopy technique was developed to overcome these limits based on the decoupling of excitation and emission. This technique was firstly described in 1994 as Light-Sheet Fluorescence Microscopy (LSFM) by Francis Spelman (64) and Ernst Stelzer (65) and then as Selective Plane Illumination Microscope (SPIM) in 2004 by Jan Huisken (66). The core of these techniques relies upon fluorescence acquisition orthogonal to excitation. In this way, fluorescence and excitation are decoupled, improving the contrast (comparable to confocal microscope) and optical sectioning, reducing the photodamage. We can state

that Light-Sheet microscopy combines the advantages of the optical sectioning of confocal microscope with the higher acquisition rate provided by widefield microscopy. In **Figure 3.3**, we can see the differences among widefield (**a**), confocal (**b**) and light-sheet (**c**) architectures.

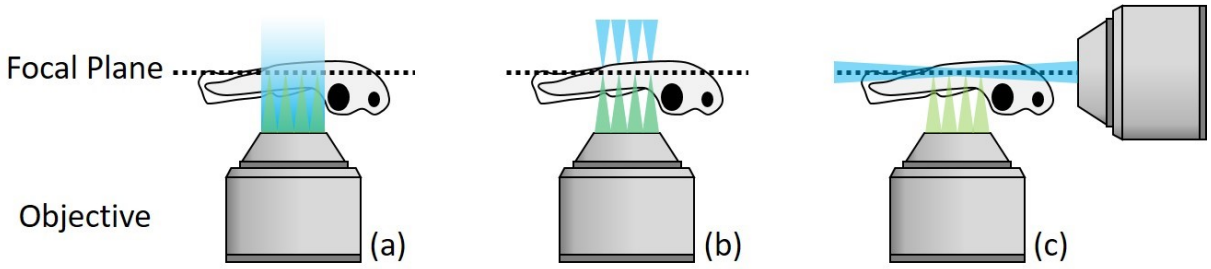

Figure 3.3. Schematic representation of the illumination modalities of widefield (**a**), confocal (**b**) and light-sheet (**c**) microscope. The excitation is cyan, and the fluorescence is green. In the light-sheet configuration, the excitation and the fluorescence are orthogonal. In cyan is reported the excitation, in green the fluorescence. The sample is simultaneously shined in widefield microscopy (**a**), and the fluorescence is acquired. In confocal microscopy (**b**), a focused laser is shined point by point in a scanning mode. In light-sheet microscopy, (**c**) illumination comes perpendicularly to the excitation, providing decoupling of the two.

To better understand the theory behind light-sheet microscopy, we should introduce the concept of beam waist (BW). BW represents the Gaussian beam's thickness at its focus, and it is a crucial parameter of LSFM: a thicker beam waist leads to worse sectioning but a larger field of view (**Figure 3.4**). The beam waist depends on the numerical aperture of the lens used.

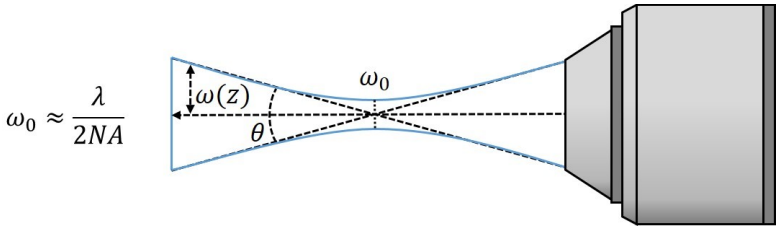

Figure 3.4. Schematic representation of the main parameters of a Gaussian beam: ω_0 is the beam waist, and ϑ is the divergence angle.

There are two approaches for the generation of the light sheet.

1. Cylindrical lens approach. This lens focuses the light onto a line instead of a point. It is the simplest and cheapest approach, but the cylindrical lens may introduce optical aberrations. It is worth noting that cylindrical lenses do not guarantee thin sheets of lights (beam waist) because of their numerical aperture.

2. Scanning approach. In this case, a single beam is scanned along the axis with a speed higher than the camera frame rate. The scanning systems generally are based on galvanometric mirrors or acousto-optic devices (67). The scanning system may also be used for scanning the light sheet along the optical axis of the detection objective, generating a three-dimensional (3D) illumination pattern.

SPIM provides a higher Field-of-View (FoV) for its intrinsic characteristics compared to other microscopy approaches. Combining this evidence with the high optical sectioning provided by the technique, we use light-sheet microscopy for 3D studies of thick samples. The general approach includes the motion, by a motorized stage, of the sample through the light sheet. We will comment in **Chapter 8** on another possibility of performing a 3D stack in LSFM.

3.2.1 Light-parallelization for SNR enhancement

Light-Sheet is the election tool for the volumetric image of large samples for both FoV and resolution. Nowadays, one of the main goals of optical microscopy is retrieving quantitative and volumetric information while minimizing sample photodamage. The photosensitivity of the sample forces to work with low exposition time and low laser power leading to images with poor SNR. In a standard LSFM, the easiest way to retrieve the lost signal would be to increase the excitation peak intensity, but the higher the illumination intensity, the greater the risk of inducing photodamage. Even with the photo-resistant sample, fluorescence is a saturable process, and at high laser powers, it results in no gain limiting the advantages of increasing laser power. To prevent phototoxicity and accumulate photons, a good solution would be to increase the exposure time or average multiple images. However, this strategy requires a longer acquisition time: it exists a trade-off between the acquisition speed and the SNR of the images. Parallelization of the illumination/acquisition represents an essential tool for enhancing SNR preventing damage to the sample. In **Chapter 8**, we report a practical application of this latter approach. Let us assume a general measurement f_i (n points p_j). In this paragraph, we will describe the process of light parallelization, pointing out its advantages in terms of SNR enhancement and background suppression. To better understand these latter processes, we need to define the matrix equation for a set of measurements and the noise types that can affect data. More details about the information contained in this paragraph can be found in the supplementary information of reference (67). We encode the sequence of measured points through the weights $\omega_{ij} \in \{0,1\}$, writing the following equation:

$$f_i = \sum_{j=1}^{n} \omega_{ij} p_j$$

Equation 3.1

Defining a $n\ x\ n$ square matrix W, whose entries are the weights, we can write the array of encoded measurements in matrix form:

$$\boldsymbol{f} = W\boldsymbol{p}$$

Equation 3.2

By inverting the matrix, we retrieve the individual points:

$$\boldsymbol{p} = W^{-1}\boldsymbol{f}$$

Equation 3.3

At this point, we must consider the presence of noise in our measurements. Here we will describe three types of noise: random noise, photon noise and background noise.

Random noise. We will assume this noise is independent of the signal:

$$\boldsymbol{f} = W\boldsymbol{p} + \boldsymbol{e}$$

Equation 3.4

With the following properties:

- The expected value of the noise is zero: $E[e_i] = 0$
- The noise is uncorrelated and has variance σ^2: $E[e_i e_j] = \sigma^2 \delta_{ij}$

We consider now the reconstruction, done with the inverse matrix $M = W^{-1}$ that leads to:

$$\widehat{\boldsymbol{p}} = M\boldsymbol{f} = \boldsymbol{p} + M\boldsymbol{e}$$

Equation 3.5

The mean square error (the variance of $\widehat{\boldsymbol{p}}$) in the presence of random noise ($M\boldsymbol{e}$) is given by:

$$\epsilon_i = \sigma^2 \sum_{j=1}^{n} m_{ij}^2$$

Equation 3.6

Photon noise. Considering a set of measurements not correlated, they will follow the Poisson distribution. In this case, we can write the mean square error as:

$$\epsilon_i = \nu\rho^2 \sum_{j=1}^{n} m_{ij}^2$$

Equation 3.7

Where we defined $\nu = \sum_{k=1}^{n} \omega_{ij}^2$ namely, the number of entries in the i_{th} column of W whose value equals one. We can finally write the mean square error in the presence of both random and photon noise:

$$\epsilon_i = (\sigma^2 + \nu\rho^2) \sum_{j=1}^{n} m_{ij}^2$$

Equation 3.8

Background. We must comment now on the possible presence of a uniform background for which $\beta_i = \beta_j = \beta \ \forall i, j$. We also assume the background independent of the signal, and we write:

$$\boldsymbol{f} = W\boldsymbol{p} + \boldsymbol{\beta}$$

Equation 3.9

The resulting background after the decoding with the inverse matrix $M = W^{-1}$ is now:

$$\boldsymbol{\beta}' = M\boldsymbol{\beta}$$

Equation 3.10

Where $\beta_i = \sum_{j=1}^{n} m_{ij}\beta_j = \beta \sum_{j=1}^{n} m_{ij}$. On the other hand, if the signal-dependent background is present, we have $\boldsymbol{f} = W(\boldsymbol{p} + \boldsymbol{\gamma})$. Even if its expected value is unaltered after decoding, the background contributes to degrading the SNR, being a source of photonic noise. The shape of the encoding matrix will play a crucial role in improving SNR. Interestingly, the parallelization approach, also called multiplexing, is borrowed from spectroscopy (68).

As we saw, parallelization enables decoding n planes P_j from n frames F_j, whose noise content is now $W^{-1}\boldsymbol{e}$ instead of $\boldsymbol{e}$**.** Such a noise reduction is an intrinsic feature of parallelized acquisition, known as Fellgett's advantage: the signal-independent noise of the measurement is shared among the illuminated planes. Roughly we can say that the larger the number of simultaneously acquired planes (and then frames), the lesser the noise per plane. This assumption is not completely true since the decoding step needed

to retrieve information from each plane can introduce some noise to the images. The choice of W (now referred to as S, encoding matrix) is crucial in determining the SNR of the decoded images since the amount of added noise depends on the encoding matrix. To illustrate this effect, we used three different illumination patterns, each one represented by a unique matrix:

1- S*equential scan.* This pattern corresponds to the traditional implementation of SPIM, where a single light sheet illuminates a single plane, and we perform z-scanning, moving illumination to a different axial position at each frame. Consequently, the encoding matrix, the identity I ($S^{-1} = I = S$), leaves the noise content unchanged. This non-parallelized acquisition scheme is used as a benchmark for the following ones.

2- *Black Light Sheet scan.* This pattern is based on $n-1$ parallel and identical light sheets simultaneously illuminating a volume divided into n sections: all planes within a volume are illuminated except for one. The axial position of the dark plane changes after each frame. As an effect, the dark plane scans over the sample. The corresponding matrix S contains zeros on the main diagonal and ones everywhere else. We expect the following gain in SNR for an image in the z-stack is:

$$\frac{\mathrm{SNR_n}}{\mathrm{SNR_0}} = \sqrt{\frac{1+\chi^2}{1+(n-1)\chi^2}}\frac{(n-1)}{\sqrt{(n^2-3n+3)}}$$

Equation 3.11

Where χ is the ratio of the standard deviation of the photon noise to the standard deviation of the camera noise (69), and SNR_0 is the SNR of the image acquired using a sequential scheme with the same exposure time and energy per light-sheet. The parameter χ depends on several variables, such as detector type, the brightness of the sample, and exposure time and is fixed for experimental setup and conditions. In fast imaging experiments, the exposure time is expected to be low, resulting in a small number of collected photons and, correspondingly, a low value of χ.

3- *Hadamard scan*. A volume, divided into n planes, is simultaneously illuminated by $(n+1)/2$ identical light-sheets. At each frame, the axial position of the beams is changed accordingly to the rows of the Hadamard matrix S (70). In this case, we expect an SNR gain as:

$$\frac{SNR_n}{SNR_0} = \sqrt{\frac{1+\chi^2}{1+\frac{n+1}{2}\chi^2}}\frac{n+1}{2\sqrt{n}}$$

Equation 3.12

Which also depends on the parameter χ. Note that, different from Black Light Sheet matrices that can be defined for every natural number n, Hadamard matrices are defined only for $n = 2^k - 1$, with $k > 1$ and integer. For a better understanding of the Hadamard matrix, we refer to supplementary information of reference (67).

To investigate the effects of parallelization on image background, we should consider that noise and offset affect imaging through a camera. We define this latter as the signal-independent background. The parallelization also offers the advantage of suppressing background, increasing the contrast of the reconstructed images. In particular, the expected background reduction with the Black Light Sheet encoding is:

$$\frac{\beta_n}{\beta_0} = \frac{1}{n-1}$$

Equation 3.13

Where β_0 is the background of the image acquired using the sequential scan. For Hadamard encoding, we write such a reduction as:

$$\frac{\beta_n}{\beta_0} = \frac{2}{n+1}$$

Equation 3.14

From **Equation 3.13** and **Equation 3.14**, we find that both encoding methods enable reducing the background compared to the sequential scan. In addition, such a reduction increases with the number of illuminated planes. However, the Black Light Sheet encoding shows better performance in background suppression. Therefore, while the Hadamard scan provides the best SNR gain of the strategies analyzed, the Black Light Sheet can be preferable when a strong background is present. Note that it is always possible to determine the optimal encoding method for a given sample or application.

3.3 The Diffraction Limit

In **paragraph 1.1.1**, we mentioned that the phenomenon of Diffraction is the basis for image formation. The Diffraction acts as a source of light that propagates to the objective concurring for the image formation. The conjugation between image and specimen means that each point of the specimen has a corresponding one in the image. It is

essential to state that the image of a point source through an objective lens is no more a point. The constructive and disruptive interferences produce a characteristic diffraction pattern consisting of a central bright spot (Airy Disk) surrounded by concentric rings forming the Airy pattern (**Figure 3.5**, **a**). The central spot contains around 84% of the light (71). The Airy Disk dimension depends on the wavelength λ and the angular aperture of the objective (72).

$$r = 1.22\lambda\frac{f}{D}$$

Equation 3.15

D/f is the aperture angle, f is the focal length, and D is the lens diameter. In terms of the NA defined in the previous paragraph, we can rewrite the previous equation as follows:

$$r = 1.22\frac{\lambda}{2NA}$$

Equation 3.16

Given $NA = nsin\alpha$, n is the refractive index of the medium between the sample and the objective, and α is the half-angle of the cone of specimen light accepted by the objective. We notice that the disk dimension decreases with decreasing wavelength and increasing numerical aperture. The dimension remains finite, and we define microscopy as a diffraction-limited technique. Ernst Abbe, who published the landmark paper containing the definition of the fundamental resolution limit, firstly quantified the phenomenon. The resolution limit was described as the shortest distance d between two points that can still be distinguished with a microscope system, otherwise they result unresolved (**Figure 3.5**, **c**) (73).

$$d = \frac{\lambda}{2NA}$$

Equation 3.17

Experimentally, this means that for a Numerical Aperture equal to one, and the visible wavelengths in the range of 400-700 nm, the resolution limit is around 200 nm. The British scientist Lord Rayleigh later redefined Abbe's theory with the Rayleigh criterion for the resolution limit: two Airy patterns are distinguishable if the center of one Airy disk falls on the first minimum of the other Airy Disk (**Figure 3.5**, **b**). The new definition of resolution limit (74) is given by:

$$d = 0.61\frac{\lambda}{NA}$$

Equation 3.18

When we look at a point source in 3D, the Airy Disk elongates in the axial direction. This typical density distribution is called the point spread function (PSF). The image is the result of the real light source with the PSF of the microscope used. The axial resolution is even worse than the lateral one and is given by the **Equation 3.19**:

$$d = \frac{2\lambda n}{NA^2}$$

Equation 3.19

The application of a pinhole improves this limit by a factor $\sqrt{2}$ since the confocal aperture can be closed to eliminate higher orders of the diffraction pattern (62,71). Thus, constraining the axial PSF and improving the optical sectioning of the technique. We can consider confocal microscopy a super-resolution technique to its $\sqrt{2}$ the improvement brought to resolution.

$$d_{xy} = 0.4\frac{\lambda}{NA}$$

Equation 3.20

$$d_z = 1.4\frac{\lambda n}{NA}$$

Equation 3.21

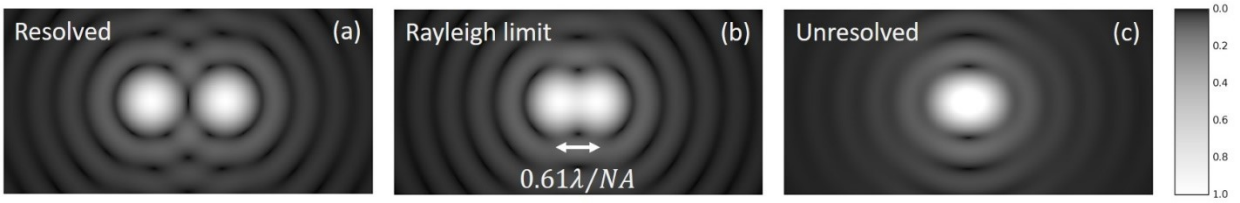

Figure 3.5. Airy diffraction patterns generated by light from two point sources passing through a circular aperture, such as the eye's pupil. We can resolve points far apart (**a**) or meeting the Rayleigh criterion (**b**) while points closer than the Rayleigh criterion (**c**) are unresolved. Image adapted from Wikipedia, Creative Commons BY-SA 4.0.

3.4 Super Resolution techniques

As we saw in the previous paragraph, the lateral resolution of usual microscopy techniques is constrained to around 200 nm in the visible range, limiting access at the nanoscale. In 2014 Eric Betzig, Wiliam E. Moerner and Stefan W. Hell won the Nobel Prize

in Chemistry for "the development of super-resolved fluorescence microscopy". The so-called nanoscopy consists of two main groups of super-resolution techniques:

- Deterministic super-resolution: based on **RE**versible **S**aturable **O**ptica**l** **F**luorescence **T**ransitions (RESOLFT). It is possible to prevent the emission of adjacent molecules by manipulating the fluorescing volume. The **ST**imulated **E**mission **D**epletion (STED), firstly developed by Stefan Hell, belongs to this group (75).
- Stochastic super-resolution: based on the complex temporal behavior of many fluorophores. In this group of techniques, the idea is to separate the light emission of two adjacent molecules temporally by the stochastic switching between a dark and a bright state.

The last group of super-resolution techniques includes a set of approaches that modestly increases resolution like the 4Pi microscope, the confocal itself and the **S**tructured **I**llumination **M**icroscopy (SIM). SIM is implemented on laser-based widefield microscopy, adding a movable diffraction grating into the excitation beam path (76). Zero-order or only first-order diffracted laser beams are let to pass through the objective interfering with each other at the focal plane of the objective and creating an illumination in stripes. This stripe pattern of light by its superimposition with the sample generates the so-called Moiré effect. Under homogeneous illumination, objects separated by a small distance, or in other words, being organized at high frequency, are not visible. Using structured illuminations overlaps the high-frequency organization of the sample with the high frequency of the illumination stripes creating an interference pattern of lower frequency, which is well collected by the objective. We will treat less the SIM in this work.

3.4.1 Deterministic super-resolution techniques

In these methods, super-resolution is achieved by the selective deactivation of fluorophores. As we saw in **paragraph 1.1.2**, fluorescence (spontaneous emission) occurs after the absorption of a photon, promoting an electron from the ground state to an excited one ($S_0 \rightarrow S_1$). The following relaxation from S_1 to S_0 can occur by the spontaneous emission, i.e., fluorescence. A second photon striking the fluorophore forces the excited electron to relax to the vibrational state corresponding to the energy gap that equals such photon energy. By selecting the photon energy in the red portion of the emission spectrum, the resulting stimulated emitted photon is red-shifted and easily decoupled from the fluorescence of interest. STED works by depleting the fluorescence in specific regions of the focus, e.g., a donut, leaving a central part of the spot to fluoresce. The donut-shaped depletion beam is achieved by altering the properties of the pupil plane of the objective (in **APPENDIX I**: Development and characterization of a phase-

plate, we report the process of fabrication and characterization of a phase plate used for STED/RESOLFT). An annular phase plate creates perfect null intensity at the focus. Another common implementation uses an optical vortex based on interference. We describe now the lateral by a modified Abbe's law:

$$d_{xy} = \frac{\lambda}{2nsin\alpha\sqrt{1 + \frac{I}{I_{sat}}}}$$

Equation 3.22

where n is the refractive index of the medium, I is the maximum STED intensity and I_{sat} is the saturation intensity defined as the power required to reduce the fluorescence intensity by half. The main drawback of STED is the need to use a high-intensity depletion laser, which may lead to photodamage and photobleaching. Another drawback of STED is that there will always be some fluorophores in the depletion area that are not being depleted by the STED depletion laser, resulting in fluorescence emission. Compared to the case of a perfectly depleted fluorophore, this leads to a lower obtainable resolution. Even if STED does not fully deplete the excited states of the fluorophores, it still affects their lifetimes. We obtain a higher resolution by filtering the photons by their arrival time. We term this approach Gated-STED (g-STED) since the filtering based on arrival time is called "gating". We can also use gating as a tunable parameter to reduce STED depletion power, thus avoiding photodamages and preserving the lateral resolution. G-STED allows higher super-resolution than STED without gating, but the reduced number of collected photons also reduces the SNR. A process of deconvolution is strongly recommended while working with STED images. Until now, we referred to STED as working with continuous-wave laser sources (CW), but STED can be implemented either with pulsed lasers systems or with CW laser sources (77). The use of pulsed lasers comes from the evidence that CW-STED requires higher average power than pulsed STED to achieve an optimal depletion. The STED pulse must arrive directly after the excitation pulse to achieve an efficient depletion; the excited level is no longer pumped. Another characteristic to consider is the pulse width or pulse duration. It is advantageous that the laser pulse width is significantly shorter than fluorescence lifetime (≈ 2 ns) and longer than vibrational lifetimes (≈1-5 ps) to avoid absorption back by the same pulse. Therefore, pulses in the 100 ps range are typically used. The pulse's duration also affects the resolution of STED, which mathematical derivation is presented by Moffitt *et al.* in reference (78). We can consider RESOLFT as a generalization of the STED concept. RESOLFT operates with molecules exhibiting at least two different optical states (photoactivable, photochromic), of which one (A) is bright and generates fluorescence, and the other (B) is dark, giving no signal. The transition between the two states is induced by light. In this case, the function of the

donut beam is deactivating the peripheral zone of the excitation by turning off the emitting molecules while the center remains bright. The inverse transition can be either spontaneous or stimulated. In addition, in this case, the new formula for the resolution is again the one in **Equation 3.22**. The architecture of Deterministic super-resolution techniques mainly based on scanning microscopes strongly constrains the acquisition time and the capability of performing live-cell imaging. Stefan Hell *et al.* presented a parallelized widefield arrangement exploiting the principle of RESOLFT (79). An intensity distribution of the switch-off light featuring zero intensity lines further apart from the conventional Abbe resolution limit is used to achieve parallelization. In this way, authors restrict rsFPs emission to lines of sub-diffraction size. The illumination pattern is then scanned over the sample. Compared to other methods, including applying the zeros of structured illumination (72,80), widefield RESOLFT microscopy avoids mathematical steps that are prone to noise issues. As we mentioned in **APPENDIX I**: Development and characterization of a phase-plate, our capability to develop linear phase plates suggests the fruitful application of RESOLFT to SPIM. In reference (81), the authors suggest the application of a half-moon phase plate combined with a photoconversion laser to a SPIM, reducing the light sheet's thickness and improving the axial resolution (originally constrained by diffraction limit) and, thus, optical section. This approach represents another way, slightly different from those previously presented, to bring RESOLFT (or STED) to a widefield configuration.

3.4.2 Stochastic super-resolution techniques

In this group of techniques, the temporal separation of adjacent emissions is the core. The optical architecture of the setup is often based on a widefield system. The most general definition can be called **S**ingle **M**olecule **L**ocalization **M**ethods (SMLM) (82). The signals of different fluorophores must be acquired sequentially rather than simultaneously by controlling their optical properties (83) to obtain super-resolution imaging. In this approach, single photoactivable or photochromic molecules are randomly activated in the sample (**Figure 3.6**). If only a *few* emitters are activated (with a controlled laser pulse) in a field of view of a few tens of microns, and the background is composed of molecules in the off state, then the switching statistic guarantees that the distance between on-molecules is major than the diffraction limit. Therefore, it is certain that the emitters are single molecules, and their position may be determined whit a nanometric precision. Turning off emitters and turning on new ones repeatedly allows for obtaining a high-resolution image after many cycles (generally thousands). The critical property of the fluorophore is its photoactivation for at least one cycle (84). Differences in technical details lead to different approaches. If we use genetically encoded exogenous probes fused to the interest target, we talk about **P**hoto**A**ctivated **P**hotolocalization **M**icroscopy

(PALM). If we stain endogenous molecules in the sample with antibodies labeled with organic fluorophores, we talk about **ST**ochastic **O**ptical **R**econstruction Microscopy (STORM)(85). In general, we describe the localization precision of the fluorophore may as follows (86):

$$\sigma = \sqrt{\left(\frac{s_i^2 + {a^2}/{12}}{N}\right)\left(\frac{16}{9} + \frac{8\pi s_i^2 b^2}{a^2 N^2}\right)}$$

Equation 3.23

Where N is the number of collected photons, a is the pixel size of the imaging detector, b^2 is the background signal in average, and s_i is the standard deviation of the PSF.

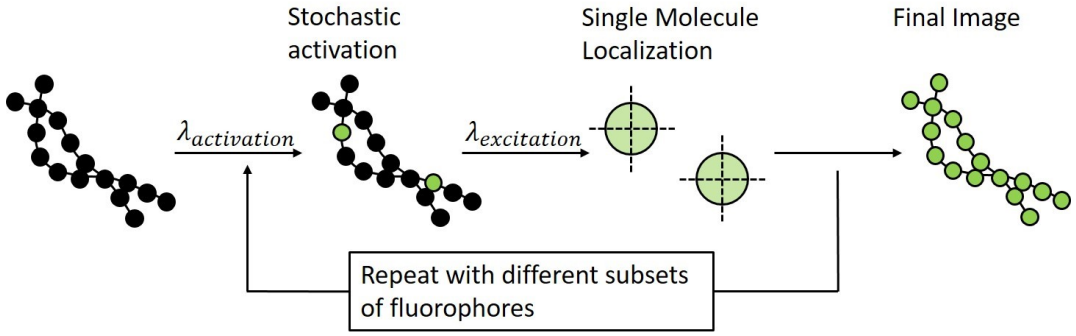

Figure 3.6. General representation of Single-Molecule Localization Methods. The final image is a density map reporting the positions of all the fluorophores acquired during the cycles.

The widefield architecture of SMLM suggests its fruitful combination with SPIM. In 2013 Francesca Cella *et al*. in reference (87), proposed coupling two-photon excitation to Individual Molecule Localization Single Plane Illumination Microscope (IML-SPIM). This approach combines the advantages of optical sectioning of SPIM, the resolution enhancement of SMLM and spatial confinement of 2PA. The improved signal-to-noise ratio of selective plane illumination allows nanometric localization of single molecules in thick scattering specimens without activating or exciting molecules outside the focal plane. The authors report then a 3D super-resolution imaging of a cellular spheroid.

4 Photoacoustic Microscopy

The first idea of using soundwaves to investigate biological systems comes from Stanford University around the 1970s by Ross Lemons and Calvin Quate (88). The strong belief that the visualization of the acoustic properties of the sample may reveal unobserved features of optically transparent samples moved them to investigate this approach. While in optical microscopy, variations of the dielectric properties determine the scattering, in acoustic microscopy, the material's elastic properties determine the scattering. Lemons and Quate developed a Scanning Acoustic Microscope (SAM) where a piezoelectric was the source of ultrasounds, and another piezoelectric was the receiver in the transmitted position (**Figure 4.1**, **a**) or where a piezoelectric acts both as receiver and emitter (**Figure 4.1**, **b**). The sample was placed in a water-filled chamber and moved by an XY-translational stage.

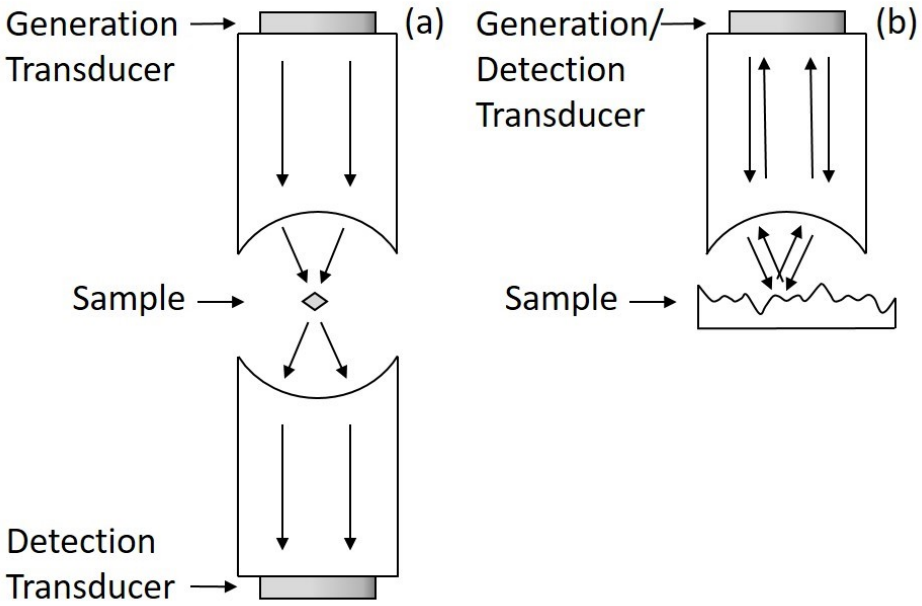

Figure 4.1. Schematic representation of Scanning Acoustic Microscope (SAM) in transmission (**a**) and reflection (**b**) mode. Image adapted from reference (88).

Another advantage of using acoustic waves is the less scattering of acoustic waves than light waves (89). As we mentioned in **paragraph 1.1.1**, the wavelength increase may reduce the scattering. Generally, we can say that techniques implementing acoustic detection may be used to study thick biological samples offering better penetration depth compared to light-based microscopy approaches. Many pioneering studies around the 1980s demonstrated that fast enthalpy and volume changes associated with the absorption of light by chromophores generate acoustic waves detected by microphones (90–92). The photoacoustic (PA) wave generated by applying a pulsed laser or a

modulated laser to an absorbing medium is the basis of an imaging technique that was termed Photoacoustic Microscopy (PAM).

4.1 Principles of Photoacoustic Microscopy

Despite the initial diffidence for the potential uses of PA techniques, in the last 40 years, the number of methods using photothermal effects (including PA) strongly increased, covering a wide field of applications from environmental sciences to material and biological sciences. The generation of PA waves is achieved through either a pulsed laser or a modulated laser source, which differences will be discussed later. The amplitude and phase of PA waves depend on the light source properties and the excited systems' optical, thermal, and mechanical properties. In general, the local rise in pressure p_0 is defined as follows:

$$p_0 = \Gamma \eta_{th} \mu_a F$$

Equation 4.1

Where η_{th} is the percentage of light converted to heat, F is the fluence of the illumination source, and Γ is the Gruensein parameter defined as $\Gamma = \beta / k_B \rho C_P = \beta v_S^2 / C_P$ (93). In this equation, β is the expansion coefficient, k_B is the Boltzmann constant, ρ is the density, C_P is the specific heat at constant pressure and v_s is the speed of sound. μ_a then is the absorption coefficient. After the initial pressure rise, the pressure wave diffuses inside the sample at the sound speed in the medium.

The flexibility and suitability for thick samples studies allow the application of this detection in Photoacoustic Tomography (PAT) approaches (97) that are devoted to performing 3D imaging onto thick biological systems. Nowadays, photoacoustic techniques are some of the fastest-growing methodologies in biomedical imaging (94–96) for their combination of optical excitation and acoustic detection, leading to two main features: First, PAM provides high-contrast spectral properties of tissues by investigating the optical absorption of the system (95). Second, detecting acoustic waves provides a relatively large penetration depth for the lower attenuation of sound waves (97). Based on the optical configuration, we can distinguish three main groups of applications of PA: photoacoustic computed tomography (PACT), optical-resolved photoacoustic microscopy (OR-PAM) and acoustic-resolved photoacoustic microscopy (AR-PAM), including the hybrid approach Ultra High-Frequency Photoacoustic Microscopy (UHF-PAM). In the next chapter, we will comment on the properties and configuration of OR-PAM, AR-PAM and UHF-PAM techniques.

4.2 Resolution of Photoacoustic Microscopy

As we mentioned in the previous paragraph, there are many possible implementations of photoacoustic microscopy according to what drives the lateral resolution. Like optical microscopy, acoustic and photoacoustic microscopy has in resolution penetration depth and contrasts their main characterizing parameter (98). This paragraph will comment on the main properties of selected photoacoustic microscopy approaches.

4.2.1 Optical Resolved Photoacoustic Microscopy (OR-PAM)

In OR-PAM, a diffraction-limited light spot is focused on the sample, and an ultrasound transducer acquires the emitted soundwave. Since the optical focal spot is much time smaller than the acoustic one, the optical properties of the system drive the lateral resolution (99). Therefore, the lateral resolution of OR-PAM is given by the size of the light spot, according to Abbe's Law:

$$R_{L,OR} = 0.51 \frac{\lambda_O}{NA_O}$$

Equation 4.2

Where λ_0 is the optical wavelength, NA_O Is the numerical aperture of the objective, and 0.51 is the full width at half maximum (FWHM) of the optical focal spot. For the axial resolution, we base on the assumption that the PA response to a point target follows a Gaussian frequency profile, and we write the following **Equation 4.3**:

$$R_{A,OR} = 0.88 \frac{v_A}{\Delta f_A}$$

Equation 4.3

Where $v_A$is the speed of sound of the medium and Δf_A is the PA signal bandwidth that is approximated as the transducer bandwidth. This last assumption is based on the fact that the PA bandwidth is much wider than the transducer detection bandwidth. We can comment that, since higher frequency components of PA signal are attenuated faster than lower ones, we can have degradation in axial resolution while investigating thicker samples. For its properties, OR-PAM is well suitable for single-cell imaging while having advantages in terms of resolution of light and its low penetration in tissues.

4.2.2 Acoustic Resolved Photoacoustic Microscopy (AR-PAM)

In AR-PAM, the sample is shined with an unfocused light source (That may also be the scattering of a diffraction-limited beam inside the sample), and a focused ultrasound transducer (100) harvests the acoustic emission. Here the lateral resolution is given by

the acoustic properties of the transducer. We can generally describe the resolution of a microscope as linked to its working frequency and numerical aperture (98) as follows:

$$R = \frac{\lambda}{2NA}$$

Equation 4.4

For an acoustic wave, we can write the relation $\lambda \times f = v_A$ that links the wavelength of the acoustic wave with the frequency and the speed of sound in the medium. We can rewrite **Equation 4.4** as follows:

$$R = \frac{v_A}{2f_A NA}$$

Equation 4.5

Considering the FWHM of the acoustic focal spot in acoustic amplitude (99), we obtain the final relation (**Equation 4.6**):

$$R_{L,AR} = 0.71\frac{v_A}{f_A NA_A}$$

Equation 4.6

Where NA is the numerical aperture of the ultrasonic transducer, as OR-PAM, the axial resolution in AR-PAM is defined as follows:

$$R_{A,AR} = 0.88\frac{v_A}{\Delta f_A}$$

Equation 4.7

AR-PAM is suitable for thick tissues studies where the focused optical beams scatter and become diffuse (99).

4.2.2.1 Ultra-High Frequency Photoacoustic Microscopy (UHF-PAM)

Here we present a hybrid approach in photoacoustic. Since both lateral and axial resolution of AR-PAM depends on the acoustic frequency, increasing that parameter may improve image quality. While working with a frequency over 1000MHz, we can reach a lateral resolution comparable to an optical microscope. However, the higher is the sound frequency, the higher is the attenuation by the medium, limiting this technique to the study of thin cell layers.

4.2.3 Super Resolution in Photoacoustic Microscopy

Many approaches to overcome the diffraction limit exist in PAM, like happening in fluorescence microscopy. Since the higher resolution of PAM is OR-PAM, super-resolution

techniques break the diffraction limit by using nonlinear techniques such as saturations, switchable quenching, or multiphoton absorption on the illumination part of the process. This paragraph will present the state-of-art of Super-Resolution PAM, excluding approaches based on photochromic probes that will be further commented on in **paragraph 4.4.3.1**.

4.2.3.1 Nonlinear Photoacoustic Methods

The principle demonstrated by Danielli *et al*. (101) is based on the nonlinear dependence of PA waves from the excitation at higher energy levels. In PAM image generation, the peak intensity per pixel of PA waves is collected and assumed proportional to the excitation beam. While working at higher excitation power, this assumption is no longer valid, and mechanisms such as nonlinearity, optical saturation or multiphoton absorption occur. The first source of nonlinear PA is based on nonlinear thermal expansion. By considering the second-order term of the expansion coefficient, write as follows:

$$\beta(T) \approx \beta_1 + \beta_2 T$$

Equation 4.8

The laser induces pressure in the acoustic excitation voxel described by the **Equation 4.9** from reference (102):

$$p(r - r_0, z - z_0) = \frac{1}{k}\{\beta_1 T(r - r_0, z - z_0) + \frac{1}{2}\beta_2 [T(r - r_0, z - z_0)]^2\}$$

Equation 4.9

While the second nonlinear effect is due to the optical saturation related to single-photon absorption, under specific conditions, the initial pressure in the voxel may be written as a polynomial expansion:

$$p_0(r_0, z_0, E_p) = \sum_{n=1}^{\infty} c_n(r_0, z_0)(E_p)^n$$

Equation 4.10

Here E_p Is the energy per pulse. The main point of this approach is that a train of increasing energy pulses pumps the sample, saturating all the electrons. In this saturated state, the additional energy is depleted through different pathways, such as non-linearities. From these pressure waves, images corresponding to the absorption of different molecules can be reconstructed. These techniques allow the resolution to boost up to 88 nm. However, these approaches are limited to subsurface and have a poor temporal resolution due to the scanning system. Localization methods have been applied

to accomplish super-resolution imaging in PAI, ultrasound imaging, and fluorescence microscopy. The general principle of the localization imaging method is to superimpose the local maxima positions of all localized sources in the sequence of images (103). The authors demonstrate improvements from 7.5 µm to 0.4–0.7 µm in the lateral resolution and from 33 µm to 2.5 µm in the axial resolution in vitro. Furthermore, the unresolved microvessels in the conventional OR-PAM images are visualized in the localization PAM images. This approach may also work with ultrasound arrays (104).

4.2.3.2 Two-Photon Photoacoustic Mechanism

Non-radiative two-photon absorption (2PA) improves axial resolution, allowing high 3D resolution. Conventional PAM requires spatial filtering to achieve high axial resolution, while in Two-Photon Photoacoustic Microscopy (2P-PAM), only the area within the focal spot generates nonlinear photoacoustic signals. Due to easier one-photon absorption, a prominent 1PA signal will be competitive with the 2PA signal (**Figure 4.2**, **a-b**). The 2PA signal is extracted using a lock-in detection system (105): the input laser is amplitude modulated, and the two-photon PA is extracted by locking at the modulation frequency or one of its harmonics. This approach will be explained in detail in **Chapter 7**. In the paper by Lee et al., the authors achieve (106) a later and an axial resolution of 0.51 µm and 2.41 µm, while 1PA has a lateral resolution of 0.71 µm. The system shows an improvement of factor 1.4 in lateral resolution.

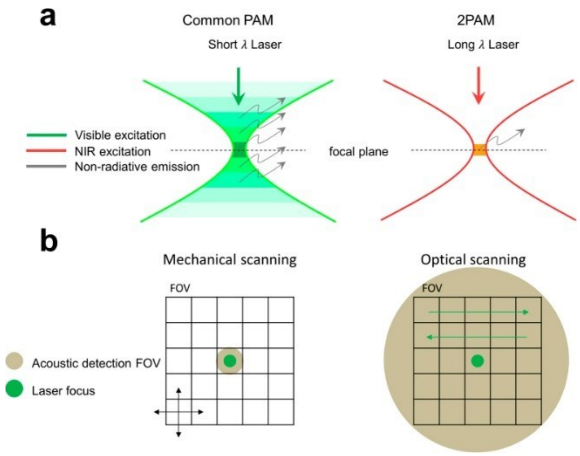

Figure 4.2. Comparisons between 1P-PAM and 2P-PAM. (**a**) Temporal or spatial filtering is necessary to eliminate the induced background and acquire the axial resolution in common PAM based on the visible laser excitation process. However, in 2P-PAM, with NIR excitation, only photons within the focal spot generate nonlinear photoacoustic signals providing intrinsic optical confinement, determining the 3D spatial resolution. (**b**) While only mechanical scanning is applicable in current common PAM due to the small acoustic detection filed-of-view (FOV), 2P-PAM could be operated at low acoustic frequency creating a large acoustic detection FOV. Optical scanning is thus possible. Image from reference (106).

4.2.3.3 Structured Illumination Photoacoustic Microscopy (SI-PAM)

Another approach that we treat quickly exploits structured illumination to increase the resolution of PAM. Such a specific illumination pattern (called moiré interference pattern), generated by interference, provides an easier view (76). As we mentioned in **paragraph 3.4**, the capability of structured illumination of increasing resolution in optical microscopy relies on the information provided by the interaction of the three-dimensional modulated illumination patterns and high-frequency variation in sample fluorescence caused by small structures. These interactions generate a low-frequency Moiré pattern containing information on non-resolvable structures. Imaging the Moiré patterns at different positions and their subsequent processing allows the reconstruction of sub-diffraction information. In photoacoustic and implementation of structured illumination called **B**lind **S**tructured **I**llumination **P**hoto**A**coustic **M**icroscopy (BSIPAM) uses optical speckle patterns as structured illumination for enhancing the spatial resolution of PA imaging in scattering media, describing the measured PA signal as a function of the various speckle patterns and the absorber distribution (**Figure 4.5**, **a-c**). Through acquiring various images and deconvolution, it is possible to retrieve the original distribution of the sample with an improving factor of 2 (**Figure 4.3**, **d**) (107). Other approaches providing better improvement are reported in reference (108). Since SI-PAM works in AR-PAM mode, the achievable resolution is in tenths of microns (around 20 µm in the previous reference) but with a slightly improved penetration depth.

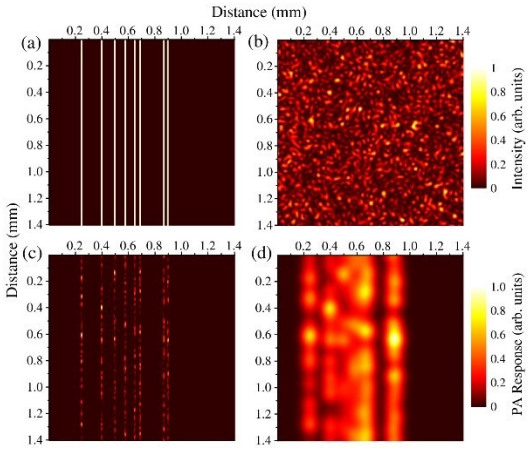

Figure 4.3. Simulated results by Murray *et al*. show (**a**) an absorbing system consisting of 10 µm wide lines separated by distances varying between 40 and 150 µm. (**b**) a speckle pattern with a speckle size of 25 µm. In (**c**), the product of the absorber distribution and speckle pattern giving the photoacoustic (PA) source distribution is reported. Finally, (**d**) shows the PA response found by convolving the PA source distribution with the transducer PSF (Gaussian with an FWHM of 100 µm). Image from reference (107).

4.3 Sensitivity of Photoacoustic Microscopy

Another important classification of PAM relies on optical sources. There are mainly two sources that may be used: pulsed laser sources or modulated continous-wave (CW) laser sources (109)

4.3.1 Signal Generation in photoacoustic microscopy

In this chapter, we consider the initial pressure rise in both pulsed and CW photoacoustic, starting from **Equation 4.1**. Assuming working with Gaussian pulses, we define the overall intensity as follows:

$$I_{pulsed}(t) = \frac{F}{\tau\sqrt{2\pi}} e^{-\frac{t^2}{2\tau^2}}$$

Equation 4.11

With a fluence F and an FWHM of the temporal pulse profile of $2\sqrt{2ln2}\tau$, where τ is the pulse width. The resultant PA pressure for a target point is proportional to the time derivative of the excitation pulse (3). The maximum PA pressure is:

$$p_{pulsed,max} \propto \frac{\Gamma\eta_{th}\mu_a F}{\tau^2}$$

Equation 4.12

For a modulate CW laser, the temporal profile of the intensity is the following:

$$I_{CW}(t) = I_0[1 + \sin(\omega_c t)]$$

Equation 4.13

Where ω_C is the modulation frequency and I_0 is the average laser intensity. Then the maximum PA pressure is defined as follows:

$$p_{CW,max} \propto \Gamma\eta_{th}\mu_a\omega_C I_0$$

Equation 4.14

Taking account of the **Equation 4.13** and **Equation 4.14**, we can compare both illumination approaches. CW sources, and their modulation and electronics, are generally cheaper than pulsed ones, while the higher operating frequency allows faster imaging (110). However, by comparing the two previous equations is easy to see that pulsed excitation provides better PA generation than CW (111). In addition, pulsed illumination provides axial resolution: the acoustic flight time that depends on laser pulse width, the tissue's acoustic attenuation, and the detection bandwidth provide information on the depth of the target absorber and the axial resolution. By contrast, CW excitation does not

provide similar information (112). The following paragraph will discuss the approaches that maximize PA signal generation.

4.3.2 Detection in Photoacoustic Microscopy

The core of any PAM system is the detection tool: an ultrasound transducer (UST). USTs are generally made of a piezoelectric material, capable of converting an electrical signal into mechanical motion and vice versa, making them suitable for generating and detecting soundwaves. Structurally, UST includes a disk of a piezoelectric material, which thickness determines the resonance frequency, and a damping material, absorbing the backward-traveling waves and damping the resonance of the disk. The damper enables the transducer to produce waves short in time and wide in frequency bandwidth (**Figure 4.4**). The two most popular choices of material for the piezoelectric disk are the ceramic lead zirconate titanate (PZT) and the polymer polyvinylidene fluoride (PVDF)(113). UST may be unfocused (flat) or spherically/cylindrically focused. In **Figure 4.4** are reported the main properties of a spherically focused transducer that are useful to understand the **Equation 4.7** relative to lateral resolution in AR-PAM.

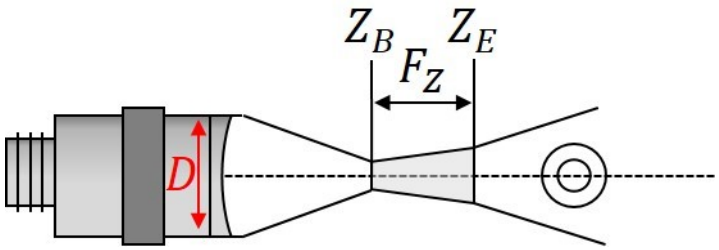

Figure 4.4. Main features of an ultrasound transducer. Z_B and Z_E are respectively the beginning and the end of the focal zone (FZ). D is the element diameter. The dashed line is maximum intensity line, and the circular crown is respectively the -6 dB and -12 dB beam diameter. The beam diameter (BD) at -6 dB at the focus is calculated through the equation $BD(-6dB) = 1.02Fc/fD$ for a focused transducer. For a flat transducer the equation is different: $BD(-6dB) = 0.2568DS_F$. BD =beam diameter, F =Focal Length, c =material spund velocity, D=element diameter and S_F=normalized focal length (=1 for flat transducers) defined as the ratio between the focal length and the near field (N). The focal zone is calculated as follows: $F_Z = NS_F{}^2[2/(1 + 0.5S_F)]$. F_Z is the focal zone, N is the near field (The far field is the area beyond N where the sound field pressure gradually drops to zero).

4.3.3 Noise in Photoacoustic Microscopy

It is important to comment on the sources of noise, which, as in all the other microscopy techniques, can limit the detection (110,114). The noise in PAM arises mainly from three sources: thermal, acoustic noise from the medium, thermal noise from the ultrasonic transducer and electronic noise from the amplifier. We describe noise in terms of power spectral density (PSD) that describes the distribution of noise power per bandwidth unit

as a frequency function (110). The medium generates a thermal, acoustic noise which PSD is:

$$N_a(f) = \eta_d(f) k_B T$$

Equation 4.15

Here η_d Represents the efficiency of the transducer at a frequency (f), defined as the fraction of acoustic power converted to electrical power. T is the absolute temperature of the medium and k_b Is the Boltzmann constant. The transducer itself generates a thermal noise due to the thermal agitation of charge carriers (also called Johnson-Nyquist noise). Considering a transducer with an internal resistance matched to a preamplifier with an internal resistance R. In this case, the PSD is given by (115):

$$N_d(f) = k_B T$$

Equation 4.16

As an electronic component, also the preamplifier introduces additional noise. Using a matched impedance, the preamplifier noise is well described through the noise factor F_n, representing the ratio between the thermal noise of the source resistor, at the input, and the output noise of the preamplifier. The PSD is given by:

$$N_{am}(f) = N_d(f)[F_n - 1]$$

Equation 4.17

Summing the three above components of the noise, we obtain the total noise power:

$$P_{noise} = \int_{\Delta f} df[\eta_d(f) + F_n] k_B T$$

Equation 4.18

Where Δf is the frequency bandwidth of the ultrasonic transducer.

4.3.4 Optimizing PA signal generation

There are many ways to optimize the PA SNR. Looking at the temperature dependence of noise, one might attempt to chill the medium, but, as we saw in **paragraph 1.3**, the PA signal has a stronger dependence on temperature through the linear reduction of the expansion coefficient. The chilling method is counter-effective. The signal-averaging may help but reduces the imaging speed. One key point is the reduction of the bandwidth of the transducer and associated electronics (114). For example, a narrowband ultrasound transducer with a CW excitation mode and a lock-in Detection can easily bring a 1000 reduction factor of the noise (110) amplitude. However, the SNR in pulsed excitation is

still better than the CW counterpart. In addition, a narrowband transducer strongly degrades axial resolution for the **Equation 4.7**.

4.4 Contrast in Photoacoustic Microscopy

Photoacoustic microscopy has its base in the medium's optical properties, so the contrast depends on the different optical properties of the target probe and the background. We can classify the contrast agents through their availability in the interest system between endogenous and exogenous.

4.4.1 Properties for contrast agents for photoacoustic microscopy

Probes for photoacoustic microscopy must have slightly different properties compared to the probes designed for fluorescence microscopy. Looking at the energy balance (3):

$$E_\lambda = \phi_f E_f + \sum Q_i + E_{stored}$$

Equation 4.19

Where E_λ is the total energy of the photon, ϕ_f is the quantum yield of fluorescence, Q_i the energy associated with each non-radiative step and E_{stored} The energy stored in photoproducts living much longer than the pressure-integration time of the experiment. The main properties that a good probe suitable for PAM should have a low (or none) fluorescence quantum yield and the absence of any photoproduct to minimize the competitiveness between these processes and the heat release. As shown in **Equation 4.1**, optical absorption is a crucial parameter for PA emission: good PA probes should have good optical absorption. We further divide the contrast agents between endogenous and exogenous, as we mentioned before.

4.4.2 Endogenous contrast agents

One of the primary advantages of PAM is the capability of imaging label-free specimens in a large spectral range (UV, visible, NIR). Some of the most common sources of contrast that absorb in the visible spectral range are hemoglobin in red blood cells (RBCs), cytochromes in mitochondria, and melanin in melanosomes. At the same time, we can investigate DNA and RNA in the UV spectral range and in the NIR, water and lipids. **Figure 4.5** shows some of the most common absorbers in living tissues. In reference (100), the authors demonstrate the bi-concave shape of RBCs using a diffraction-limited 532nm laser spot in an OR-PAM configuration with a resolution of 220 nm. The concentration and the localization of hemoglobin inside the RBC provide information on the health state of the cell itself. In reference (116), Tan *et al*. used PAM to image anemic RBC, finding out that a major concentration of hemoglobin at the cell's periphery is a symptom of this disease. The thickness of the central region of RBC is also symptomatic of anemia (117).

These measurements were performed using an OR-PAM configuration with a 532 nm laser and a 50MHz transducer, providing a lateral resolution of 1 µm. A multiphoton approach was proposed in reference (118) to increase optical depth. Using a pump laser and probe pulses makes it possible to create separate PA signals extracted by temporal frequency encoding. This method is called transient absorption ultrasound microscopy (TAUM). This technique needs a low-frequency ultrasound transducer with a lower lateral resolution than other approaches. It is important to notice that a label-free PA nanoscopy uses hemoglobin in RBC as described partially in **paragraph 4.2.3.1** and reference (101)

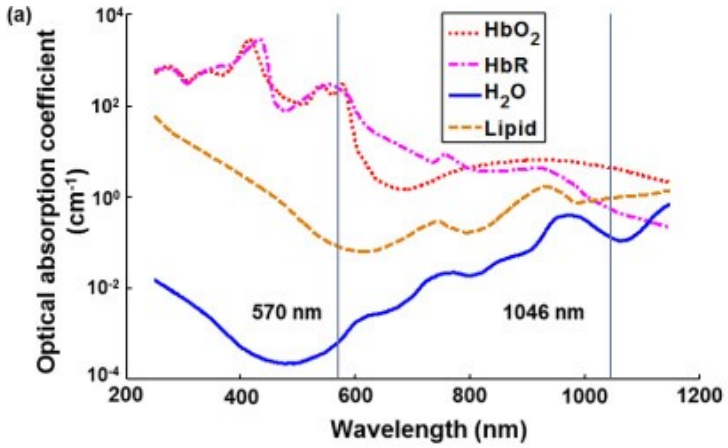

Figure 4.5. Representation of the absorption of many tissues' components depending on the wavelength. Water and lipids are suitable for NIR studies, while Hemoglobin and other co-factors are more useful in the Vis range. Image reproduced from reference (119)

Another important endogenous contrast agent is represented by the cytochromes, proteins facilitating the energy production in mitochondria (120). In reference to (121), the cytochromes were targeted with a 422 nm laser, and the signal was acquired with a 40MHz transducer. A good agreement was demonstrated between the photoacoustic image and the fluorescence one, obtained by using MitoTracker Green FM stain. Another important endogenous contrast agent is represented by the cytochromes, proteins facilitating the energy production in mitochondria (120). In reference (121), cytochromes were targeted with a 422 nm laser, and the signal was acquired with a 40MHz transducer. It was demonstrated a good agreement between the photoacoustic image and the fluorescence one, obtained by using MitoTracker Green FM stain (**Figure 4.6**, **a-d**).

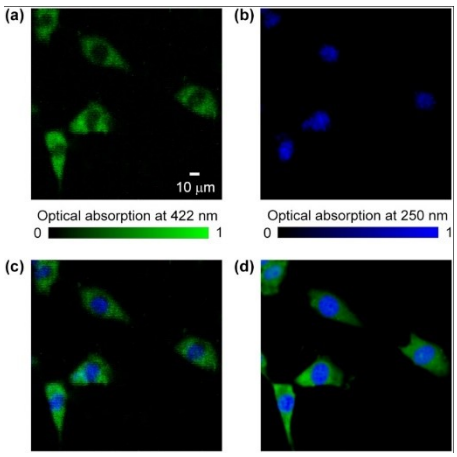

Figure 4.6. PAM and fluorescence microscopy of fibroblasts. (**a**) Label-free PAM image of fixed but unstained fibroblasts acquired at 422 nm wavelength. (**b**) Label-free PAM image acquired at 250 nm wavelength. (**c**) Dual-color superimposed image of (**a**) and (**b**). (**d**) Fluorescence microscopy image of the cells with mitochondria stained in green and nuclei stained in blue. Image reproduced from reference (121).

Melanin pigment is an important molecule present in the melanosome organelle within melanocytes. It could be imaged in PAM. Then a branch of PA working in the UV region is present, called UV-PAM. In this light region, the main absorbers are the nucleic acids DNA and RNA (122). Imaging these acids at 250nm seems to provide better contrast among other cell components. In reference (123), Yao *et al.* combined the UV absorption with a 422 nm excitation, providing a label-free PA providing information similar to histopathological ones. Recently, it has been demonstrated that the application of UV-PAM intraoperative histopathologic examination of the surgical specimen is crucial for tumor margin identification with a less complicated sample preparation than other methods (124).

4.4.3 Exogenous contrast agents

All the endogenous contrast agents strongly improve contrast and generate high SNR images due to their strong optical absorption but are limited to availability in different cell lines. Similarly, to optical microscopy, it is necessary to provide contrast agents from the outside. These exogenous contrast agents generally are calorimetric stains, fluorescent dyes, nanoparticles or fluorescent proteins (FPs) (125,126). If stains with different optical properties are selected, different lasers may be used to separate PA contributions. Histopathological Wright's stain was used in UHF-PAM by Strohm *et al.* in reference (127) to determine the different characteristics of neutrophils, lymphocytes and monocytes. The setup uses a 532/610 nm laser and a 1000MHz ultrasound transducer. In this work, we also demonstrated the feasibility of Hematoxylin & Heosin (H&E) stain in 2P-PAM. Using exogenous agents makes it possible to move to PAM the

toolbox of techniques developed for optical microscopy. FRET is one of the possibilities. Wang *et al.* in reference (128), demonstrated the application of FRET to a fluorescent donor (Rodhamine 6G) to a non-fluorescent acceptor (DOQCI). The system used a tunable laser, pumped by an Nd:YLF laser, with the excited PA and fluorescence signal acquired by a 50 MHz ultrasonic transducer and a photomultiplier tube module, respectively (129,130). The authors used this approach to quantify FRET efficiency through PA to a depth of around 1 mm. Another tool moved from optical microscopy is FPs (131); in reference to (132), authors use a FRET pair made of two genetically encoded probes miRFP670-iRFP720 in PAT, enabling dynamic functional imaging of active biological processes in deep tissues. By PA detection of the changes in the optical absorption of the miRFP670 FRET-donor, they monitored cell apoptosis in deep tissue at high spatiotemporal resolution using PAT; they detected apoptosis in single cells at a resolution of ≈3 µm in a mouse ear tumor and in deep brain tumors (>3 mm beneath the scalp) of living mice at a spatial resolution of ≈150 µm with a 20 Hz frame rate. It is important to focus on the role that FPs and their subclass of rsFPs may have in PAM.

4.4.3.1 Photochromic proteins in photoacoustic microscopy

In the last years, the possibility of improvements in lateral resolution in PAM suggested using rsFPs similarly to super-resolution fluorescence microscopy, terming the technology reversibly switchable photoacoustic microscopy (RS-PAM). Yao *et al.* (133) demonstrated a differential PA imaging of a bacterial phytochrome BphP1. The idea is that when stable BphP1 is on the *on*-state upon 780 nm irradiation pulse train, molecules are gradually converted to the *off*-state. As a result, the PA amplitude of the signal decreases proportionally to the local excitation intensity. Thus, the PA signal in the center decays faster than in the surroundings. A differential approach between two images will give a high contrast image of the cell with a sub-diffraction resolution. This means a smaller FWHM of the lateral PSF that is shown to be $(0.51/\sqrt{1+bm})\lambda/NA$ where m is the power dependence of the switching-off rate on the excitation intensity and m is the order of the polynomial fitting. RS-PAM achieves a $\sqrt{1+bm}$ improvement in resolution compared to conventional PAM. For the axial resolution, the improvement is the loss of dependence from the acoustic components, providing good optical sectioning to RS-PAM. The axial PSF is quantified as $1.8\sqrt{2^{1/(1+bm)}-1}(\lambda/NA^2)$. The authors estimated the lateral and axial resolution of around 141 nm and 400 nm, respectively (**Figure 4.7**, **a-c**).

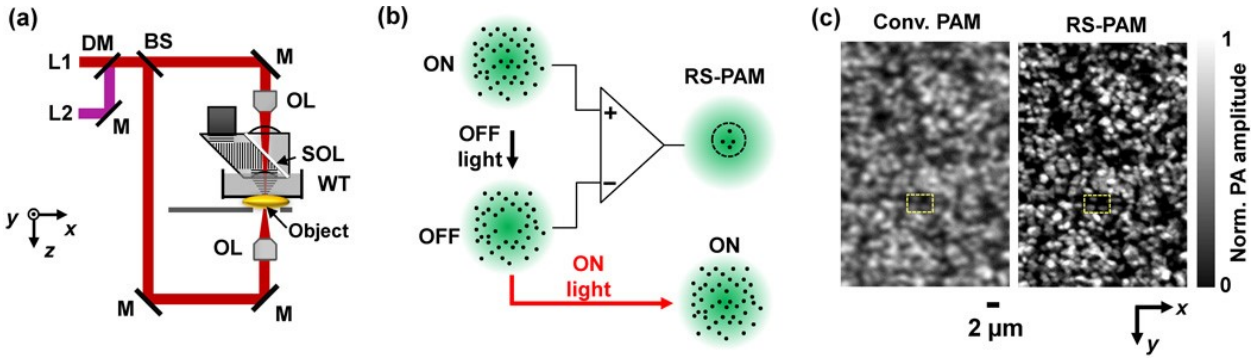

Figure 4.7. Sub-diffraction photoacoustic microscopy of reversibly switchable BphP1 (RS-PAM) shows an effective improvement in lateral resolution. (**a**) Schematic of the double-illumination photoacoustic microscopy system. BS, beam splitter; DM, dichroic mirror; L1–2, the laser beam 1 and 2; M, mirror; OL, optical lens; SOL, silicone oil layer; WT, water tank. Top objective NA: 0.1; Bottom objective NA: 1.4 with oil immersion. The transducer was a full-ring ultrasonic transducer array (Imasonic) with a 5 cm diameter, 5 MHz central frequency and 512 elements. (**b**) Principle of RS-PAM with sub-diffraction resolutions. Within the diffraction-limited excitation volume, some ON state BphP1 molecules (red dots) are switched to the OFF state, where the switching-off rate is proportional to the local excitation intensity. RS-PAM improves the spatial resolution in all dimensions by fitting the nonlinear signal decay dynamics. (**c**) Conventional PAM and RS-PAM images of BphP1-expressing bacteria are densely fixed on a cover glass, showing the superior lateral resolution of RS-PAM. Image adapted by permission from Springer Nature Customer Service Centre GmbH: Springer Nature, *Nat Methods* **13**, 67–73 by Junjie Yao *et al.* Copyright © (2016) (133).

In **Figure 4.8** (**a,b**), the image resolution improvement by exploiting photochromic proteins for background suppression is significant. The images were acquired monitoring a tumor expressing BphP1 through PACT.

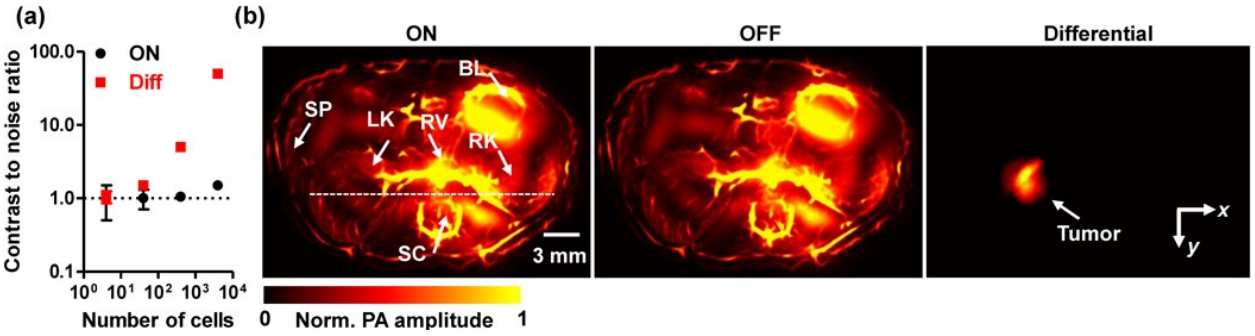

Figure 4.8. PA images of BphP1 expressing U87 cells and HbO2 in scattering media. The differential image effectively removes the background signal, increasing the contrast of the cell area (**a**) Whole-body PACT images of the liver region of a representative nude mouse repeatedly acquired for 30 days after the injection of BphP1-expressing U87 cells into the right liver lobe (n = 6). Differential signals (shown in color) are overlaid on top of the structural signals from the blood. The differential image effectively removes the background signal, increasing the contrast of the cell area (**b**) Increase in areas of the primary and secondary tumors—error bars standard errors of the results from 6 animals. Image adapted by permission

from Springer Nature Customer Service Centre GmbH: Springer Nature, *Nat Methods* **13**, 67–73 by Junjie Yao *et al*. Copyright © (2016) (133).

A huge work of characterization has been done by Paul Vetschera *et al.* in reference (42). Here the authors characterized many genetically encoded probes for fluorescence microscopy from an optical point of view. It is important to notice that FPs designed for fluorescence are not suitable for PAM for their high fluorescence quantum yield. It is important also to notice that the phytochromes proposed by Yao *et al.* fit the requirements of low fluorescence quantum yield, but they still have a remarkable size compared to other fluorescent proteins: 36.67 kDa for BphP1 (134), 30.79 kDA for monomeric GFP (135) and 25.45 kDA of slr1393 (37) belonging to the new promising class of cyanobacteriochromes (CBCRs). Due to their low fluorescence quantum yield and reduced weigth, we think that CBCRs might introduce important improvements in photoacoustic microscopy. For this reason, we will focus this work thesis mainly on this new family of FPs.

PART TWO: EXPERIMENTAL RESULTS

5 Proteins expression and purification

In vitro characterization of the photophysics of fluorescent proteins is a fundamental prerequisite for their application in modern microscopy on living cells.
This chapter focuses on protein engineering, heterologous expression, and purification of two novel mutants of GFP and their engineering. We then report the protocols for expressing and purifying the two GFP mutants and a cyanobacteriochrome. This chapter's protocols mainly come from published work (136–139).

5.1 Engineering of dark mutants of GFPs

As we mentioned in **paragraph 2.2.2**, it is possible to introduce punctual mutations to the sequence of a GFP to vary its spectral properties. The mutation is introduced at the level of the DNA sequence coding for the protein. The approach used to introduce mutations is referred as *site-directed mutagenesis*. Among the possible technical implementations of site-directed mutagenesis, we used the one operating through polymerase chain reaction (PCR)(138). The PCR essentially has the role of amplifying a billion times a DNA fragment. The procedure needs the sample to undergo many thermal cycles in the presence of a thermostable DNA polymerase and requires *primer* oligonucleotides complementary to the target DNA region (**Figure 5.1**). The DNA fragment is denatured to single-stranded DNA at 95°C (at a temperature such that the polymerase is not damaged). The temperature is cooled to down (around 50/60°C) for pairing the single-stranded DNA and the primers; this is called *annealing* temperature. If the temperature is too low, the primers will not pair; if it is too high, they will also pair in other regions, leading to *non-specific* products. The temperature is then raised to 72°C for the extension/elongation phase, where the DNA fragment synthesis is achieved. Polymerization goes on until stopped rising the temperature to 95°C. These cycles, performed through a thermal cycler (also referred to as a PCR machine or DNA amplifier), are repeated many times.

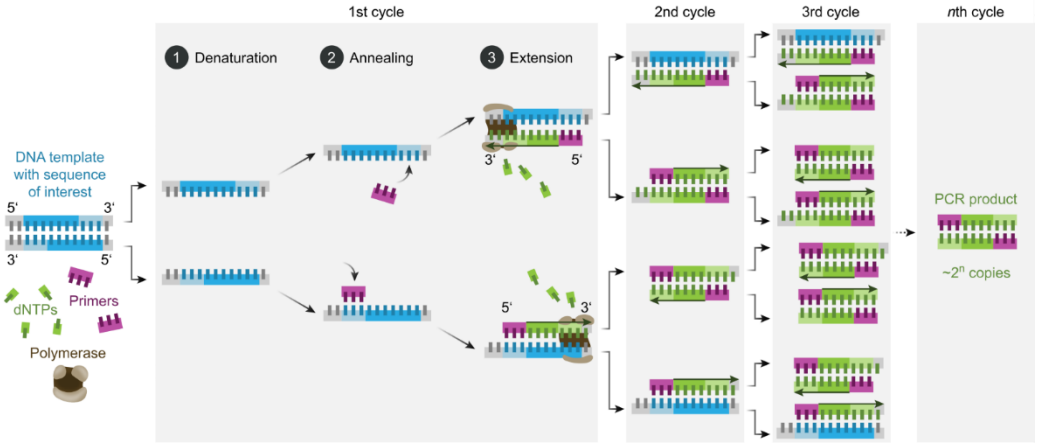

Figure 5.1. Schematic representation of the PCR process. The starting reagents include the interest DNA sequence in appreciable quantity, the enzyme, the primers, and the dNTPs (a

solution of the four deoxynucleoside triphosphates requested by the polymerase to work)—Image reproduced from Wikipedia, Creative Commons BY-SA 4.0.

The DNA coding for mutated GFP is then inserted into host (either prokaryotic or eukaryotic) cells through a plasmid vector. Plasmids are extrachromosomal DNA molecule within a cell that is physically separated from chromosomal DNA and can replicate independently. In *E. Coli* bacterial cells, they are generally in the shape of circular double-stranded DNA and must satisfy some structural requirements: they should contain an *ori* sequence that acts as an origin for replication inside host cells allowing plasmids to replicate as extrachromosomal elements, not depending on the replication of chromosomal DNA. They should contain a selective marker to distinguish cells, including the plasmid, from the others; these selective markers are generally resistant to antibiotics. They should contain a region where it is possible to insert the target DNA (for example, DNA codifying for GFP tagging a specific structure or alone). They should then contain the gene *lacI* codifying for the operon *LacI*, involved in the expression control (**Figure 5.2**).

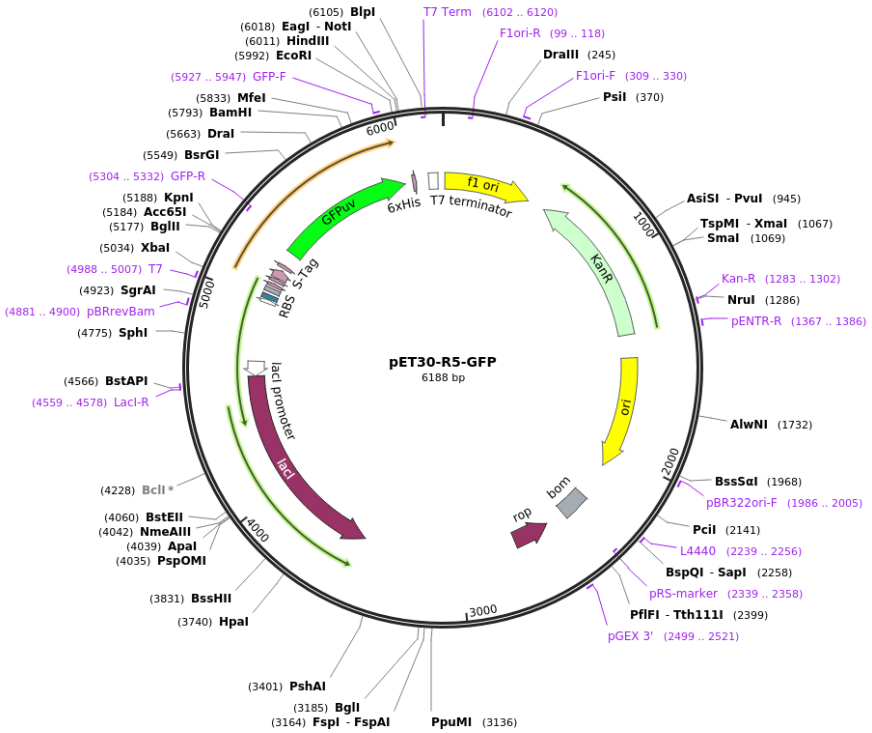

Figure 5.2. Schematic representation of a pET30 plasmid, including the GFP sequence. Colored arrows highlight all the main features. It is crucial to notice the *lacI* gene, the *ori* sequence for the origin of replication, and the sequence codifying for the antibiotic resistance used for selection (Kanamycin). In green is highlighted the sequence codifying for the GFP where the mutagenesis process occurs. Image reproduced from Addgene website.

The core of the mutagenesis through PCR is the primers. In this case, the primer (generally ten nucleotides) pairs with a region of the parental DNA except for one (or at least two) bases. A DNA polymerase with a low proofreading activity is used. Proofreading is the capability of a DNA polymerase to fix newly made nucleotide incorporation errors from the primer terminus before further primer extension. A DNA polymerase with a low proofreading activity will replicate billions of times the DNA strain from the primer with the altered nucleotide without fixing it, generating many copies of the parental DNA, including one or more different bases (the desired mutation). The parental DNA is then digested through an enzyme that removes only methylated DNA (the son DNA is not methylated).

After amplification, an agarose gel electrophoresis is used to analyze the results to investigate the presence of non-specific DNA or investigate the optimal conditions for PCR. Only the sequencing will confirm then the results of PCR.

In this work, we engineered mutants of GFP starting from those reported in reference (35). These are mutants of the wild type, and the enhanced GFP with E222Q mutation added (wildQ and wildQT). As we mention in **paragraph 2.2.2,** this is a punctual mutation introducing photoswitching properties to the GFP. E222Q means that glutamine substitutes glutamate at position 222 in the protein. In terms of nucleotides, it means that, for example, while the codon encoding glutamate is GAA, the one encoding glutamine contained in the primer is CAA, differing for just one nucleotide. We added another mutation from wQ and wQT: Y145W, tryptophane for tyrosine, reported in (140) to generate dark mutants of FPs, characterized by lower fluorescence quantum yield. To indicate the lower fluorescence emission, we term darkwQ the mutant wQ+Y145W and darkwQT the mutant wQT+Y145W.

After obtaining the plasmid encoding for the structure of interest, it is inserted into a system capable of translating the coding sequence of the DNA to a functional protein. The system used is *E. Coli* strains (BL-21 with kanamycin resistance) optimized for this aim. We insert the plasmid through bacterial transformation: the cell membrane becomes temporarily permeable through a thermal shock or an electroporation process. To select only bacteria that included the plasmid, they are grown on a Luria broth-agarose plate containing the proper antibiotic.

5.2 Protein production

The proteins' production requires the upscaling of the translating system. An *E. Coli* suspension transformed with the engineered plasmid in Luria Broth (LB) is spread onto an LB – Agarose plate. The LB is a nutritive medium often used as a culture medium for bacteria. The gel (obtained after agarose polymerization) is functionalized with an antibiotic to select only bacteria that incorporated the plasmid with the antibiotic resistance. Once the bacterial colony incorporating the target DNA is selected, it is necessary to upscale the volume of bacterial suspension to obtain appreciable protein recovery. Generally, a small portion of bacterial suspension (or bacterial growth) is harvested and inoculated in flasks containing liters of LB and antibiotics, and the density

of the bacterial cultured is monitored through the Optical Density (OD) parameter. Since FPs, and recombinant proteins, are secondary metabolites, the OD plays a crucial role: *E. Coli* produces the secondary metabolites in the stationary phase of microbial growth. If a microbial culture's environmental conditions worsen due to the deprivation of nutrients, salts, amino acids or the increase of harmful waste products such as acids or ethanol, the population starts to die, moving the suspension to the death phase. Overpopulation is the main factor leading to these phenomena. OD_{600} represents the scattered light at 600 nm wavelength by the bacterial suspension and can directly relate to the number of microorganisms in very low-density suspensions. After reaching an optimal OD, the temperature is reduced to 28°C to stop bacterial growth, and IPTG is added to induce proteins expression. This compound is a molecular mimic of allolactose, a lactose metabolite that triggers transcription of the *lac* operon, and it is therefore used to induce protein expression where the gene is under the control of the lac operator. After this process, the protein is overexpressed inside the cellular membrane of the cells and must be recovered.

5.3 Protein Extraction and Purification

Generally, the proteins include a His-Tag (145) termination in their genome. The His-Tag is an amino acid motif of nonfunctional histidine at the end of the protein used for affinity purification. The cellular membranes are removed after sonication, and the supernatant containing the proteins is separated from the pellet through centrifugation. The His-Tag motif enhances the affinity for metallic ions (141), and through this property, the supernatant containing the proteins runs over a Nickel functionalized column (Ni-NTA). An elution with imidazole (with a higher affinity to the resin) is performed to obtain free and clean protein. Dialysis on the membrane is necessary to remove the imidazole that denatures proteins. After this process, the three proteins are produced and ready to be characterized in **Chapter 6**.

5.4 Materials and Methods

This paragraph reports the experimental protocols used for the processes expressed in this chapter.

5.4.1 Site-Directed Mutagenesis

The PCR for the site-directed mutagenesis requests the following components:

- 5 µl of buffer (QuikChange II kit, Agilent)
- 3 µl of Quick Solution (QuikChange II kit, Agilent)
- 0.5 µl of DNA obtained through mini prep (Wizard ® PlusSV minipreps DNA purification system).
- 1 µl of dNTPs (QuikChange II kit, Agilent)

- 1.25 µl of primer 1 (Sigma Aldrich)
- 1.25 µl of primer 2 (Sigma Aldrich)
- 1 µl of Turbo DNA polymerase (QuikChange II kit, Agilent)
- 37 µl of water-DEPC (Sigma Aldrich)

After PCR, 1 µl of DPN-I enzyme is added, and the sample is incubated for 1h at 37°C. The enzyme digests the parental methylated DNA. The DNA obtained is transformed into competent *E. Coli* BL-21. We performed the transformation by adding 10 µl to 100 µl of *E. Coli* in ice for 30'. Then the temperature is raised to 30" at 42°C and cooled again for 2'. After that, we added LB, and we kept bacteria under stirring. This process generates pores onto the membrane of bacteria, allowing the plasmid to enter the cell.

5.4.2 Protein Production, Extraction, and Purification

We used the following protocol for three *E. Coli* strains: one containing wQ+Y145W (darkwQ) in pET30 plasmid, one containing wQT+y145W (darwQT) in pET30 plasmid, and the last one, provided by Prof W.Gartner, expressing slr1393 (GAF3). This last strain is double transformed, containing slr1393g in pET30 (the backbone of the proteins) and H01+PcyA in pACYC plasmids; this last portion codifies for the phycocyanobilin-producing enzyme, the chromophore, from hemoglobin. The antibiotics requested are Kanamycin and chloramphenicol for GAF3 and Kanamycin for the two GFPs. The following protocol is adapted from references (35,142). At this point, we have three *E.Coli* strains: one containing wQ+Y145W (darkwQ) in pET30 plasmid, one containing wQT+y145W (darwQT) in pET30 plasmid, and the last one, provided by professor W.Gartner, expressing slr1393 (GAF3). This last strain is double transformed, containing slr1393g in pET30 (the backbone of the proteins) and H01+PcyA in pACYC plasmids. This last portion codifies hemoglobin's phycocyanobilin-producing enzyme (the chromophore). The antibiotics requested are kanamycin and chloramphenicol for GAF3 and Kanamycin for the two GFPs. The following protocol is adapted from references (35,142).

Inoculum preparation. Pre-inoculum preparation: We start from one colony from the glycerol stock, and we added it to 3mL LB + antibiotics 1:1000 in 15mL Falcon®. We shake the Falcon at 220rpm and 37°C for six hours, and then we split the pre-inoculum into three 50mL Falcons® containing 10mL LB + antibiotics 1:1000. Finally, we shake at 220rpm and 37°C overnight. We prepare three 2L flasks containing 1L of LB + antibiotics 1:1000 each. We add the three inoculums to the three flasks, checking the OD_{600} until it reaches 0.5/0.6 (doubling time around 30'). We added 250 µL of IPTG for each flask to induce the protein expression. We left shaking overnight at 28°C and 220rpm (The temperature is crucial for blocking bacterial growth). This latter process moves the bacterial culture to the stationary phase, where protein production occurs.

Pellet recover. We centrifuge the bacterial growth for 15' at 4°C and 6000rcf. We remove the supernatant, suspending then the pellets in 10mL of PBS (NaCl 137mM, KCl 2,7mM,

Na_2HPO_4 10mM, KH_2PO_4 2mM, pH 7.4). We split the 30mL total of pellet/PBS into two 50mL Falcons and centrifuge for 30' removing the PBS. We re-suspend then the pellets with 25mL of sonication solution (TrisHCl 20mM, NaCl 100mM, pH 8 + EDTA-free protease inhibitor in tablets, Roche) and sonicate for 5'. We further lysed the bacterial membranes by adding 5mL of lysing solution (10% Triton X-100 (Sigma Aldrich) + 50uL of DNAse + 50uL of $MgCl_2$ 1M) for 1/2h at 4°C far from light. We recovered the solution and centrifuged it for 1h at 4°C and 11000rpm, recovering the supernatant and trashing the pellets. The supernatant is used to suspend the NinTA (NiNTA Agarose, QIAGEN) resin in a column kept safe from light and under-stirring at 4°C overnight in a bottle.

Column purification. We slowly empty the solution (supernatant/resin) back into the column to allow an optimal arrangement of the resin inside the column, then we wash the bottle twice with 15mL of TrisHCl that we empty into the column. We then elute with TrisHCl + 500mM Imidazole. The imidazole is more affine to the resin than the His-Tagged protein that is then eluted and must be recovered from the column's bottom. It follows the dialysis process for removing the imidazole that may denature the protein in a 30000kDa centrifugal filter (Pall). GAF3 may be further passed over an ion-exchange column (DEAE Sephadex, GE healthcare) to remove the proteins not binding the chromophores.

Proteins' quantification. We characterized protein recovery by calculating the absorbance ratio at 260 nm and 280 nm by a spectrophotometer. GAF3 has a recovery of 1.977 mg/mL, and both darkwQ and darkwQ have a recovery of 2.7 mg/mL. Considering a final volume of 4 mL (10 mL for the GFPs), the total recovered quantity was 7,908 mg for GAF3 and 27 mg for darkwQ and darkwQT.

6 Molecular Spectroscopy for protein dynamics characterization

This chapter offers an overview of the main optical properties of the GFP mutants and the typical experiments performed to validate FPs in fluorescence and photoacoustic microscopy. In the first part of the chapter (**paragraph 6.1**), we explain canonical light-based spectroscopy measurement to investigate the spectral properties of novel photochromic probes. The second part of the chapter (**paragraph 6.2**) offers their subsequent characterization through PA spectroscopy and their application in a 1D PAM experiment.

6.1 Optical Spectroscopy Characterization

After protein engineering, expression, extraction and purification, the resulting solution must be characterized in optical properties before applying FPs as a molecular tag for fluorescence and photoacoustic microscopy. This chapter proposes the light spectroscopy characterization of the three proteins through the acquisition of fluorescence emission/absorption spectra. Characterization of the photoconversion of the two GFP mutants was performed through laser photolysis experiments to retrieve the photo-switching quantum yield. For GAF3, photo-switching quantum yields for forward and reverse reactions are already known.

6.1.1 Dark Mutants of GFP

We have first determined the spectral properties of the new proteins darkwQ and darkwQT by collecting the absorption and emission spectra of the proteins.

6.1.1.1 Absorption/Fluorescence Spectra

Figure 6.1 compares both proteins with the original wQ. At pH ≥ 7, the absorption spectra of darkwQ (**a**) and darkwQT (**b**) in the visible region of the spectrum display a large band centered at 480 nm (**Figure 6.1**, solid black line) corresponding to the state *on* of the chromophore. It is interesting to notice that the profile of the darkwQT absorption spectrum is similar to the one in the original wQ but slightly blue-shifted, while the one for darkwQ is much different (35). For both proteins, illumination on the high-energy tail (488 nm) of the absorption spectrum of the *on*-state leads to a green fluorescence emission that mirrors the absorption spectrum (**Figure 6.1**, black dashed line). It is possible to retrieve the fluorescence quantum yield of the darkwQ and the darkwQT by comparison with the original wQ. Using wQ (**Figure 6.1**, green solid and dashed lines) as a reference with a known fluorescence quantum yield of 0.45 (35), the fluorescence yields for darkwQ and darkwQT can be calculated as 0.086 and 0.043, respectively. Interestingly, even if the original wQT has a higher fluorescence quantum yield (0.71) compared to wQ (0.45), darkwQT has a lower one than darkwQ.

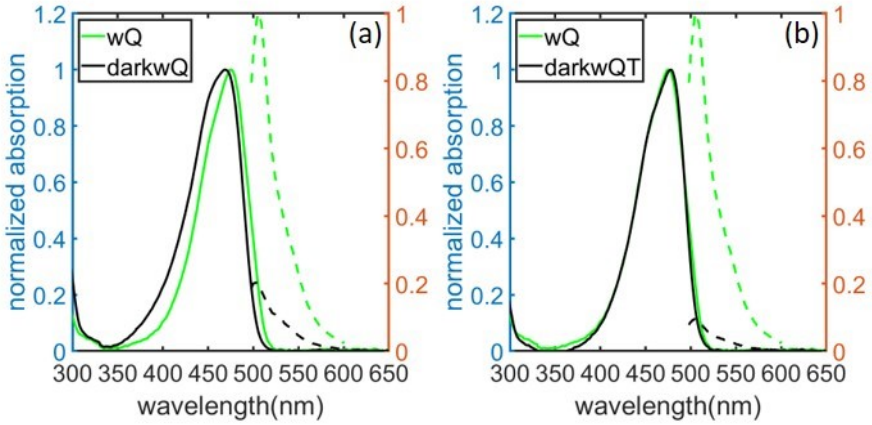

Figure 6.1. (**a**) A plot of absorbance (solid line) and fluorescence (dashed line) of both wQ (green) and darkwQ (black). (**b**) A plot of absorbance (solid line) and fluorescence (dashed line) of both wQ (green) and darkwQT (black). Absorbance is normalized for their absorption maximum, while fluorescence is normalized for the maximum of fluorescence of the original wQ.

In **Figure 6.2**, we report the photoconversion between the *on* and the *off* state of darkwQ (**a**) and darkwQT (**b**). The photoconversion between the two optical states occurs for the isomerization of p-HBI, as shown in **Figure 2.8** (**a**). For the parental proteins, wQ and wQT, irradiation of the peak centered at 480 nm with a 488 nm laser leads to the formation of a sideband, corresponding to the *off* state, centered at 400 nm and the reduction of the main band (35). The subsequent irradiation with 405 nm laser restores then the main band. Differently from wQ and wQT, the absorption spectra of darkwQ and darkwQT display one single band centered at ≈480 nm, and the irradiation at the main peak behaves differently: the absorption spectrum is almost unchanged for darkwQT upon 488 nm excitation while the same illumination decreases the single band of the darkwQ absorption spectrum. Changes in the absorption spectrum eventually lead to changes in the emission spectrum. Excitation with 405 nm wavelength partially restores the band in darkwQ.

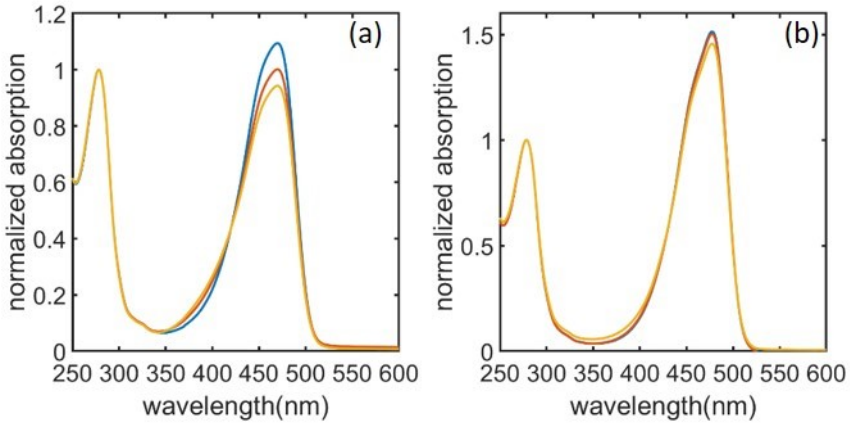

Figure 6.2. (**a**) Photoconversion of darkwQ. (**b**) Photoconversion of darkwQT.

6.1.1.2 Photolysis with transient absorption detection

Flash Photolysis (and photolysis with transient absortpion detection) is a technique used to study fast light-dependent reactions and was originally developed during World War II as an approach to develop cameras fast enough to capture enemy missiles. The technique was originally developed by George Porter (later Lord Porter of Luddenham) and Ronald Norrish in 1949, and their achievements were subsequently recognized with the Nobel Prize in Chemistry awarded in 1967 (143). Flash Photolysis is a pump-probe technique in which the sample is first excited by a short-pulse source such as a pulsed laser or a flash lamp. The pump laser excites a molecule into a reactive state, and from there, it is possible to measure the reaction spectroscopically, using a light beam to measure absorbance changes in time. Current implementations exploit nanosecond pulsed lasers (nanosecond laser flash photolysis) or ultrafast laser sources (pump-probe transient absorption) to produce reactive excited states, which are then probed by monitoring the concomitant absorption changes. We have used a laser photolysis setup where excitation is achieved by a CW laser (0.5 kW/cm^2), and the sample is exposed to the beam for time intervals spanning from 1 s to 20 s. By measuring the absorbance at different exposure times, it is possible to obtain the switching quantum yield after linear fitting the obtained curve. In **Table 6.1**, we report the experimental points used for data fitting. The fluence (ϕ) is obtained as the product between the exposition time and the power of the laser expressed in kW/cm^2 so that the final units are mW*s/cm^2. The absorbance is reported as a variation in the logarithmic scale and normalized for the maximum value $\ln(1 - \Delta A/A^0)$. The final equation used for fitting is then $\ln(1 - \Delta A/A^0) = 2303 \cdot \varphi_{on} \cdot \varepsilon \cdot \phi$ (**Equation AII-6**). For both proteins, we obtained an absorbance graph *vs*. power whose trend is linear for low power. We fitted them in this region, considering that the slope of the curve is equal to:

$$p = \frac{2303 * \varepsilon_{488} * Einstein}{\pi * r^2} \varphi$$

Equation 6.1

Where ε_{488} is the absorption coefficient at 488 nm, and $Einstein$ is a conversion factor from $W \cdot s/Einstein = {\lambda}/{1.19 * 10^8}$. r is the beam diameter striking the cuvette equal to 1mm. To better comprehend **Equation 6.1**, see the full derivation in **APPENDIX II**: Basis of Photolysis with transient absorption detection.

Table 6.1. A table containing the experimental points used for fitting.

darkwQ		*darkwQT*	
$\phi(mW \cdot s/cm^2)$	$\ln(1 - \Delta A/A^0)$	$\phi(mW \cdot s/cm^2)$	$\ln(1 - \Delta A/A^0)$
0	0	0	0
0,59	0,058	0,55	0,024
0,99	0,090	1,67	0,029
1,92	0,185	2,85	0,066
2,14	0,196	22,42	0,121
3,74	0,246	44,42	0,143
22,64	0,308	65,57	0,163
46,66	0,368	92,52	0,173
87,76	0,392		

Fitting was performed in the linear region of **Figure 6.3**. For darkwQ (**a**) and darkwQT (**b**), we evaluate *off→on* photoconversion quantum yields of $\varphi_{on} = 1.09 * 10^{-3}$ and $\varphi_{on} = 5.48 * 10^{-3}$, respectively, comparable with those reported in reference (35).

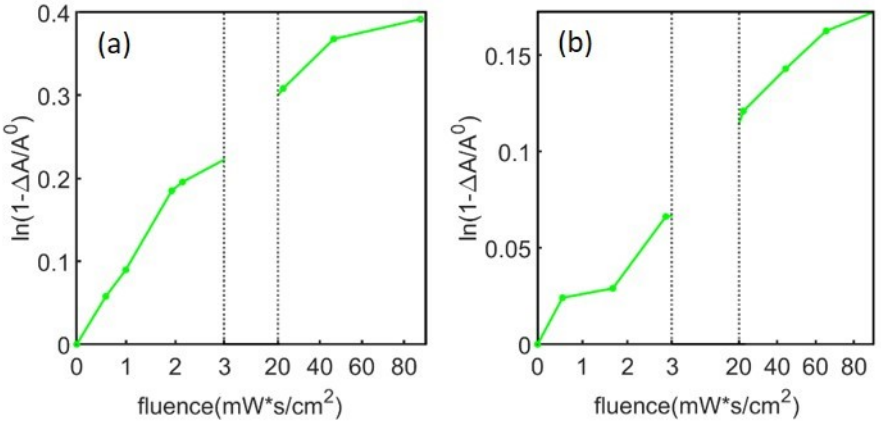

Figure 6.3. A plot of the data used for fitting. We report the absorbance as a function of the laser power used. (**a**) darkwQ. (**b**) darkwQT. The first break highlights the linear region considered for fitting operations. The linear region is more evident for darkwQ (**a**).

The low photoconversion yield of the two mutants and their very small spectral changes upon photoconversion make the two weakly-fluorescent proteins less interesting for further consideration in photoacoustic applications.

6.1.2 GAF3 from slr1393

The photophysical properties of GAF3 from slr1393 are well characterized, and data related to optical properties come from references (142,144). In the following paragraph, we mostly concentrate on the photoacoustic signals generated by photoexcitation of the protein.

6.1.2.1 Absorption/Fluorescence Spectra

GAF3 from slr1393 is a photochromic protein switching between a red absorbing parental ($GAF3_R$) state and a green absorbing one ($GAF3_G$). The photoswitching between these two states occurs upon red irradiation (633/670 nm) for the red→green transition and green irradiation (513/540 nm) for the green→red transition. $GAF3_R$ absorption spectrum displays a large band centered on 650 nm (absorption maximum at 649 nm), while $GAF3_G$ has its absorption peak centered at 536 nm (**Figure 6.4**). Upon conversion between the two forms, the absorption spectra of GAF3 show an isosbestic point at 590 nm. The excitation at the isosbestic point leads to an emission mirroring the absorption for $GAF3_G$ and a slightly different one for $GAF3_R$. It is important to notice the higher Stokes shift (≈100 nm) revealed for $GAF3_G$ compared to $GAF3_R$ (≈30 nm). $GAF3_R$ has a higher fluorescence quantum yield ($\phi_{F,GAF3_R} = 0.1$), compared to $GAF3_G$ ($\phi_{F,GAF3_G} = 0.06$). The photoconversion process was previously characterized using nanosecond and CW photolysis. The quantum yield of conversion green→red ($\phi_{GR} = 0.30$) is higher than the one for conversion red→green ($\phi_{RG} = 0.09$), making $GAF3_R$ the parental state. The photoconversion quantum yields of $GAF3_R$ are at least one order of magnitude higher than those of GFP derivatives. Moreover, the spectral shift between the two species is huge, exceeding 100 nm. Being characterized by high photoconversion yield and large changes in extinction coefficient, GAF3 is considered a promising contrast agent for photochromic photoacoustic applications, and we will study it in detail in the following paragraphs.

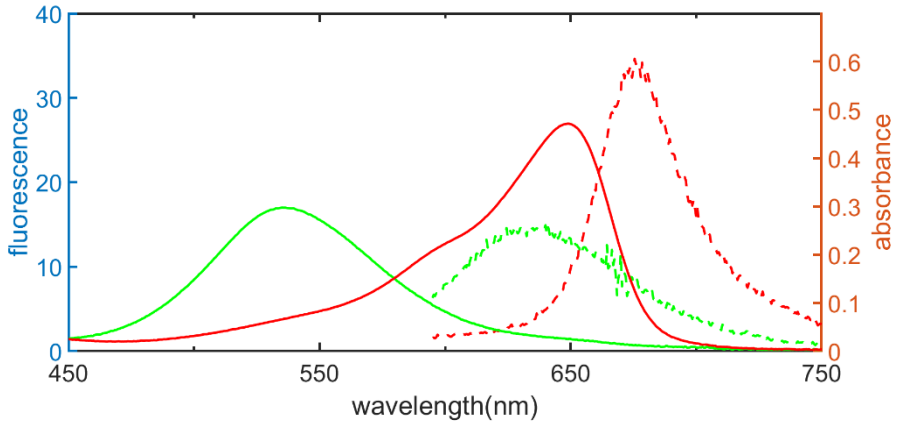

Figure 6.4. Absorption/Fluorescence spectra of GAF3. Solid lines show the absorption spectra of $GAF3_G$ (green) and $GAF3_R$ (red), and dashed lines show the fluorescence spectra of $GAF3_G$ (green) and $GAF3_R$ (red). Data adapted from reference (142).

6.2 Photoacoustic Spectroscopy Characterization

We have collected the photoacoustic signals for one of the two GFP mutants and GAF3. The GFP mutant's PA signal showed a much smaller photochromic response than expected. After an initial assessment, we did not further deepen the PA analysis. On the contrary, a thorough investigation of GAF3 started from a reevaluation of enthalpic and volumetric signals for the two photoconversion processes, taking advantage of a slightly better time resolution of the current experimental layout compared to previous determinations. We then collected photochromic photoacoustic spectra of the two GAF3 species, and we studied how we can exploit the changes in the PA signal due to the photochromic transformation to obtain a strong contrast over scattering or absorbing background and identify the spatial distribution of GAF3 containing structures in a model 1D scanning detection system.

6.2.1 Optical Setup

The experimental layout (**Figure 6.5**) is obtained by modifying a previously reported setup (144). A nanosecond laser (Nd:YAG) tuned by an optical parametric oscillator (OPO) of an Integra system (GWU-Lasertechnik Vertriebsges. GmbH, Germany) provides the excitation PA signals. Depending on the species, the output at 410/470 nm for GFP mutants and 540/650 nm for GAF3 was selected. The repetition rate was kept at 5 Hz, and the laser pulse energy was monitored with an energy meter during data acquisition. A piezoelectric transducer (Panametrics, V-103, 1 MHz) detects the PA signal that, after 54 dB pre-amplification (Panametrics model 5662 ultrasonic preamplifier, 0.5-5 MHz, 54-dB gain), is fed into a digital oscilloscope (LeCroy 9370) operating at 500 MS/s in a 10 µs time window, and finally transferred to a personal computer for further elaboration. Each PA signal was an average of 100 shots. A 1 cm x 1 cm quartz cuvette (Hellma™) with four

optical windows was inserted into a sample holder with a piece of aluminum foil placed between the cuvette and the piezoelectric transducer to reflect stray light from the pulsed laser beam preventing the generation of a large-amplitude acoustic wave by direct absorption of photons by the transducer's surface. A temperature-controlled sample holder (TASC 300, Quantum Northwest, Spokane, WA, USA, 0.02°C of stability) stabilizes the temperature of the quartz cuvette containing the sample and thin layers of vacuum grease between the cuvette, the aluminum foil, and the transducer match the components acoustically. A vertical 270 µm slit, shaping the beam laser (corresponding to an acoustic transit time of roughly 200 ns)(145), provides a time resolution of 20 ns after the deconvolution of the PA signal (146,147).

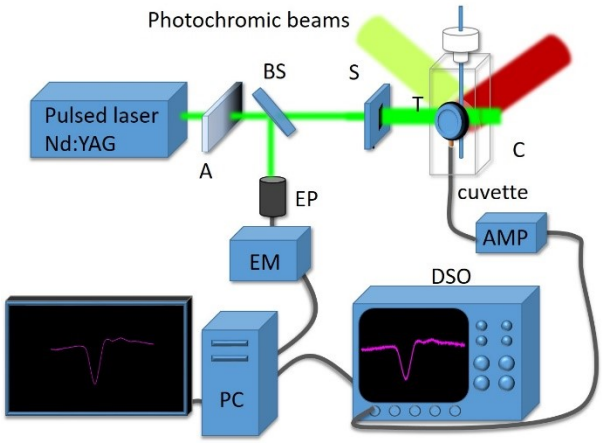

Figure 6.5. Schematic sketch of the PA spectroscope used for measurements. A pulsed laser was used to induce PA waves within the sample. A is an attenuator, BS is a beam splitter, S is the slit shaping the beam. The signal is acquired from the sample placed in the cuvette C through the ultrasound transducer T. The photochromic beams come perpendicularly to the surface of the transducer (red and green beams). The cuvette may include a capillary. The signal from T is amplified (AMP) and fed to a Digital Oscilloscope (DSO). A portion of the beam (around 10%) is deflected by the beam splitter to an energy probe (EP) connected to an energy meter (EM) and is used as a normalization factor for the waveforms. The signals are transferred to and analyzed by a personal computer (PC). The cuvette holder can be moved perpendicularly to the transducer.

For experiments in homogenous solutions, photoconversion from $GAF3_G$ to $GAF3_R$ state was achieved by the CW emission at 514 nm of a multiline argon-ion laser (JDS Uniphase 150 mW all lines). The reverse photoconversion was induced using the 633 nm output of a HeNe laser (30 mW) and the 670 nm output of a diode laser (3 mW), while the photoconversion from $darkwQT_{on}$ to $darkwQT_{off}$ was achieved through the 488 nm emission of the previous multiline argon-ion laser, while the reverse photoconversion was obtained through a 405 nm diode laser. Two shutters allow the laser line selection with the shutter drivers operating oppositely (Uniblitz, Vincent Associates Inc., Rochester, NY,

USA). The photoconversion laser was kept on during the collection of PA signals to prevent the accumulation of photoproducts generated by the pulsed excitation, forcing the proteins to stay in one of their states. The photoconversion beams entered the cuvette perpendicularly to the transducer. The absorption of the light of the photoconversion beam from the transducers' surface results in a nondetectable signal.

6.2.2 Dark Mutants of GFP

As we mentioned, dark mutants of GFP did not show any interesting properties in terms of photoconversion and this reflected on PA properties.

6.2.2.1 Photochromic Properties

Among the two GFP mutants, darkwQ showed the best photoswitching properties. We thus collected photoacoustic (**Figure 6.6**) signals under excitation at 410 (**a**) or 470 (**b**) nm for the two species (darkwQ$_{off}$ and darkwQ$_{on}$). To probe the *on* state, a pulsed excitation at 470 nm was used in combination with a photoconversion laser at 405 nm to force the protein to remain in that optical state. At the same time, a pulsed 410 nm excitation, and a 488 nm CW laser was used to probe the *off* state for photoconversion. The contrast between the two signals is evaluated to be around two in the best case, reflecting the poor properties of photoswitching previously demonstrated.

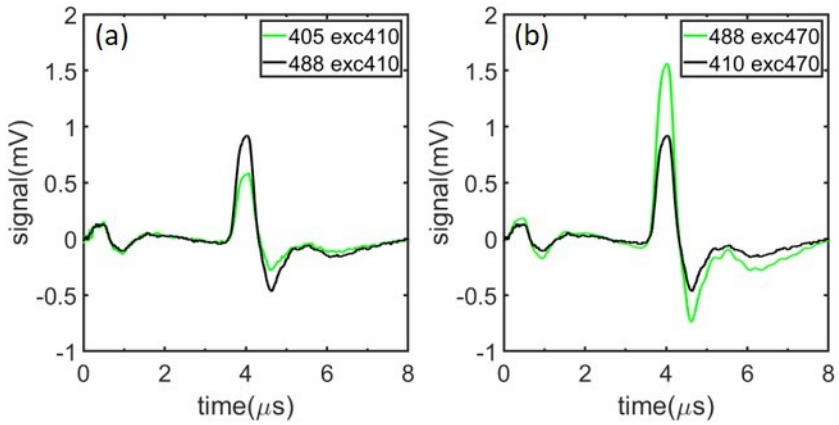

Figure 6.6. (**a**) PA signal for the solution of darkwQ excited at 410 nm (green darkwQ$_{on}$, black darkwQ$_{off}$). (**b**) PA signal for the solution of darkwQT excited at 470 nm (green darkwQT$_{on}$, black darkwQT$_{off}$).

6.2.3 GAF3 from slrl1393

Compared to the two GFPs, GAF3 showed better photochromic properties. Its photoswitching quantum yields are higher than those evaluated for the dark mutants of GFP, and the change in absorption coefficient is by far larger. For this reason, GAF3 has adequately been receiving more attention in this work. The analysis moved from more

spectroscopic studies aimed at determining kinetic and thermodynamic properties to studies intended to provide preliminary information for future microscopy applications.

6.2.3.1 Photochromic properties and Photoacoustic Spectra

After baseline correction and normalization, the PA waveforms for $GAF3_R$ and $GAF3_G$ solutions at room temperature were collected as a function of the pulsed laser excitation wavelength of 450-670 nm. The amplitude of the first positive oscillation of the waveform was taken as a measure of the signal intensity and plotted against the wavelength to have an action spectrum. With PA detection, it is possible to exploit the photochromic properties of GAF3 to increase the contrast in sensing the compound in the presence of background-absorbing media. **Figure 6.7** (**b, c**) compares the PA signals observed for $GAF3_G$ and $GAF3_R$ after excitation in the main absorption bands of the two species demonstrating that upon pulsed excitation at 540 (**Figure 6.7**, **c**) nm and concomitant 633/670 nm CW excitation, a large and stable PA signal is observed for $GAF3_G$ (green curve). The $GAF3_R$ generation upon CW photoconversion with 514 nm light strongly reduces the PA signal (≈4-fold). The ratio between the PA signal amplitudes is in keeping with the change in molar absorption coefficient at this wavelength. Using a 650 nm pulsed excitation, the ratio between PA signal amplitudes upon conversion from $GAF3_R$ (initially generated through 514 nm CW excitation) and $GAF3_G$ (obtained by 633/670 nm CW excitation) is similar (≈4.5-fold, **Figure 6.7**, **b**). The smaller than expected change in amplitude under 650 nm excitation, based on the absorption coefficients of $GAF3_R$ and $GAF3_R$ (≈15-fold), is attributed to incomplete conversion under the employed experimental conditions.

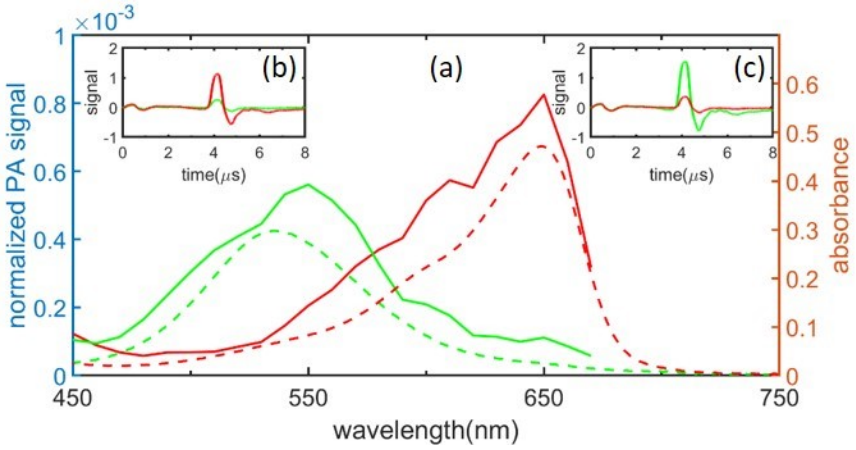

Figure 6.7. Inset (**c**). Energy-normalized PA signals for a GAF3 solution excited at 540 nm (green, $GAF3_G$; red, $GAF3_R$). Inset (**b**). Energy normalized PA signals for a GAF3 solution excited at 650 nm (green, $GAF3_G$; red, $GAF3_R$). Main spectra (**a**). PA signal amplitude for $GAF3_G$ (green dotted line) and $GAF3_R$ (red dotted line) function of excitation wavelength. Signal amplitudes were estimated from the first positive oscillation (at ≈4 μs) and normalized for laser pulse energy. The

corresponding absorption spectra are reported as solid green and solid red lines for comparison. T = 20 °C. [GAF3] = 5 μM.

The action spectra of GAF3 (**Figure 6.7**, **a**, dashed lines) are obtained as in the previous experiments: we collected PA signals for $GAF3_G$ ($GAF3_R$) under 633/670 nm (514 nm) CW illumination. The insets in **Figure 6.7** report the PA signal intensity measured at 540/650 nm excitation for $GAF3_R$ and $GAF3_G$ at 650 nm (**b**) and 540 nm (**c**) excitation wavelength. The main plot (**Figure 6.7**, **a**) compares the PA signal intensity as a function of the pulsed excitation wavelength for $GAF3_G$ (solid green curve) and $GAF3_R$ (solid red curve). It is possible to see a good agreement between the absorption spectra (green and dashed red curve) and the normalized PA spectra in green and solid red curves. In particular, the red curve perfectly overlaps the PA spectrum for $GAF3_R$. The agreement is not perfect for $GAF3_G$. We attributed this effect to wavelength-dependent incomplete conversion of GAF3 in the range where absorption spectra strongly overlap, which may also reflect the larger green to red photoconversion yield.

6.2.3.2 Photochromic Photoacoustic signals in the presence of competitive absorbers

Likewise happening in fluorescence microscopy, the photochromic modulation of the PA signal amplitude generated by GAF3 allows distinguishing its contribution in the presence of absorbing, non-photochromic compounds. This process mimics the situation encountered in tissues, where other absorbers are present, most likely not showing modulated signals from photochromic conversion. As a simple case, we acquired the PA signal of a GAF3 solution exciting at 650 nm and 540 nm for $GAF3_R$ and $GAF3_G$, in the presence of absorbance by a co-solute, Brilliant Black BN (BBBN), at increasing concentrations, to emulate the competitive absorption. The absorbance of $GAF3_R$ at 650 nm and $GAF3_G$ at 540 nm were, respectively, 0.22 and 0.14. The range of competitive absorbance by BBBN was 0-0.5 at 540 nm and 0-0.75 at 650 nm. **Figure 6.8** compares selected PA signals for $GAF3_R$ and $GAF3_G$ after excitation at 540 nm (**a**) or 650 nm (**c**) for the highest BBBN concentration investigated, corresponding to an absorbance of 0.5 at 540 nm and 0.75 at 650 nm. Although the non-adjustable PA signal is quite intense, the adjustable fraction is evident in the plots, giving rise to reasonably high contrast (**Figure 6.8**, **b,d**).

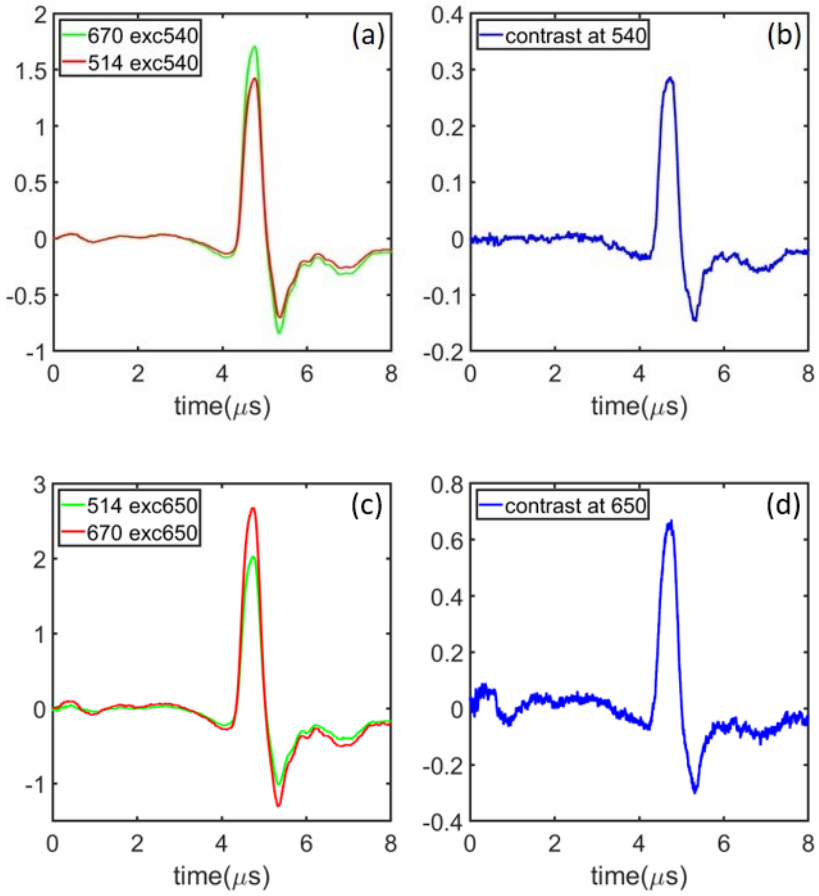

Figure 6.8. PA signals for $GAF3_R$ (red curves) and $GAF3_G$ (green curves) solutions after excitation at 540 nm (**a**) or 650 nm (**c**). The solutions also contained BBBN at a concentration corresponding to an absorbance of 0.5 at 540 nm and 0.75 at 650 nm. The difference between PA signals at 540 nm ($GAF3_G$ minus $GAF3_R$, **b**) and 650 nm ($GAF3_R$ minus $GAF3_G$, **d**) shows a solid contrast even in a competitive absorber.

6.2.3.3 Photochromic photoacoustic signals in the presence of scattering media

After studies on purified protein, we performed experiments on *E. Coli* suspensions overexpressing the protein. This situation expands the previous configuration with competitive absorbance to mimic a scattering environment and the possible presence of unknown, non-photochromic chromophores. A suspension of bacteria with an OD of 0.6 at 650 nm is used primarily due to light scattering from the bacterial suspension. **Figure 6.9** shows the PA signals for an *E. Coli* suspension overexpressing GAF3 after excitation at 540 nm (**a**) or 650 nm (**c**) for $GAF3_R$ (red lines) and $GAF3_G$ (green lines) with the intensity of the signal of $GAF3_R$ in (**a**) much more significant than expected with an abnormal signal shape in the first part of the signal. We attribute this evidence to a competitive, non-photochromic species in the bacterial suspension, absorbing mainly at 540 nm. On the contrary, the $GAF3_G$ signal in panel (**c**) is consistent with expectations and does not

suggest the presence of additional competitive absorbers. The magnitude of the PA signal intensity (contrast) change can be evaluated by subtracting the two waveforms (panels b and d). The contrast is much better for the red absorbing species exploiting the 650 nm absorption band. As observed previously, due to incomplete conversion, the ratio between signals in (**d**) and (**b**) (≈7) is not exactly matching the ratio between absorption coefficients of $GAF3_R$ and $GAF3_G$. The experiment shows that it is possible to identify the contribution to the photoacoustic signal arising from the photochromic protein inside the bacteria.

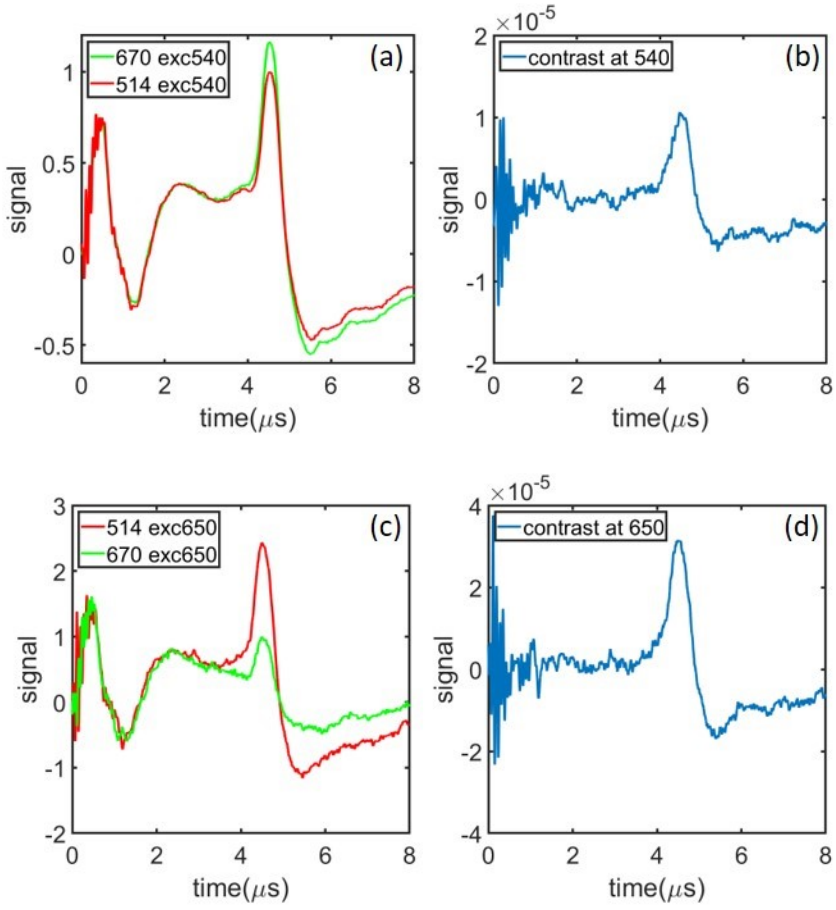

Figure 6.9. PA signals for a suspension of *E. coli* overexpressing GAF3 after excitation at 540 nm (**a**) or 650 nm (**c**) for $GAF3_R$ (red signals) and $GAF3_G$ (green signals). After baseline subtraction and laser pulse energy normalization, signals were normalized to the lower amplitude waveform ($GAF3_R$ in the top left and $GAF3_G$ in the bottom left). In panels (**b**) and (**d**), we plot the two forms' contrast by subtracting the two PA signals.

6.2.3.4 Photochromic photoacoustic signals from a capillary tube

To test the capability to retrieve spatial information exploiting the photochromic PA signal by GAF3, we have placed a capillary tube filled with a solution containing GAF3 under

various conditions to realize a simple phantom. We then scanned the laser beam horizontally to test the imaging capability in this 1D, simplified scheme.

A 1 cm x 1 cm plastic cuvette (Sigma-Aldrich) with four optical windows was placed into the PA sample holder, and a small cylindrical glass capillary tube (outer diameter 1.6 mm, inner diameter 1.0 mm) sealed at the bottom vertically entered the cuvette (**Figure 6.10**, **a**) containing the solution of interest (a Brilliant Black BN solution, a GAF3 solution, or a suspension of *E. Coli* expressing GAF3). Depending on the experiment, the cuvette was filled with water, a BBBN solution, or an *E. Coli* bacterial suspension. The beam's position (shaped by the 270 µm vertical slit) was scanned horizontally through the cuvette (**Figure 6.10**, **b**) using a micro-positioning translation stage. PA signals were collected at positions separated by 200 µm steps. Photoconversion beams for these experiments were obtained by coupling a frequency-doubled CW Nd:YAG laser (100 mW) or a high-power LED (central wavelength 670 nm, 50 mW) to a fiber bundle. The beam entered the cuvette at a right angle to the pulsed laser beam, filling the capillary volume.

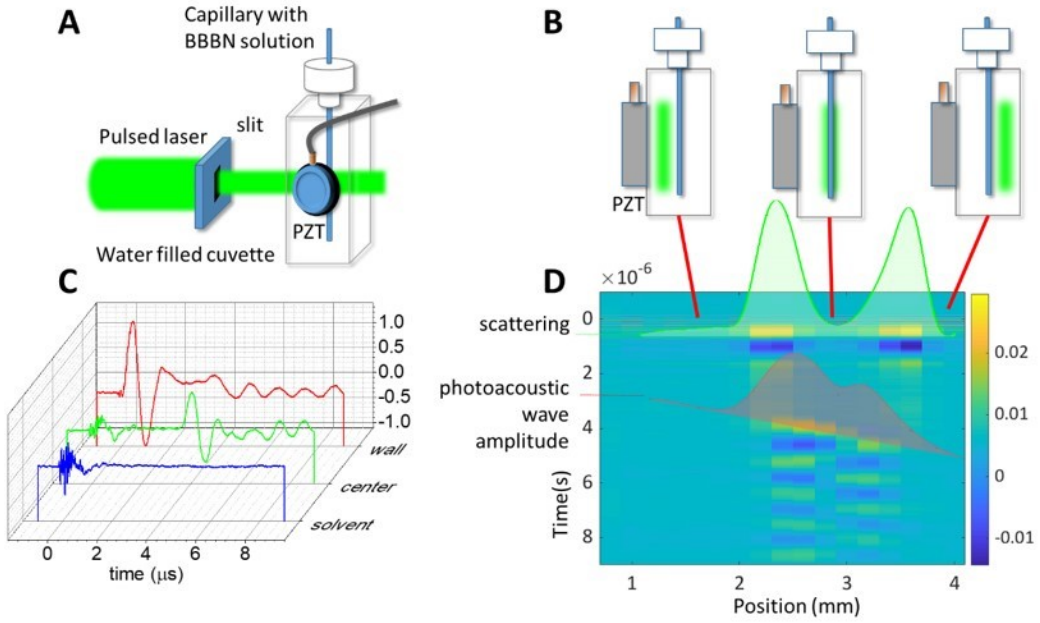

Figure 6.10. (**a**) Schematic representation of the cuvette with the capillary tube, the laser beam, and the piezoelectric transducer (PZT). (**b**) Front view of the cuvette with the capillary and the laser beam at three different positions (passing to the left, through the center, or to the right of the capillary). (**c**) Representative waveforms collected with the laser beam passing through the solvent (blue), the center of the capillary (green), or the capillary wall (red). The capillary contained a BBBN solution with 0.5 (1 cm pathlength) absorbance at the excitation wavelength. The oscillation starting at time ≈0 s at all positions is due to the scattered light absorbed by the transducer's surface. The oscillation starting at about 3.5 µs in the green waveform is due to the signal generated upon absorption by the solution inside the capillary. The scattering signal

becomes very large when the laser beam hits the capillary wall (red), and a smaller amplitude oscillation is appreciable at about 4 μs due to the absorption of the laser beam by the solution inside the capillary. To emphasize the scattering signal, we collected these data without the aluminum foil between the cuvette and transducer (which was present in all other experiments) to emphasize the scattering signal. (**d**) Contour plot of the PA signals collected at different beam positions inside the cuvette. The signal due to laser scattering is observed at t≈0 s at all beam positions. The width of this signal (solid green line) estimates the external diameter of the capillary (1.6±0.2 mm FWHM), consistent with the direct measurement using a caliper. Due to the finite speed of sound (≈1500 m/s in water), the signal from absorption by the solutions inside the capillary is observed at increasing delay when the cuvette is scanned, and the distance between the transducer the beam increases. The red shaded area reports the amplitude of the acoustic wave generated inside the capillary, whose time-position dependence nicely reproduces the speed of sound in the solvent (≈1500 m/s). The width of the red curve (FWHM) is 1.0±0.2 mm, identical to the one measured through an optical microscope with a calibrated ruler.

In **Figure 6.11** (**b**), we report selected signals collected for $GAF3_R$ (red line) and $GAF3_G$ (green line) under 650 nm excitation, at the center of the capillary tube, along with their difference (blue line), showing evidence that the photoacoustic wave for $GAF3_R$ is larger than the one for $GAF3_G$. Similar results were obtained under 540 nm excitation, the only difference being an overall smaller amplitude of the PA signals due to lower absorbance at this wavelength**. Figure 6.11** (**c**) reports the contour plot representation of the signals for $GAF3_G$ and $GAF3_R$ collected for the beam at different positions across the cuvette, showing the increase in the arrival time of the PA wave generated by the protein, as already observed in **Figure 6.10** (**d**). The plot of the amplitude of the first maximum of the acoustic wave for $GAF3_R$ as a function of the beam position (**Figure 6.11**, **d**, *left*) increases when the beam hits the solutions inside the capillary tube, quickly identifying the position of the capillary. The signal is much smaller for $GAF3_G$ (**Figure 6.11**, **d**, *center*). The right panel of **Figure 6.11** (**d**) estimates the contrast in identifying the spatial distribution of GAF3 by subtracting the signals corresponding to the two shapes of the protein. It is worth noting that the signal becomes slightly smaller near the capillary center, possibly due to optical interference caused by the curved capillary surface.

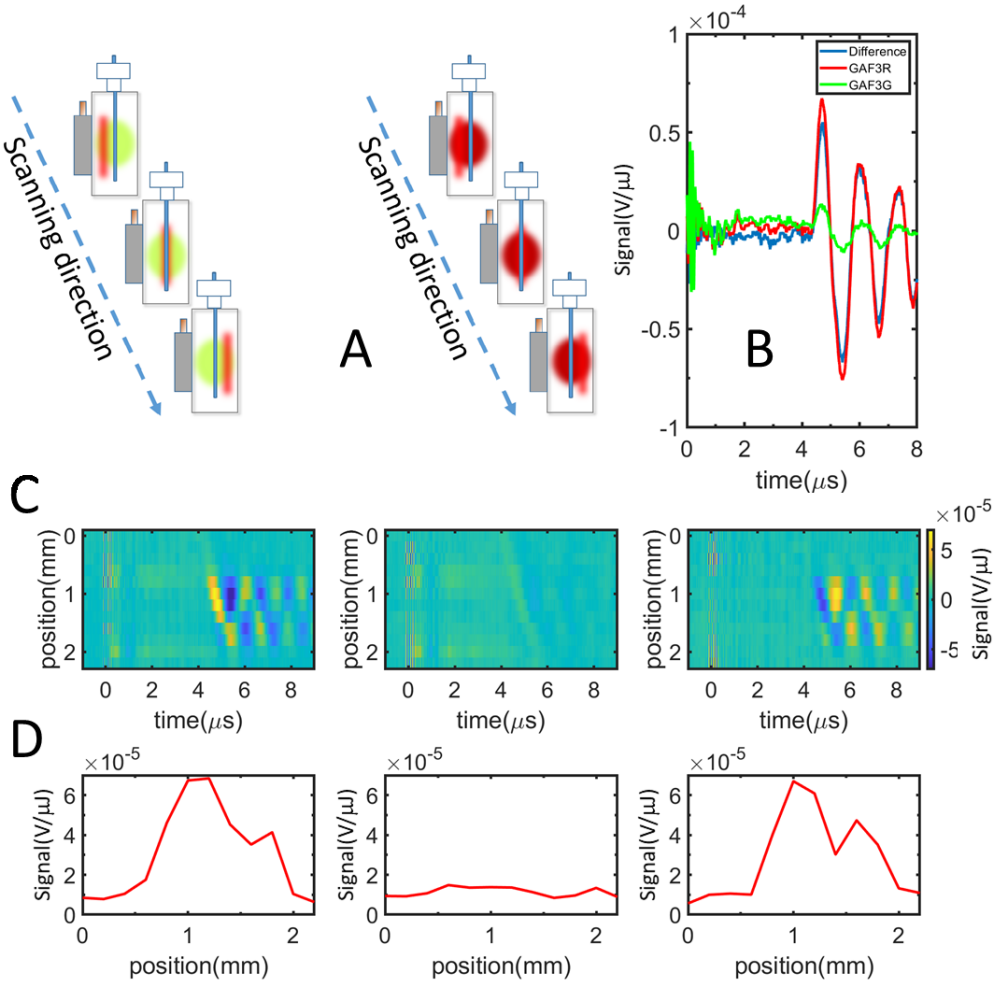

Figure 6.11. Capillary tube experiment for a 5 µM GAF3 solution. The cuvette is filled with deionized water (**b**, **c**, and **d**). The competitive absorbance of the BBBN solution was 0.75 (1 cm pathlength) at 650 nm, where excitation was performed. (**a**) Schematic of the geometrical arrangement of the pump beam (vertical slit), the photoconversion beam (red or green circles), and the capillary tube at different pump beam scanning positions for $GAF3_R$ (*left*) and $GAF3_G$ (*right*). (**b**) PA signals were collected at the center of the capillary for $GAF3_R$ (red), $GAF3_G$ (green), and the difference between the signals (blue). (**c**) Contour plot of the PA signals as a function of time and position of the beam in the cuvette for $GAF3_G$ (*left*), $GAF3_R$ (*center*), and the difference between the two signals (*right*). (**d**) The amplitude of the first positive PA oscillation for $GAF3_R$ (*left*), $GAF3_G$ (*center*) and the difference between the two signals (*right*) as a function of the excitation beam position inside the cuvette.

In the following step, an *E. Coli* suspension overexpressing GAF3 is placed inside the capillary to test the capability to retrieve the spatial information of the photochromic PA signal when the capillary is immersed in water in a BBBN solution (to model competitive absorption) or in an *E. Coli* suspension with OD (650 nm) = 0.6 (to model the presence of a non-absorbing scattering medium). While pulsed excitation at 540 nm does not lead to

satisfactory results (**Figure 6.12**, **Figure 6.14**, **Figure 6.16**), excitation at 650 nm can retrieve the position of the capillary under all tested conditions shown in **Figure 6.11** (**Figure 6.13**, **Figure 6.15**, **Figure 6.17**).

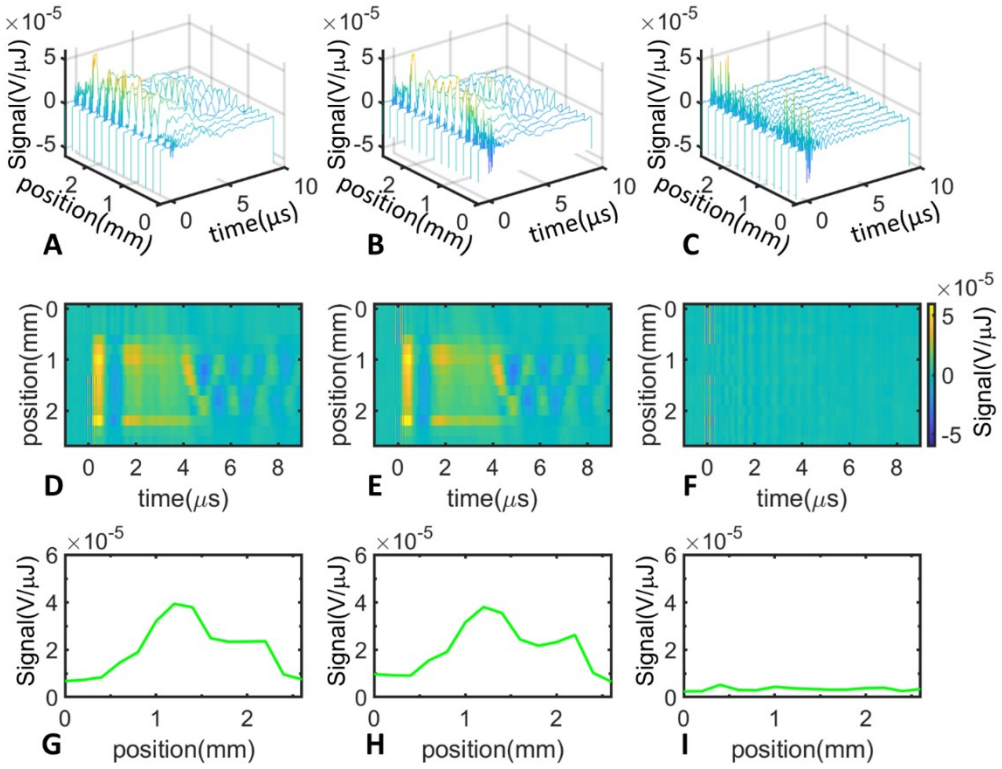

Figure 6.12. Photoacoustic signals were collected for a capillary tube filled with a transformed *E. Coli* (overexpressing GAF3) bacterial suspension immersed in a water-filled cuvette. Pulsed excitation was at 540 nm, T = 20 °C. The top row (**a-c**) reports waterfall plots of the photoacoustic signals as a function of time and the position of the excitation beam inside the cuvette for $GAF3_R$ (**a**), $GAF3_G$ (**b**), and the $GAF3_G$ - $GAF3_R$ difference (**c**). The center row (**d-f**) shows the contour plots for the signals in (**a-c**). The bottom row (**g-i**) shows the amplitude of the first positive oscillation of the PA signals in (**a-c**) as a function of the excitation beam position inside the cuvette.

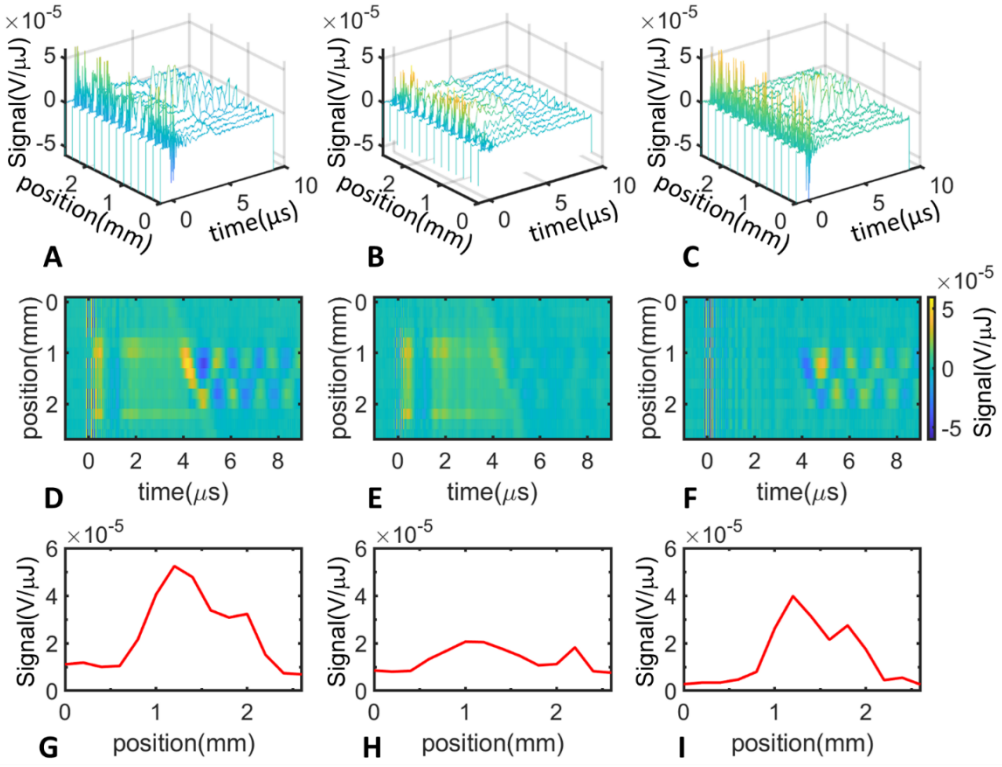

Figure 6.13. Photoacoustic signals were collected for a capillary tube filled with a transformed *E. Coli* (overexpressing GAF3) bacterial suspension immersed in a water-filled cuvette. Pulsed excitation was at 650 nm, T = 20 °C. The top row (**a-c**) reports waterfall plots of the photoacoustic signals as a function of time and of the position of the excitation beam inside the cuvette for $GAF3_R$ (**a**), $GAF3_G$ (**b**), and the $GAF3_R$ - $GAF3_G$ difference (**c**). The center row (**d-f**) shows the contour plots for the signals in (**a-c**). The bottom row (**g-i**) shows the amplitude of the first positive oscillation of the PA signals in (**a-c**) as a function of the excitation beam position inside the cuvette.

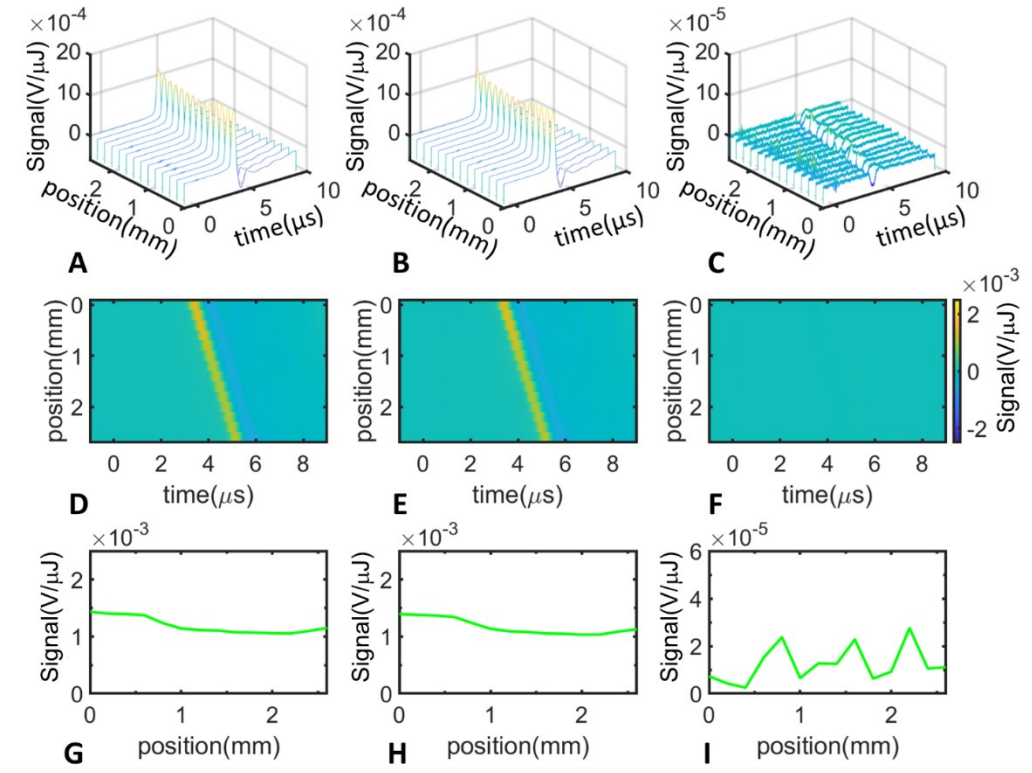

Figure 6.14. Photoacoustic signals were collected for a capillary tube filled with a transformed *E. Coli* (overexpressing GAF3) bacterial suspension immersed in a cuvette filled with a BBBN solution, A(540 nm) = 0.5. Pulsed excitation was at 540 nm, T = 20 °C. The top row (**a-c**) reports waterfall plots of the photoacoustic signals as a function of time and of the position of the excitation beam inside the cuvette for $GAF3_R$ (**a**), $GAF3_G$ (**b**), and the $GAF3_G$ - $GAF3_R$ difference (**c**). The center row (**d-f**) shows the contour plots for the signals in (**a-c**). The bottom row (**g-i**) shows the amplitude of the first positive oscillation of the PA signals in (**a-c**) as a function of the excitation beam position inside the cuvette.

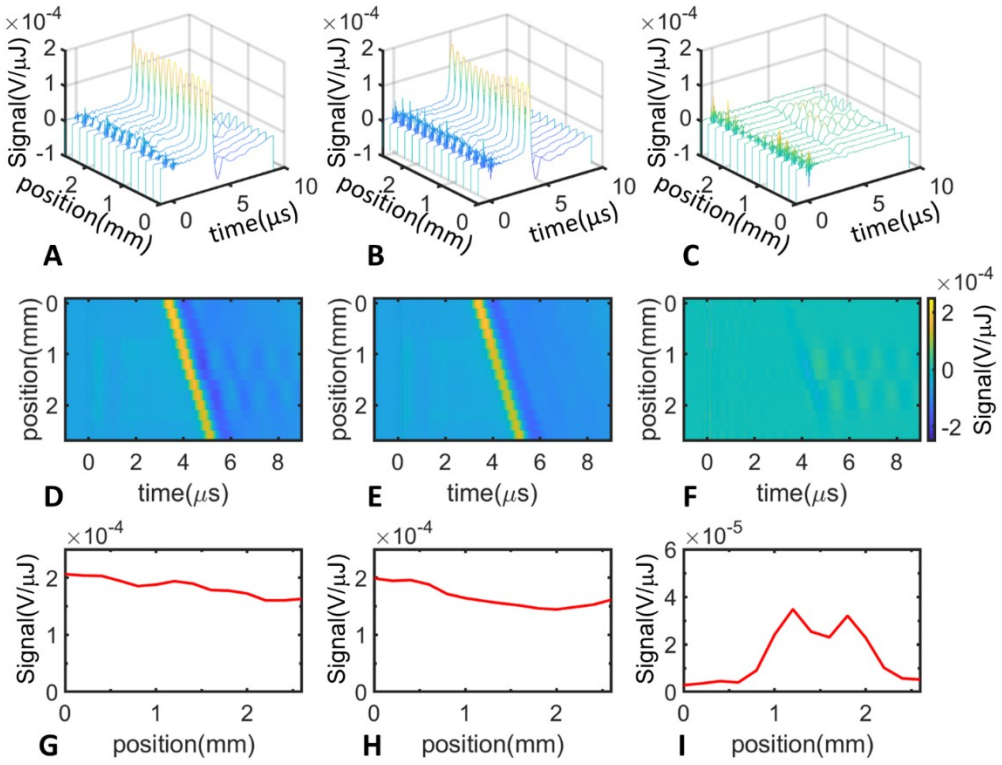

Figure 6.15. Photoacoustic signals were collected for a capillary tube filled with a transformed *E. Coli* (overexpressing GAF3) bacterial suspension immersed in a cuvette filled with a BBBN solution, A(650 nm) = 0.75. Pulsed excitation was at 650 nm, T = 20 °C. The top row (**a-c**) reports waterfall plots of the photoacoustic signals as a function of time and of the position of the excitation beam inside the cuvette for $GAF3_R$ (**a**), $GAF3_G$ (**b**), and the $GAF3_R$ - $GAF3_G$ difference (**c**). The center row (**d-f**) shows the contour plots for the signals in (**a-c**). The bottom row (**g-i**) shows the amplitude of the first positive oscillation of the PA signals in (**a-c**) as a function of the excitation beam position inside the cuvette.

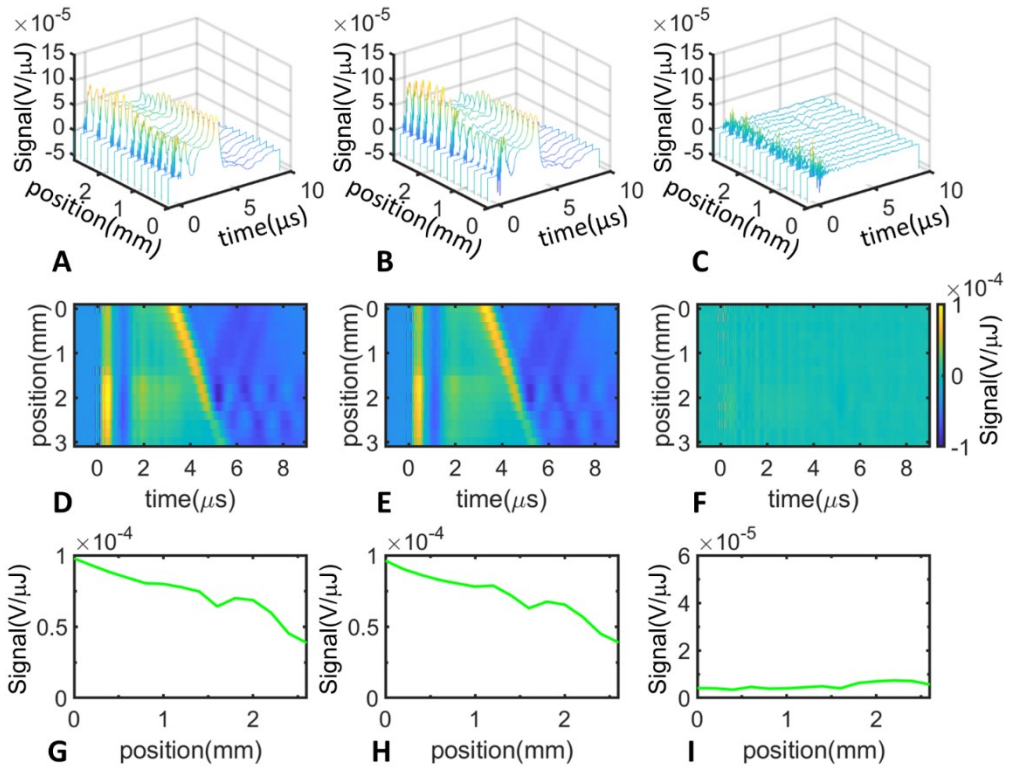

Figure 6.16. Photoacoustic signals were collected for a capillary tube filled with a transformed *E. Coli* (overexpressing GAF3) bacterial suspension immersed in a cuvette filled with an *E. Coli* suspension, A(600 nm) = 0.5. Pulsed excitation was at 540 nm, T = 20 °C. The top row (**a-c**) reports waterfall plots of the photoacoustic signals as a function of time and of the position of the excitation beam inside the cuvette for $GAF3_R$ (**a**), $GAF3_G$ (**b**), and the $GAF3_R$ - $GAF3_G$ difference (**c**). The center row (**d-f**) shows the contour plots for the signals in (**a-c**). The bottom row (**g-i**) shows the amplitude of the first positive oscillation of the PA signals in (**a-c**) as a function of the excitation beam position inside the cuvette.

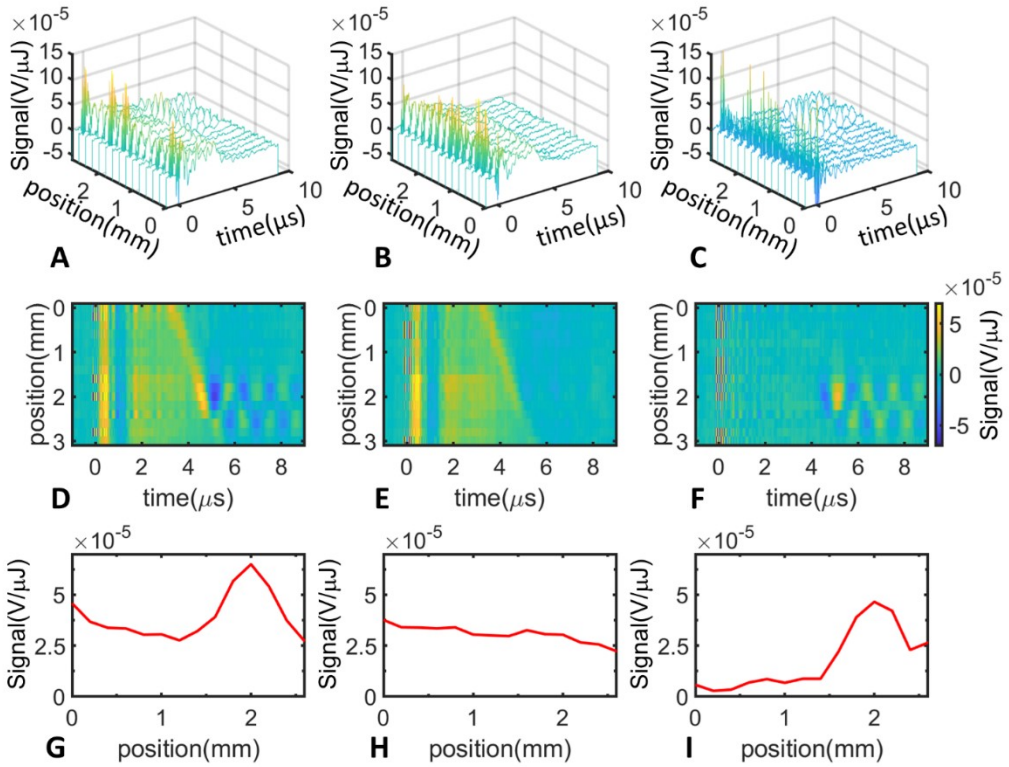

Figure 6.17. Photoacoustic signals were collected for a capillary tube filled with a transformed *E. Coli* (overexpressing GAF3) bacterial suspension immersed in a cuvette filled with an *E. Coli* suspension, A(600 nm) = 0.5. Pulsed excitation was at 650 nm, T = 20 °C. The top row (**a-c**) reports waterfall plots of the photoacoustic signals as a function of time and of the position of the excitation beam inside the cuvette for $GAF3_R$ (**a**), $GAF3_G$ (**b**), and the $GAF3_R$ - $GAF3_G$ difference (**c**). The center row (**d-f**) shows the contour plots for the signals in (**a-c**). The bottom row (**g-i**) shows the amplitude of the first positive oscillation of the PA signals in (**a-c**) as a function of the excitation beam position inside the cuvette.

As a result, we find out that the photochromic PA signal enables identifications of the spatial distribution of the protein (within the cylindrical capillary tube phantom) in the presence of competitive absorbance and scattering media (**Figure 6.10**). When the capillary is immersed in water, the position of the *E. Coli* suspension overexpressing GAF3 is easily detected regardless of the photochromic behavior (**Figure 6.12**, **Figure 6.13**). However, in a competitive absorbing (**Figure 6.14**, **Figure 6.15**) or non-absorbing (**Figure 6.16**, **Figure 6.17**) scattering environment, the capillary position becomes evident only when the non-modulated background is suppressed thanks to the modulable fraction of the PA signal coming from the photochromic change between $GAF3_R$ and $GAF3_G$. The double peak feature at the center of the capillary is due to optical artifacts due to the curvature of the capillary walls.

6.2.3.5 Time-resolved heat release and volume changes

The slightly improved time resolution of the current photoacoustic setup prompted us for a reevaluation of the enthalpic and volumetric changes associated with photoconversion of GAF3. In this paragraph, we briefly describe the experimental procedure followed to analyze the non-radiative decays after photoexcitation of GAF3 (3,146,147) and the analysis results. After baseline subtraction, signals are normalized for sample absorbance at the excitation wavelength ($1\text{-}10^{-A}$) and laser pulse energy. We compare signals for samples ($GAF3_R$ or $GAF3_G$) to an absorbance- and laser energy-normalized Brilliant Black BN (BBBN) signal measured under identical temperature conditions. BBBN is a photocalorimetric reference, i.e., a compound demonstrated to deplete all the excited state energy through thermal relaxation within a few nanoseconds from excitation. Reference and sample signals are normalized to the maximum of the (laser pulse energy and absorbance) normalized reference signal before performing deconvolution analysis (performed using the program Sound Analysis, Quantum Northwest, Spokane, WA, USA). In **paragraph 1.3**, we mentioned that signal is a time convolution between the transfer function of the instrument, obtained with the calorimetric reference and the time derivative of the time-dependent ratio of the signal (**Equation 1.19**). It is possible to use a numerical reconvolution to retrieve the kinetic, enthalpic and volumetric parameters (146–148). These reconvolution methods assume a sum of single-exponential decay functions for the evolution of the ratio $H(t)$ as we can see in (**Equation 1.19**) and **Equation 6.2**. A reconvolution of the waveform of the photocalorimetric reference and either one, or the sum of two exponential decays fits the GAF3 signals, depending on temperature.

$$H(t) = \sum_i \frac{\phi_i}{\tau_i} e^{-\frac{t}{\tau_i}}$$

Equation 6.2

From deconvolution, we retrieved the pre-exponential factors (ϕ_i), and lifetimes (τ_i). Collecting signals for $GAF3_R$ and $GAF3_G$ as a function of the thermoelastic parameter $C_P\rho/\beta$, exploiting the strong temperature dependence of these parameters, it is possible the separation of the enthalpic and volumetric contributions (3). The values of $C_P\rho/\beta$ as a function of temperature for the buffer used in these studies is determined by a comparative method, using its known temperature dependence in water. The pre-exponential factors φ_i are plotted as a function of $C_P\rho/\beta$ using the linear relation coming from reference (3):

$$\phi_i = \alpha_i + \frac{\Delta V_i}{E_\lambda}\frac{C_P \rho}{\beta}$$

Equation 6.3

Where E_λ is the molar energy of incident photons, C_P is the constant pressure-specific heat, and β is the isobaric volume expansion coefficient. For each transient, we estimate the fraction of absorbed energy released as heat (α_i) and the structural volume change (ΔV_i). Molar structural volume changes $\Delta V_{R,i}$ were then calculated from observed volume changes according to the relation: $\Delta V_{R,i} = \Delta V_i / \phi_i$, where ϕ_i is the reaction quantum yield. Further data analysis was performed using OriginLab Pro (OriginLab Corporation, Northampton, MA 01060, USA) and Matlab (The MathWorks, Inc., USA). As already discussed, the setup used in this work provided a slightly higher temporal resolution compared to the one (144) used in previous studies on GAF3 (144) due to the size of the slit, allowing a re-evaluation of the heat release and volume change associated with photoconversion previously reported. In **Figure 6.18**, we report the laser pulse energy and absorbance normalized PA signals for $GAF3_R$ (**a**, **b** red curves) and $GAF3_G$ (**c**, **d** green curves) at 5°C (**a**, **c**) and 20°C (**b**, **d**). The reference signals from BBBN (black curves) are shown for comparison. The signals for $GAF3_R$ and BBBN at 20 °C (**Figure 6.18**, **b**) present a comparable amplitude indicating that the heat release upon photoexcitation is similar. Their time profile is also similar, but the slight shift of the $GAF3_R$ signal suggests the presence of a transient occurring at the limit of the time resolution of the setup. This shift, more evident at 5 °C (**Figure 6.18**, **a**) where the contribution from structural volume changes is more relevant, suggests the presence of a contraction in the tens of nanoseconds range. This second transient was not detected in our previous investigation, due to the lower resolution (≈60 ns) of the setup used in that case, where a 1 mm wide slit was used (144). On the other hand, the signal from $GAF3_G$ at 20 °C (**Figure 6.18**, **d**) is lower in amplitude than the signal of the reference compound, indicating a transient of negative amplitude with a lifetime in the tens of nanoseconds follows a fast, sub-resolution positive signal. The negative signal becomes evident at 5 °C (**Figure 6.18**, **c**). We note that at t = 0 s, the absorption of light coming from fluorescence emission by $GAF3_G$ or $GAF3_R$, excited by the laser pulse or by scattered light, and absorbed by the surface of the transducer, produces an intense oscillation. The latter contribution is evident also in the signals collected for the reference compound. We then performed the deconvolution analysis of signals for $GAF3_G$ and $GAF3_R$, retrieving the fractional amplitudes of the transients at each temperature. We obtained the best fit of the transients with a single exponential decay, with a lifetime below the time resolution (≈20 ns) at the higher temperatures or with the sum of two exponential decays for temperatures below 15 °C. Representative fits are reported in **Figure 6.19** and **Figure**

6.19. The lower temperature range allows us to determine the second, slower transient lifetime that occurs in the 20-100 ns time range. The short lifetime of the resolvable phase, occurring at the limit of the time resolution of the setup, affects the estimate of the fractional amplitudes. Under these conditions, amplitudes and lifetimes show correlation and cannot always be retrieved reliably. Thus, low-temperature data, where the lifetime of the second transient becomes longer, usually afforded more reliable parameters.

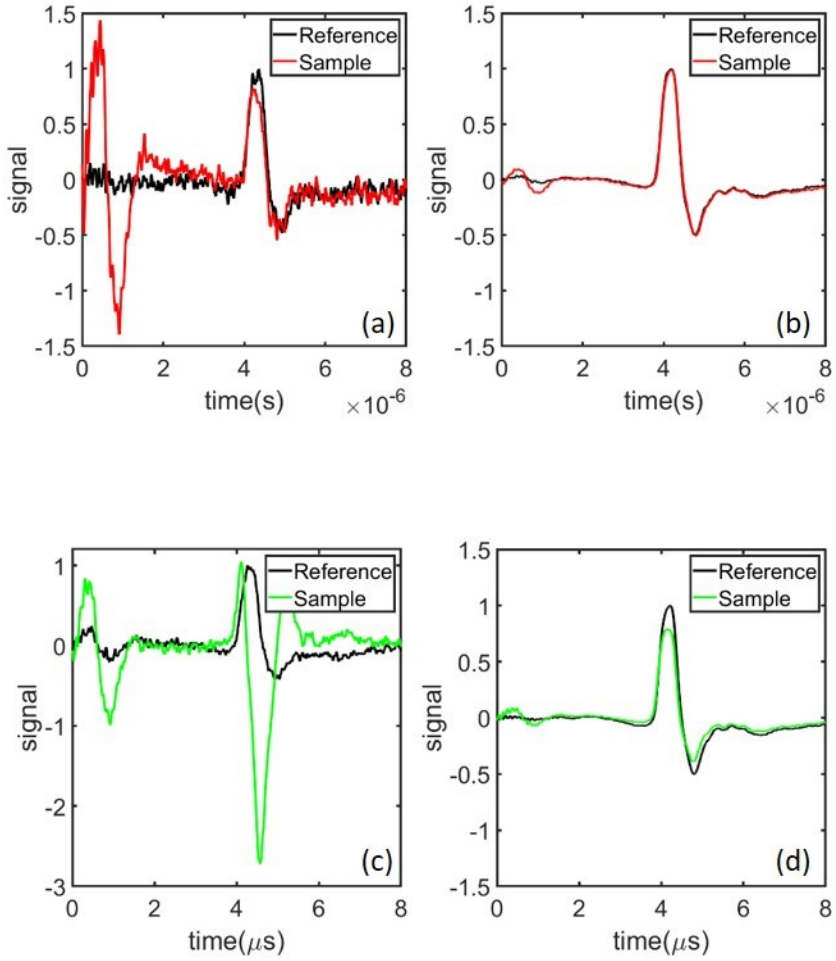

Figure 6.18. PA signals for $GAF3_R$ (**a**) and $GAF3_G$ at 5° C (**c**) and 20 °C ($GAF3_R$: **b**, $GAF3_G$: **d**). The top panels report a comparison between the laser pulse energy- and absorbance-normalized signals from BBBN (black) and $GAF3_R$ (red) at 5 °C (**a**) and 20 °C (**b**). The excitation wavelength was 650 nm. The bottom panels report a comparison between the laser pulse energy- and an absorbance-normalized signal from BBBN (black) and $GAF3_G$ (green) at 5°C (**c**) and 20 °C (**d**). The excitation wavelength was 540 nm.

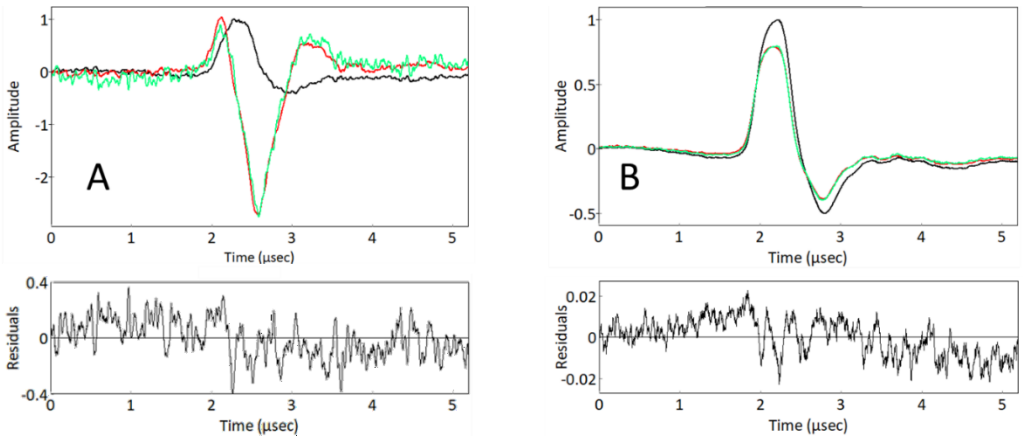

Figure 6.19. Representative deconvolution analysis of photoacoustic signals for GAF3 $_G$ at T = 7°C (**a**) and T = 20 °C (**b**). Black solid curves are the IRF measured with a BBBN solution. Red solid curves are the signals from GAF3$_G$. State GAF3$_G$ was selected by CW illumination with the 514 nm output of an Ar ion laser. The solution was stirred to ensure homogeneity. The solid green lines are the reconvolution of the IRF signals with a biexponential decay.

The fraction amplitudes of the exponential decay provide the thermodynamic information. In **Figure 6.20** (**a**), we plot the energy content of each transient ($\phi_i E_i$) as a function of $C_P\rho/\beta$. We calculate the fraction of absorbed energy released as heat (α_i) and the molar structural volume change ($\Delta V_{R,i}$) from the intercepts and slopes retrieved by the linear fits (**Table 6.2**). In agreement with our previous determination, for both species, an expansion accompanies the fast E-Z photoisomerization (labeled as process 1 in the kinetic analysis, with a lifetime below ≈10 ns). The reaction volume is larger for the GAF3$_G$ to GAF3$_R$ conversion. The α_1 values agree with our previous determinations (0.76±0.02 for GAF3$_R$ to GAF3$_G$ 0.71±0.03 for GAF3$_G$ to GAF3$_R$)(144), aside from a small difference possibly due to the better resolution of the present work. Thus, the energy content of the first reaction intermediate is comparable to our previous estimate. The relatively large contraction associated with the second transient (for the GAF3$_G$ to GAF3$_R$ conversion), labeled as 2 in the kinetic analysis, is consistent with our previous findings. However, thanks to the improved time resolution, we detect a smaller amplitude volume change, with a lifetime in the 10-100 ns range, also for the GAF3$_R$ to GAF3$_G$ photoconversion. Interestingly, the slower processes' heat release (enthalpic change) is zero within the experimental error. Last, in **Figure 6.20** (**b**), we calculate the activation energy as a slope of an Arrhenius plot $lnk_2 = E_a/RT + lnk_0$. Here we consider $k_2 = \tau_2^{-1}$ and we plot it against the inverse of the temperature $1000/T(K)$.

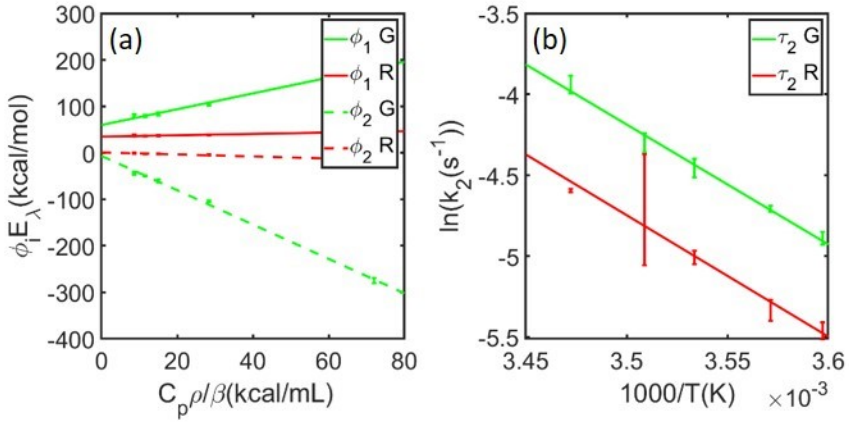

Figure 6.20. (**a**) A plot of the energy content of each transient ($\phi_i E_\lambda$) as a function of $C_P\rho/\beta$ for GAF3$_R$ (red) and GAF3$_G$ (green). Solid lines, $\phi_1 E_\lambda$, dashed lines, $\varphi_2 E_\lambda$. (**b**) Arrhenius plot for $k_2 = {\tau_2}^{-1}$ for GAF3$_R$ (red) and GAF3$_G$ (green). We retrieved lifetimes τ_2 only at temperatures below 15°C.

Table 6.2. Fractions of absorbed energy are released as heat and molar structural volume change. The linear Arrhenius plot determined activation energies for the slow process 2.

	α_1	$\Delta V_{R,1}$ (mL/mol)	α_2	$\Delta V_{R,2}$ (mL/mol)	ln(A)	E_a (kcal/mol)
GAF3$_R$	0.79±0.01	1.9±0.1	0.01±0.01	-2.6±0.3	40.5±0.5	13.9±0.3
GAF3$_G$	0.64±0.05	8±1	0.15±0.08	-11.7±0.8	42±1	14.6±0.6

6.3 Conclusions

In this first part of the experimental results, we engineered and produced two GFP mutants intending to obtain photochromic, non-fluorescent variants. However, from the first analysis of optical spectroscopy data, we find out that GFP mutants have non-ideal optical properties (photoconversion quantum yield and contrast). In particular, darkwQ showed very little switching. The mutant darkwQT was investigated in PA generation resulting in a tunable signal with poor contrast. The protein GAF3 from slr1393, on the other hand, shows better spectral properties with higher photoconversion quantum yields and contrast compared to the two GFPs. The PA signal generated by photoexcitation of GAF3 resulted tunable by selecting the red or the green absorbing state through irradiation with green or red light. We have shown that this photochromic signal can be easily distinguished from competing, non-photochromic absorbers, thus enhancing the contrast and rejecting the background signals. GAF3 was then selected as the probe to focus our photoacoustic studies.

We then used a capillary tube filled with a GAF3-containing solution as a phantom, demonstrating the possible identification of the tube's position through 1-D scanning of

the laser beam across the medium into which the capillary is placed. The photochromic behavior allows contrast enhancement and background signal suppression. In the case of absorbing media and non-absorbing, scattering media, we achieved it without loss of spatial resolution. Interestingly, the results obtained with photochromic PA signals recorded after red excitation were stronger than those originating from the green absorbing form.

GAF3, unlike canonical bacterial phytochrome photoreceptors requesting an arrangement of three domains (PAS-GAF-PHY), or full preservation of their kinetic and spectroscopic properties, binds PCB even as isolated proteins, providing all phytochrome-typical features of absorption and kinetics (149–151). Even if PCB is not present in all cells, in vivo binding of the chromophore to GAF3 can be obtained using a two-plasmid approach in *E. Coli* (142,152), bypassing external chromophore supplementation.

The red-green photochromism of GAF3 provides an additional signal that may be useful in multispectral photochromic PA imaging, even if not in the ideal spectral transmission region. It should be noted here for future applications that cyanobacteriochromes had been reported that bind BV (with a similar extent of photochromism between the parental and the photoproduct form) and that also PCB-binding CBCR GAF domains had been manipulated by mutagenesis to bind BV, shifting the spectral range for excitation further into the long wavelengths range of the spectrum.

As further advantages, photoswitching, bilin-binding proteins exhibit large absorption coefficients. The CBCR GAF domains show quite high photoconversion yields, warranting very fast photoswitching of the protein between the two states, which may be exploited to speed up the acquisition process in multi-wavelength imaging. From a structural perspective, CBCR shows a smaller dimension compared to bacterial phytochromes and GFPs derivatives. Finally, the modest but appreciable fluorescence yield may be exploited in correlative microscopy.

Further developments to test these photochromic proteins in PA imaging setups and extension of the two-plasmid approach to eukaryotic cells will assess the whole potential of this photochromic probe for biological applications.

7 Two-Photon Photoacoustic Microscopy (2P-PAM)

As we mentioned in **paragraphs 1.2.1** and **4.2.3.2**, 2PA provides unique features in terms of penetration depth, excitation constraints, and resolution while applied to fluorescence microscopy and PAM. Pursuing our aim to develop a system to enhance the contrast of PAM, we describe a 2P-PAM setup made for measurements with photochromic systems. With this setup, we try to combine the advantages of 2PA and PAM with the future perspective of including photochromic probes.

7.1 Optical Setup

The optical setup is obtained by modifying a previously reported one (153) and is reported in **Figure 7.1**. The excitation is provided by a Ti:Sapphire laser (Coherent, Chameleon Ultra). The laser generates mode-locked ultrashort pulses with a duration of 140 fs; the pulse repetition rate is 80 MHz and is given by the oscillator's round-trip optical path. Ti:sapphire oscillators are normally pumped with a continuous-wave laser beam from an argon or frequency-doubled Nd:YVO4 laser. The output is modulated by OPO for the wavelength and by a custom-made Electro-Optic Modulator (EOM) for the frequency. The EOM modulates the laser's frequency with a square wave of 1.17 MHz and a duty cycle of 50%. The next paragraph will threaten the properties of EOM.

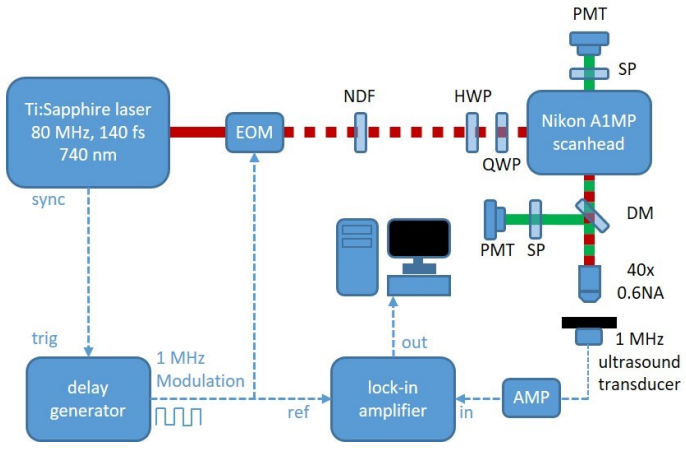

Figure 7.1. Schematic representation of the 2P-PAM setup. EOM is the Electro-Optic Modulator, PMT is the photon multiplier tube used as a detector, HWP and QWP are half and quarter waveplates, SP is short pass filters for fluorescence selecting, DM is a dichroic mirror, and AMP is the amplifier sequence. The solid red line is the NIR excitation, dashed red line is the NIR excitation after EOM modulation. Fluorescence is reported in a solid green line. The laser's position, the lock-in amplifier, the transducer and the delay generator driving the delay generator are reported.

A modulation of 80 MHz has a time between pulses (12.5 ns) that is much shorter than the time required by the acoustic wave to travel to the transducer making the detected

signal a pulse train of acoustic waves (105), while in conventional pulsed photoacoustic working between a few Hz and 10 kHz, single wave analysis is possible (**paragraph 6.2**). The subsequent modulation provided by the EOM will make the system behave like a CW laser with an amplitude modulation frequency of 1.17 MHz (**paragraph 4.3.1**). The laser beam then crosses a neutral density filter, and half and quarter waveplates are fed into a Nikon A1MP Scanhead. The ultrasound transducer (Olympus, V103-RM Contact Transducer) with a central frequency of 1.17 MHz leans against the cover glass, which covers the sample, on the opposite side of the objective lens (Nikon, 40x 0.6 NA) and is coupled to it with water. The signal is then amplified by a Thorlabs Transimpedance amplifier (AMP140 10kV/A Gain 10 MHz Bandwidth) and an Olympus Ultrasonic Pre-Amp (30dB Gain 50KHz-25MHz Bandwidth) and fed to a lock-in amplifier (SR830, Stanford Research) providing the results. The process behind lock-in detection will be treated in detail in **paragraph 7.1.2**.

7.1.1 Pump Modulation

An electro-optic modulator (EOM) is an optical device exhibiting an electro-optic effect. This object may also be referred to as Pockels cell. The simplest kind of EOM is made by a crystal (such as lithium niobate) attached to a voltage generator (half-wave voltage required to induce a π phase change, V_π) in the order of hundreds/thousands of volts. The high voltage generates changes in the refractive index distorting the molecules' position, orientation, or shape; a nonlinear optical material with an incident static or low-frequency optical field will see modulation of its refractive index. That means that if the crystal is exposed to an electric field, the light will travel more slowly through it, with the phase of the light leaving the crystal being directly proportional to the length of time it takes to pass through: the phase of the laser light exiting an EOM can be controlled by changing the electric field in the crystal.

In a Phase Modulation pattern, the phase of a carrier signal is modulated to follow the changing voltage level (amplitude) of the modulation signal with its peak amplitude and frequency remaining constant. If the amplitude of the information signal changes, the carrier phase changes correspondingly. It is generally used for creating sidebands in a monochromatic laser beam.

This setup uses a Pockels cell as an amplitude modulator of the 80 MHz output of the laser. We consider the beam to have an incoming 45° degrees polarization and the crystal with no birefringence without an applied electric field. Behind the crystal, there is a polarizer aligned to obtain 100 % transmission without an applied voltage. We can consider the transmitted field as a superposition of two in-phase field components of equal strength. Those components acquire a phase difference of $\Delta\phi = \pi V / V_\pi$ after the

application of an electric field. The total transmitted amplitude is then proportional to $(1 + e^{i\Delta\phi})/2$ and we obtain the following result for the power transmission:

$$T(V) = \left|(1 + e^{i\Delta\phi})/2\right|^2 = cos^2 \frac{\pi V}{V_\pi}$$

Equation 7.1

Typically, the voltage varies between zero and half-wave voltage.

7.1.2 Acquisition System

The detected PA signal needs to be amplified and "cleaned" from interferences. 2P-PAM setup generally implements a lock-in detection extracting small signals from a noisy background. Lock-in amplifiers (LIA) are homodyne detection schemes combined with a low-pass filter to extract signals in a specific frequency band by retrieving relative phase and amplitude relative to a periodic reference signal. LIA uses the knowledge of signals' time dependence to extract it from the noisy background as it happens for radios. LIA multiplicates its input waveform with a reference signal (down-mixing or heterodyne/homodyne detection) and then applies an adjustable low-pass filter to the result (demodulation or phase-sensitive detection). LIA can generate itself a reference signal, or it can take one from the outside. In our experimental setup, the reference signal is provided directly as the output of the delay generator used to drive the EOM and synchronized with the laser repetition pulse

The system is stimulated by a sinusoidal signal and the system response V_s and the reference signal V_r is fed to the LIA to determine the relative amplitude R and phase θ through dual-phase demodulation. The input signal is split and multiplied with the reference signal and a 90° phase-shifted copy of it. The outputs of the mixers pass through configurable low-pass filters, providing the two outputs, X and Y, termed the in-phase and quadrature component. The amplitude R and the phase Θ are derived from X and Y by a transformation from Cartesian coordinates into polar coordinates using the relation expressed by **Equation 7.2** and **Equation 7.3**:

$$R = \sqrt{X^2 + Y^2}$$

Equation 7.2

$$\theta = atan2(Y, X)$$

Equation 7.3

In terms of complex numbers, we can consider the signal $V_S(t)$ as the sum of two rotating vectors (154):

$$V_s(t) = \sqrt{2}Rcos(\omega_s t + \theta) = \frac{R}{\sqrt{2}} e^{+i(\omega_s t+\theta)} + \frac{R}{\sqrt{2}} e^{-i(\omega_s t+\theta)}$$

Equation 7.4

One vector rotates clockwise, the other one counterclockwise, both at the same speed ω_S. The projection onto the x-axis of the two vectors is the $V_S(t)$ while the one on y-axis is always zero. We express the dual-phase modulation through the multiplication of the input signal with the complex reference signal:

$$V_r(t) = \sqrt{2}e^{-i\omega_r t} = \sqrt{2}\cos(\omega_r t) - i\sqrt{2}\sin(\omega_r t)$$

Equation 7.5

The complex signal after mixing is then:

$$Z(t) = V_s(t) \cdot V_r(t) = R[e^{+i[(\omega_s t-\omega_r t)+\theta]} + e^{-i[(\omega_s t+\omega_r t)+\theta]}]$$

Equation 7.6

In practice, this situation is like having two arrows appearing to rotate at different angular velocities $\omega_s - \omega_r$ and $\omega_s + \omega_r$. The second arrow rotates much faster if the signal and reference frequencies are close. The subsequent filtering is mathematically expressed as averaging the moving vectors over time. Filtering removes the fast-rotating term by setting $\langle e^{-i[(\omega_s t+\omega_r t)+\theta]} \rangle = 0$. The averaged signal is then:

$$Z(t) = Re^{i[(\omega_s t-\omega_r t)+\theta]} \underset{\omega_s=\omega_t}{\Longrightarrow} Re^{i\theta}$$

Equation 7.7

Equation 7.7 reports the demodulated signal in which real and imaginary parts, obtained through Euler's formula, are the in-phase and quadrature components. In the graphical view, the condition $\omega_s + \omega_r$ means that the slow-rotating arrow appears at rest while the other arrow rotates clockwise at twice the frequency (often called the 2ω component). The lowpass filter usually cancels out the 2ω component completely

7.2 Setup Alignment and Calibration

The setup properties were investigated through metallic grids (Thorlabs R1L3S3PR and R1L3S5P). They were used to determine the optimal contact medium and the optimal position of the transducer over the sample.

7.2.1 Grid Samples

In **Figure 7.2**, we observe an alignment grid. Panel (**a**) shows the retrieved amplitude from LIA; panel (**b**) shows the retrieved phase. Panel (**c**) shows the transmitted light, and panel (**d**) the merged image.

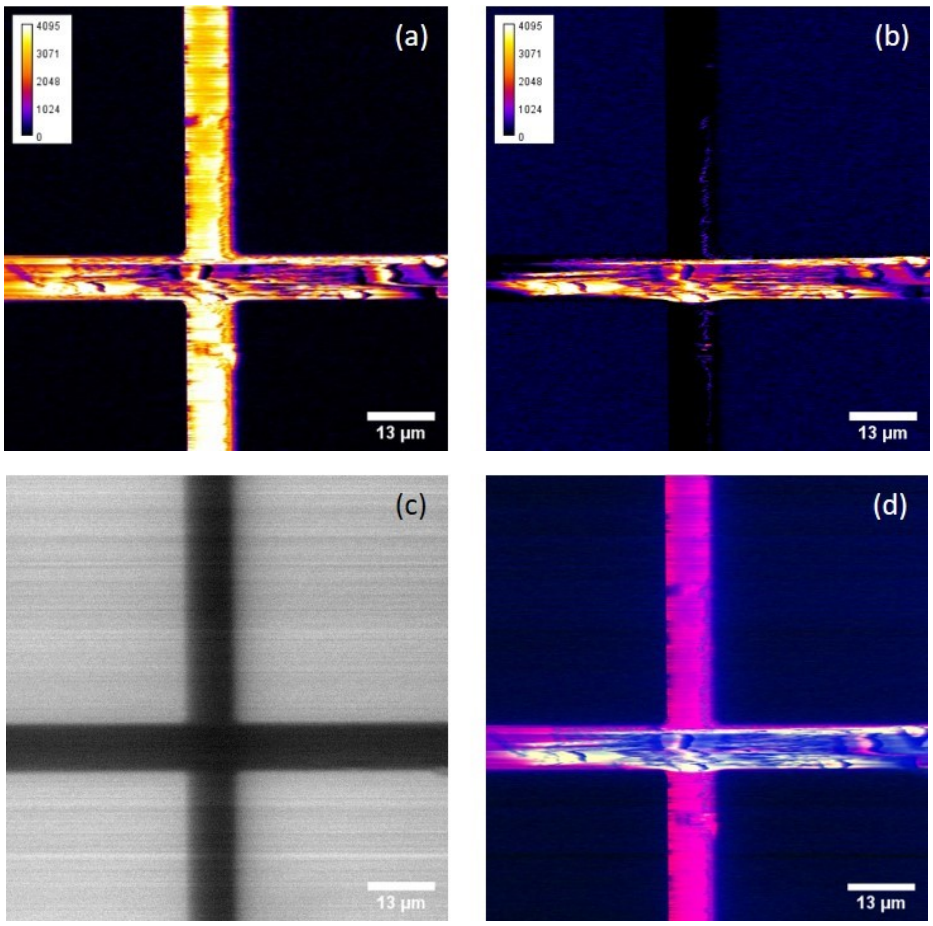

Figure 7.2. Photoacoustic images and transmitted light images of a metal alignment grid. (**a**) The amplitude of the PA signal. (**b**) The phase of the PA signal. (**c**) Transmitted light. (**d**) Merged image.

The first thing that might be observed is the different behavior of phase and amplitude. The two different branches of the grid are probably on different layers. This may somehow induce a difference in phase between the outcoming waves.

A resolution grid is used as a sample in the following images (**Figure 7.3**, **a-f**). From the profile below, we can observe a slope change at the border in phase (**b**, **e**); this behavior is similar to a derivative. The acquisition wavelength used was 780 nm.

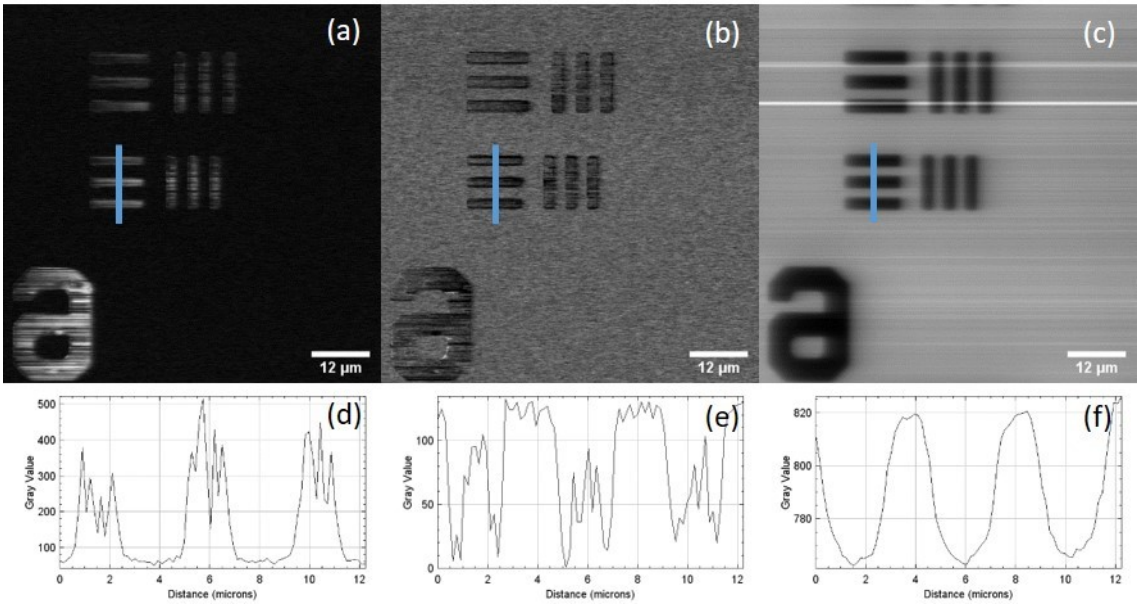

Figure 7.3. Photoacoustic and transmitted light images of a resolution grid. (**a**) The amplitude of the PA signal. (**b**) The phase of the PA signal. (**c**) Transmitted light. Bottom row (**d-f**), values along the blue line.

Al the images acquired using the custom setup images are edited through Fiji imaging processing package (38).

7.3 Results

This last paragraph presents results obtained in a biological specimen with the above-described setup.

7.3.1 Histological Stain

We used a cerebellum slab stained with Hematoxylin and Eosin (H&E), exciting at a wavelength of 780 nm. In **Figure 7.4,** we report an image of the region obtained with canonical 2PA microscopy. This image highlights the structure of Purkinje Neuron, a class of GABAergic inhibitory neurons located in the cerebellum (155). Purkinje Neurons are some of the biggest neurons, and they display an elaborate ad intricate dendritic arbor characterized by many dendritic spines (156). The H&E is one of the main stains used in histology. The hematoxylin stains cells' nuclei, and eosin stains extracellular matrix and their emissions are purplish-blue and pink, respectively. An absorption spectrum of the two components is reported in (**Figure 7.5**) from reference (157). From literature (158), it is possible to retrieve the 2PA spectra of hematoxylin and eosin. **Figure 7.5** compares the 1PA e 2PA spectra of both components. Both stains may show a 2P absorption band centered around 800 nm. We expect 1PA and 2PA spectra to show the same bands for molecules lacking an inversion center, although possibly with different relative intensities (49). In eosin's case, the 2PA peak at 830 nm is thus matched to the 1PA secondary peak

at 415 nm (**Figure 7.5**, *left*). On the other hand, the wavelengths of the two 2PA peaks of hematoxylin at 810 nm and 840 nm appear to be blue-shifted compared to twice the wavelengths of the 1PA peaks at 425 and 450 nm (**Figure 7.5**, *right*). Reference (159) reports this feature for several dyes.

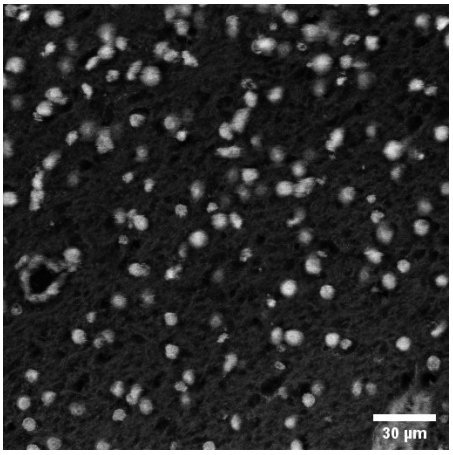

Figure 7.4. 2P image of a slice of cerebellum showing Purkinje Neuron stained with H&E stain. The image is obtained through the latter setup, exciting with a wavelength of 780 nm.

As a first attempt, we looked at a cropped region of the sample (**Figure 7.6**, **a-e**). The measure should be taken with a high pixel dwell time and high averaging of the sample. In this case, some features of the cells are shown. It is interesting to notice that signals revealed for PA (both phase and amplitude) are different from each other and are different from those of the fluorescence. However, these images are strongly affected by noise.

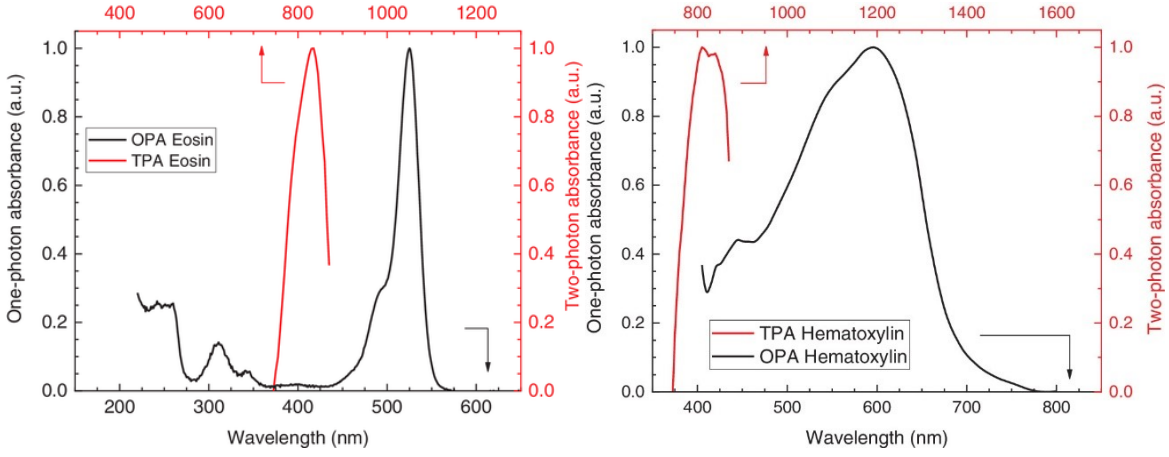

Figure 7.5. *Left*. Comparison between the one-photon-absorption spectrum (black) from the literature (157) and the measured two-photon-absorption spectrum (red) for eosin at 14.45 µM (1% concentration). *Right*. Comparison between the one-photon-absorption spectrum (black)

from the literature (157) and the measured two-photon-absorption spectrum (red) for hematoxylin at 0.83 µM (0.25% concentration). Images from reference (158).

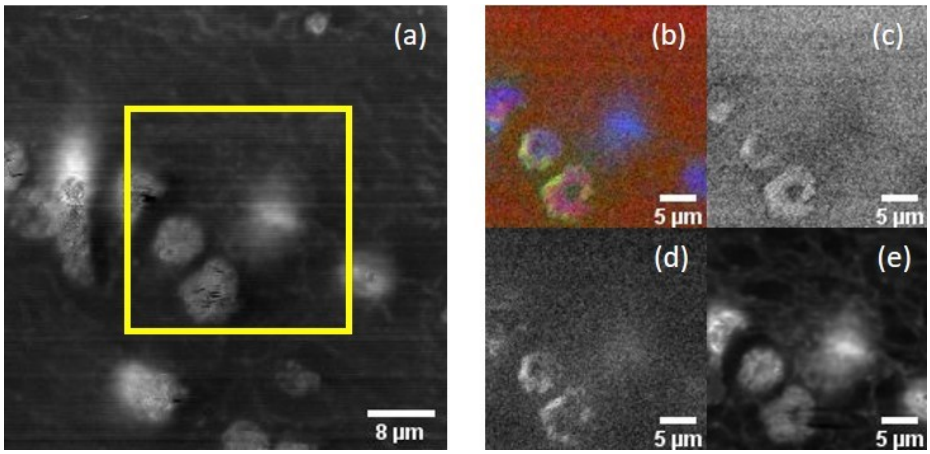

Figure 7.6. Images of a section of cerebellum showing Purkinje Neuron stained with H&E stain. (**a**) 2PA image of a region of the cerebellum. The yellow box indicates cropped area. (**b**) Merged image of the cropped area. (**c**) The phase of the PA signal of the cropped region. (**d**) The amplitude of the PA image of the cropped area. (**e**) 2P fluorescence of cropped region.

If we crop again on one of these cells, working then with a higher pixel size, we see a more detailed image showing a strongly different PA and fluorescence behavior (**Figure 7.7**). The cell results are hollow in terms of photoacoustic (**b-c**) compared to fluorescence (**d**). They also show different structures over the cellular membrane.

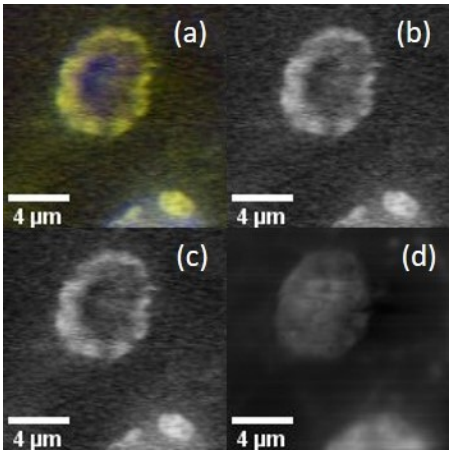

Figure 7.7. Image of a Purkinje Neuron. (**a**) Merged image. (**b**) The amplitude of the PA image of the cropped area. (**c**) The phase of the PA signal of the cropped region. (**d**) 2P fluorescence of cropped region.

Al the images acquired using the custom setup images are edited through Fiji imaging processing package (38).

7.4 Conclusions

In general, from the study on histological samples, as a proof of concept, we can conclude that fluorescence and PA may show different behaviors that can provide complementary information. Combining the literature data on H&E reveals that 2PA has a higher probability of occurring than 1PA at that frequency range. Thus, we can assume that the PA emission occurs after 2PA. As we saw from the results, the contrast of the images of biological samples is poor, and the noise dominates. For metallic samples, we can assume the presence of a resonant effect that enhances the signal, but for biological systems, this is not achievable. The modulated excitation, which certainly provides faster acquisition times, also constrains the contrast (**paragraph 4.3.1**) for its poor intrinsic sensitivity. In **Chapter 6**, we demonstrate in a simple 1D experiment the feasibility of the application of rsFPs in PAM to enhance contrast. The possibility of a 2P photoconversion of rsFPs designed for visible application was demonstrated (160). As a next step, we will implement a photoconversion experiment to demonstrate the feasibility of using GAF3 as a probe in 2P-PAM to increase contrast. Improving the contrast is not the only way to improve an image: also, the SNR has a crucial role. In the next chapter, we present an approach initially designed for fluorescent microscopy that might be an improvement for SNR in both PA spectroscopy and microscopy.

8 Multi-plane Encoded Light-Sheet Microscopy (MELM)

In **Chapter 6** (and **Chapter 5**), we presented an approach to enhance contrast in PAM that takes advantage of the intrinsic characteristic of the probes; the application of rsFPs in PAM boosts the poor contrast proper of this technique. We postulated then in **Chapter 7** the usefulness of rsFPs to 2P-PAM that may allow combining this strong contrast enhancement with the high resolution, spatial confinement and penetration depth typical of a Two-Photon excitation. This last chapter presents an approach for SNR enhancement independent of the probes' characteristics and based on a light encoding. This approach is implemented in fluorescence microscopy, but we will see that it is of general use, and it can be applied to almost every technique operating under conditions reported in **paragraph 3.2.1**: the noise must be independent of the measurement. As we already mentioned, among the existing techniques, LSFM or SPIM has become the tool of choice for volumetric imaging of large samples (161), thanks to a unique combination of speed, resolution, and FoV. In LSFM, the sample is illuminated with a light sheet (162). Combining a widefield acquisition scheme with shaped illumination allows fast optical sectioning over a large FoV at diffraction-limited resolution using low light doses. Unfortunately, traditional architectures are not optimized for fast 3D imaging: volumetric imaging in LSFM is typically performed by acquiring a sequence of 2D images from different focal planes of the sample (z-stack). Collection of a z-stack is obtained either by sample translation or synchronized movement of light sheet and objective lens, preserving the light-sheet and the focal plane of the detection lens alignment (avoiding blurring or image artifacts); requesting in both cases, a mechanical movement constraining thus the maximum acquisition rate **Figure 8.1** (**a-b**). Various innovative LSFM architectures have been proposed to overcome this limitation: remote focusing detection enables axial scanning at high rates without introducing significant aberrations (163,164).

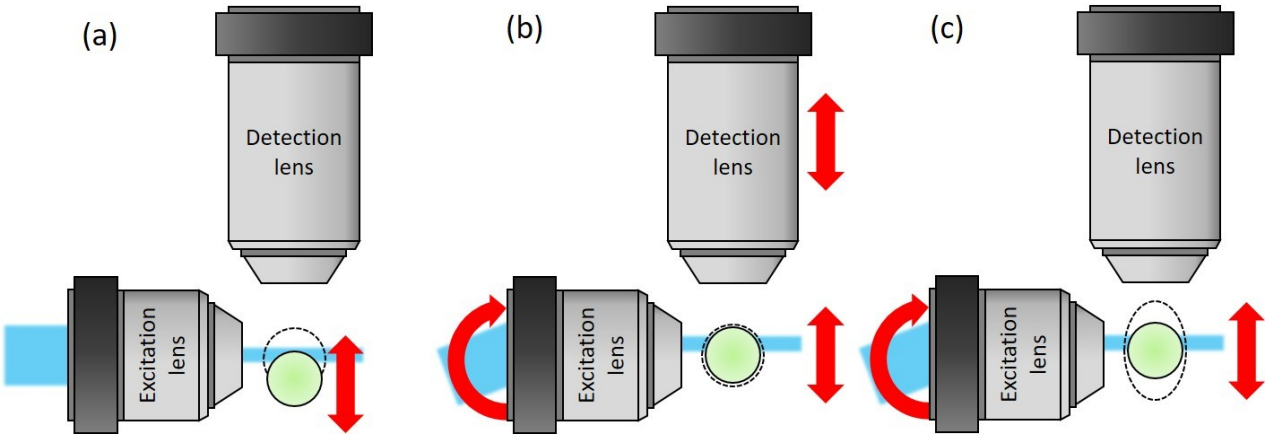

Figure 8.1. Schematic representation of three possible ways of performing 3D measurements in SPIM. The cyan squares indicate the CW 488 nm laser, the green circle represents the sample,

the dashed circle represents the focal spot, and the red arrows represent the moving parts. (**a**) the sample is mechanically scanned through the light sheet that provides optical section and 3D scanning. (**b**) the light sheet is moved by changing the entrance angle while the sample is fixed. To preserve optical alignment also, the detection objective should move. (**c**) the focal spot, the dashed ellipse, is elongated. In this case, the sample is fixed in position while the light sheet is scanned. For the elongation of the focal volume, no moving of the detection objective is needed.

The combination of a thick light sheet and a light field camera exploiting an array of micro-lenses to distinguish the axial origin of the light retrieves information of a whole volume from a single frame (165,166), requesting, however, a computationally demanding reconstruction. The resulting images typically have degraded lateral resolution. Alternatively, it is possible to extend the Depth-of-Field (DoF) of the detection objective (**Figure 8.1**, **c**), having the sample planes appear in focus. Then the translation of the light sheet is enough for image acquisition, with no need for mechanical synchronization. The translation of the light sheet can be performed in a few milliseconds, significantly increasing imaging speed. Several techniques exist for generating an Extended Depth-of-Field (EDoF), spacing from the use of spherical aberrations (167) to wavefront coding (168,169), and finally, varifocal lenses (170–172). However, all EDoF techniques produce a significant loss of photons per plane (**Figure 8.2**), degrading the SNR for the resulting z-stack. As we mentioned, increasing the exposure time of the images to maximize the signal sacrifices acquisition speed. An alternative approach is parallelizing the illumination to increase the information captured per frame and, consequently, the SNR. Although common practice in laser scanning microscopy and stimulated Raman scattering microscopy and spectroscopy (173), such a multiplexing strategy seems challenging in SPIM (174).

Here, we propose a novel technique for suppressing background and noise in EDoF Light-Sheet microscopes. We named this approach, based on illuminating a sample with encoded sequences of multiple simultaneous light sheets, Multi-plane Encoded Light-sheet Microscopy (MELM). In this chapter, we will explain the more technical details of this approach, we will comment on the results obtained, and, finally, we will present a possible application to photoacoustic microscopy and spectroscopy.

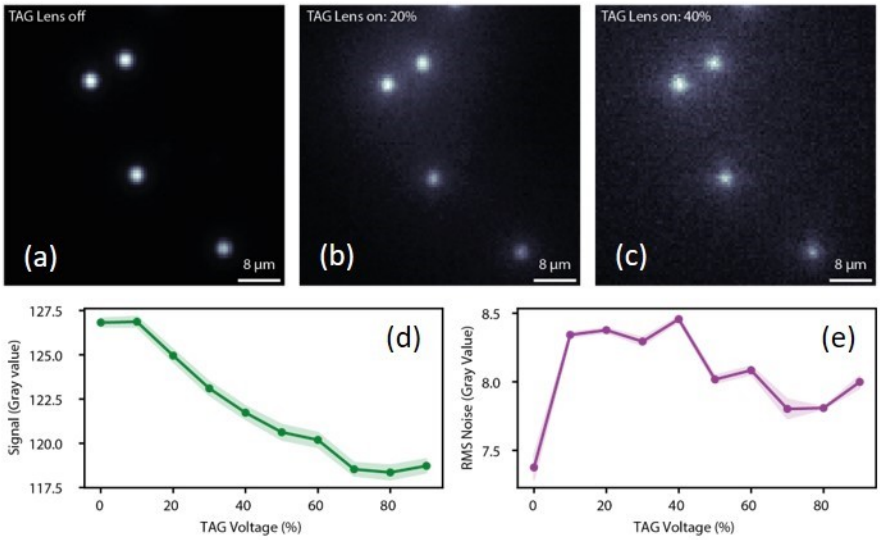

Figure 8.2. Images of 1 µm beads fluorescent beads were acquired with a 10x/0.3 NA objective lens. From (**a**) to (**c**), the driving voltage of the TAG lens increases with a corresponding deterioration of the SNR of the images. We report a quantitative analysis of the signal degradation (**d**) and noise increase (**e**) in terms of RMS. The error bar is shown as a shaded area when bigger than the line width. Image reproduced from reference (67).

8.1 Optical Setup

We report the theory behind this approach in **paragraph 3.2.1**, and in this part, we will describe the technical feasibility. **Figure 8.3** (**a**) reports the coding process for multiple planes. We collect the sum of the corresponding images in a single camera frame; by acquiring different frames (as many as the section of the sample we are interested in), we decode images from each individual using a computationally inexpensive single-step reconstruction algorithm; the decoded images exhibit an enhanced SNR depending on the illumination sequence used. A CW laser at 488 nm (Coherent Sapphire), expanded with a 5× afocal telescope, is then directed towards two Acousto-Optic Deflectors (AODs, IntraAction, ATD- 7010CD2) at the Bragg angle (in the next paragraph, we report a better description of the working principle of AOD) conjugated via a 4f system. The doubly diffracted beam is then directed to the scanning lens (f = 200 mm), while the other secondary beams are filtered out. The beam is then aligned towards the tube lens (f = 200 mm) and the excitation objective lens (Nikon 10×/NA 0.3), reaching the sample inside a chamber (a cube with transparent windows) filled with pure water, sealed to the water dipping detection objective (either Leica 10×/NA 0.3 or Leica 40×/NA 0.8), orthogonal to the excitation line. A 4f system conjugates then the back focal plane of the detection objective to the Tunable Acoustic Gradient (TAG) lens (TAG Optics Inc.), driven at its first resonant frequency (≈70 kHz), while the voltage amplitude determines the extension of the DoF and the properties of the objective lens. The working principle of the TAG lens is

explained in **paragraph 8.1.3**. After the TAG Lens, the fluorescence light is directed towards the tube lens (f = 200 mm), which creates an image of the Illuminated planes on the sensor of an sCMOS camera (ANDOR Neo 5.5). A Notch Filter (NF488-15, Thorlabs) then rejects excitation light (**Figure 8.4**, **a**)

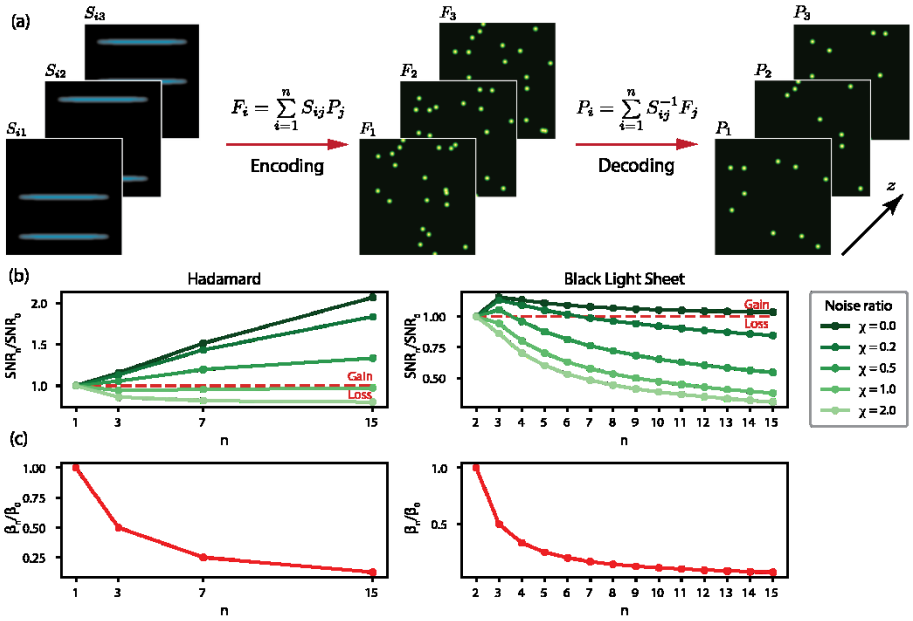

Figure 8.3. (**a**) Working principle of Multiplane Encoded Light-sheet Microscopy. A set S_{ij} of parallel light-sheets simultaneously is shined on the sample, illuminating illuminates at the same time multiple planes P_j whose resulting in superposed images are collected as the frame F_i. In order to retrieve the individual images, it is simply needed to calculate the inverse of the encoding sequence ${S_{ij}}^{-1}$ is calculated. (**b**) Comparison of SNR as a function of the acquired frames for the decoded images acquired with the Hadamard encoding (*left*) and Black Light Sheet encoding (*right*). (**c**) Comparison of the background as functions of the number of acquired frames for the decoded images acquired with the Hadamard encoding (*left*) and Black Light Sheet encoding (*right*). All plots are normalized by the SNR or background level of a sequential scan. Image reproduced from reference (67).

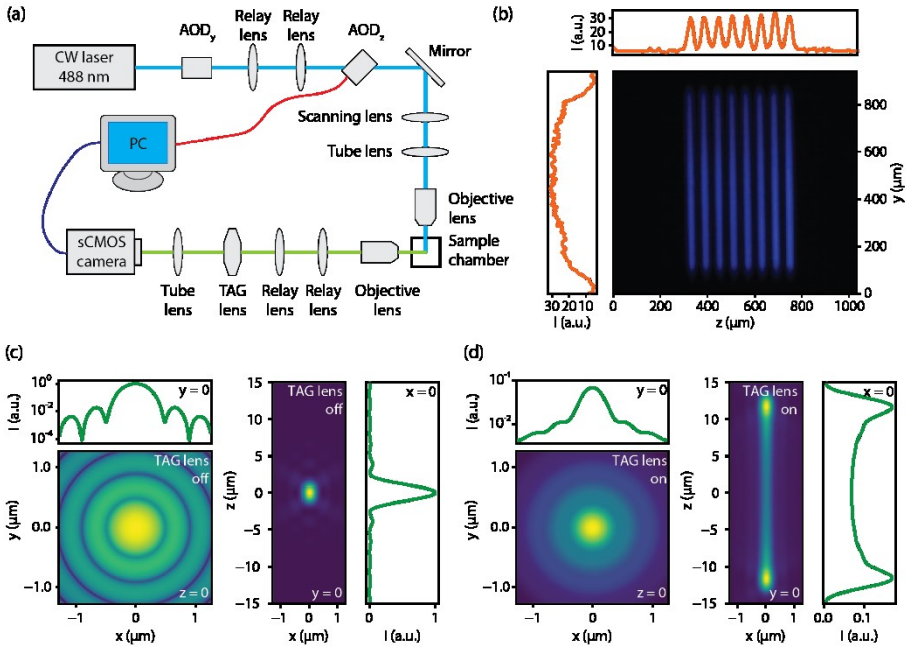

Figure 8.4. (**a**) Schematic representation of the experimental setup. The excitation arm is in blue, the detection one in green. (**b**) Experimental image of light sheets taken at the focal plane of the scanning lens. On top, the illumination intensity profile along the z-axis shows that the light sheets have comparable intensity. On the left, the intensity profile along the y-axis shows a good longitudinal homogeneity. (**c**) Native PSF of the detection objective lens (40×/0.8 NA) was calculated with the Born & Wolf model. The image of the XY plane at z=0 and the corresponding intensity profile are on a logarithmic scale. The DoF, defined as the FWHM along the z-axis, is 1.5 µm. (**d**) Extended PSF was obtained by scanning the native PSF along the z-axis with the TAG lens. In this example, the DoF extension is about 25 µm, but it can be tuned by applying a different drive voltage drive to the TAG lens. The intensity scale is the same as in (**c**). The lateral width is preserved, but the intensity per plane is reduced. Image reproduced from reference (67).

8.1.1 Acousto-Optic Scanning System (AOS)

Acousto-optic deflectors are devices used to deflect a laser beam in one direction by a variable angle, controllable by the frequency of an electrical signal. The working principle is based on the photon-phonon interaction. Such devices are acousto-optic modulators operating with a constant power electrical drive signal and a variable frequency. A Bragg condition determines the direction of the diffracted beam is condition and contains the sound wavelength; the diffraction depends on the sound frequency, which depends on the signal provided controlling the outcoming direction of light. An AOD is made-up of a piezoelectric material driven by opportune frequencies that induce vibration in a crystal. A slab of an acoustic damper is placed on the opposite side of the piezoelectric (**Figure 8.5**, **a-b**). For an isotropic medium, the deflection angle (twice the Bragg angle) can be calculated from the Bragg condition as approximately

$$\Delta\theta = \frac{\lambda}{v}\Delta f$$

Equation 8.1

where λ is the optical vacuum wavelength, f is the driving frequency (equals the acoustic frequency), and v is the velocity of the sound wave in the acousto-optic material. The latter can also be recognized as the ratio of optical wavelength and acoustic wavelength (v/f) and is typically between 10 µm and 100 µm. A sum of sinusoidal with different frequencies can also drive the AOD. In this case, the light will be diffracted with multiple Bragg angles resulting in more than one diffracted beam. This setup includes an Acousto-Optic Scanning (AOS) system made of two AOD (IntraAction, ATD-7010CD2) (**Figure 8.4**, **a**). The first AOD deflects a Gaussian beam along the y-axis, thus generating a digital light sheet for the camera. It is driven by a voltage-controlled oscillator (IntraAction, DE-704M) at the central frequency of 70 MHz (optimal frequency of the AOD) with a 20 kHz frequency modulation using a triangular wave guaranteeing the optimal homogeneity of the light-sheet intensity along the y-axis. Compared to the more traditional cylindrical lens, this approach allows confining the illumination to a region of interest, thus optimizing the photon budget (175). Multiple frequencies drive the second AOD diffracting the incident beam at different angles. The scan lens creates an array of parallel light sheets transforming the angles into unique axial positions. This AOD is controlled by a 14-bit arbitrary waveform generator (Signatec, PXDAC4800), whose output is amplified by a gain block (Mini-circuits, ZHL-1-2WX-S+). A digital I/O device (National Instruments, USB-6501) synchronizes the camera acquisition and the driving signal generation for the AODz. A custom software programmed with LabView controls the complete system. In its present form, the light-sculpting system can switch between two illumination patterns in 5 ms. AODs are a precise tool; applying the same voltage will lead to the same angular shift.

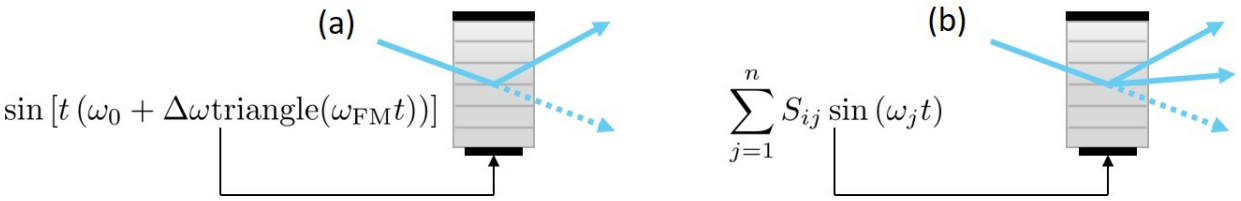

Figure 8.5. Schematic representation of an AOD driven by a sinusoidal wave (**a**) and a sum of sinusoidal waves (**b**). The black slab on the top is the damping material, and the one on the bottom is piezoelectric.

8.1.2 MELM implementation

The AOS scanning system is the key method for generating an array of parallel and identical light sheets that can be rapidly individually switched on and off. A technique to extend the DoF of the objective detection lens is then requested (in the next paragraph, we will comment on two possible approaches). The first AOD generates the light sheet, while the second AOD is used to generate the encoded illumination sequences. To this end, we drive it with a superposition of multiple sine waves V_i while collecting the superpositioned frames F_i:

$$V_i(t) \propto \sum_{j=1}^{n} S_{ij}\, sin(\omega_j t)$$

Equation 8.2

The amplitudes (S_{ij}) are the entries of the encoding matrix S (we described the encoding formalism in **paragraph 3.2.1**), and each acoustic frequency ω_{ij} diffracts the light to different axial positions (176), thus, obtaining an array stack of parallel light sheets illuminating the planes P_j only if $S_{ij} = 1$. As shown in **Figure 8.4** (**b**), the illumination pattern produced with this technique shows good uniformity along the y-axis and intensity of each beam is the same. Notably, the good linearity and almost-flat band of the AOD and its control system enabled to achieve the desired uniformity without applying any additional correction. While other light-sheet parallelization techniques have already been proposed (177,178), acousto-optic light sculpting enables the fastest switch between illumination patterns (179), preserving the speed of LSFM. We can switch between two patterns within 5 ms in our current implementation. This value does not depend on the number of produced beams; in principle, it is possible to reach any amount of parallelization without sacrificing speed.

It is possible to implement MELM in any DoF extending method. In our system, we conjugated the back focal plane of the objective detection lens with a Tunable Acoustic Gradient (TAG) lens, a varifocal lens (180) that rapidly scans the object plane along the optical axis (181), or we introduced a glass slab adding a difference in refractive index that generates spherical aberrations. If the camera exposure time is greater than the period $T = 2\pi/\omega$ of the axial scan (typically in the order of tens of microseconds), a dynamic and tunable EDoF is obtained. The resulting detection Point Spread Function (PSF) of the microscope is then defined as:

$$h_e(x,y,z) = \frac{1}{T}\int_0^T h_o(x,y,z - \Delta z\, cos(\omega t))\mathrm{d}\, t$$

Equation 8.3

Where h_o Is the native detection PSF of the system, and Δz is half of the scanning range. Importantly, changing the driving parameters of the TAG lens, namely the frequency and the voltage amplitude, can tailor Δz. **Figure 8.4** (**c-d**) shows that time-averaging results in an elongated PSF along the optical axis. The resulting time-averaged PSF preserves its width in the x-y plane. However, the out-of-focus contributions of the native PSF produce a lateral broadening of the tails while axially scanning, resulting in additional fluorescent background. Deconvolution is needed, as it typically happens with all EDoF techniques to restore the diffraction-limited images. The independence of the lateral shape of the PSF allows for performing a simple 2D plane-by-plane deconvolution and significantly low the computational cost of the post-processing step compared to other DoF extending methods. The average intensity of the extended PSF is lower than the peak intensity of the axially-scanning PSF, as we show in **Figure 8.4** (**d**); this is an inherent side effect of any DoF extending method: the longer the EdoF, the lower the signal of each plane. With these two modifications in place, image acquisition in MELM proceeds by illuminating the sample with a sequence of multiple light sheets. We selected the encoding method, the extension of the DoF, and the planes to be imaged prior to launching the acquisition by selecting the driving frequencies of both the TAG lens and AOD. Once the stack of encoded frames is collected, we used a single-step decoding algorithm to reconstruct the images of the individual planes.

8.1.3 Tunable Gradient Liquid Lens (TAG Lens)

The tunable acoustic gradient index of refraction lens (or TAG lens) is an adaptive optics device filled with fluid and driven by an acoustic used to generate a tunable focal length by a fast change of refractive index (kHz). TAG lens is generally a cylindrical cavity surrounded by a cylindrical piezoelectric and filled with a fluid (generally oil) where vibrations induce a stationary wave that allows controlling the focus. If the camera frame rate is slower than the resonance frequency of the TAG lens (condition likely to be satisfied), it will result in an extended focus: a focal volume. We performed the following procedure to calibrate the DoF extension provided by the TAG Lens as a function of the voltage applied. We filled the TAG Lens aperture with a Gaussian Beam and measured the transmitted wavefront with a Shack-Hartmann sensor. We synchronized the emission of a laser pulse to a phase value of the oscillation of the TAG Lens, thus measuring the instantaneous wavefront. We fitted the measured wavefront to a parabolic model:

$$\frac{\phi(x,y,t)}{k} = \frac{\alpha(t)}{2}[(x-x_0)^2 + (y-y_0)^2] + \beta$$

Equation 8.4

Thus, obtaining a measure of the instantaneous optical power $\alpha(t)$. By changing the delay t in the synchronization line, we measured the optical power at different times, and we fitted it to the following sinusoidal model:

$$\alpha(t) = \alpha\cos(\omega t + \varphi)$$

Equation 8.5

The amplitude is the optical power at fixed voltage V and frequencyω. Repeating this measurement for different values of driving voltage, we measured the calibration curve (V) for two different resonant frequencies of the TAG lens. We fitted this latter to a linear model:

$$\alpha(V) = mV$$

Equation 8.6

The optical power's slope m is higher for higher resonant frequencies. However, the parabolic region is smaller, thus reducing the available physical aperture. The relationship between the DoF extension and the optical power can be calculated as:

$$EDoF = 2f_0^2\alpha$$

Equation 8.7

8.2 Setup Alignment

The setup properties were investigated through fluorescent Yellow/Green Beads (FluoSpheres™, Invitrogen™). They were used to remove optical aberrations and to quantify the properties of the setup (resolution, pixel size).

8.2.1 Beads Sample

The first step of MELM validation includes numerical simulations. **Figure 8.6** shows the synthetic experiments. Notably, they show a perfect agreement with theory and a clear benefit in terms of contrast and SNR, even in photon noise. As a second step, we performed the imaging of fluorescent beads embedded in agarose gel with a sequential, Black Light Sheet and Hadamard scan (**Figure 8.7**, **a**). All three cases were obtained using the same energy per light sheet and the same camera exposure time for a fair comparison. We set the latter to $2\ \mathrm{ms}$, which added to the $5\ \mathrm{ms}$ required to switch between two encoding patterns, resulting in an acquisition rate of about 150 frames/second. Using such short exposure, the image acquired with the sequential scan is noisy and background-dominated, as we expected. Instead, the Black Light Sheet scan

shows a great suppression of the background, clearly noticeable in the intensity profile, whit no perceptible improvement in the noise level. With the Hadamard scan, we reach significantly high noise suppression with the background level not as low as the previous encoding but still appreciable. **Figure 8.7** (**b-c**) shows the SNR and contrast gain of both encoding methods as a function of the number of frames for a more quantitative analysis highlighting a perfect agreement with the theoretical models discussed before: the Hadamard scan provides an SNR gain monotonically increasing with n, reaching an improvement of about 50% at $n = 15$ while the Black Light Sheet scan provides the maximum gain at $n = 3$, which then decreases. Eventually, for high values of n, it loses its SNR advantage but maintains the background suppression.

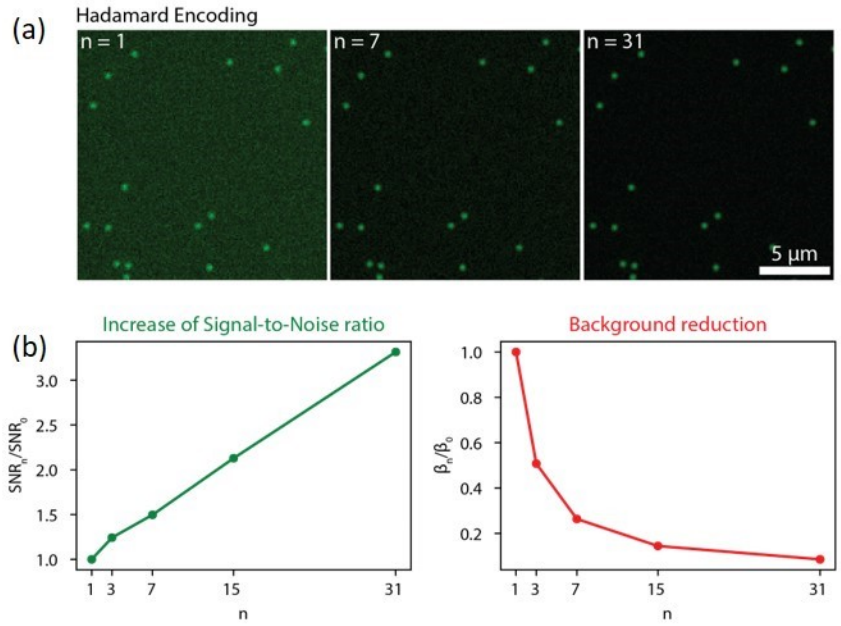

Figure 8.6. Results of the simulations. (**a**) On the left image of the original plane (n = 1). On the right, images of the same plane are encoded with the Hadamard method, using 7 and 31 frames. (**b**) Quantitative analysis of the SNR enhancement and background suppression. Both quantities are plotted against the number n of acquired frames. Image reproduced from reference (67).

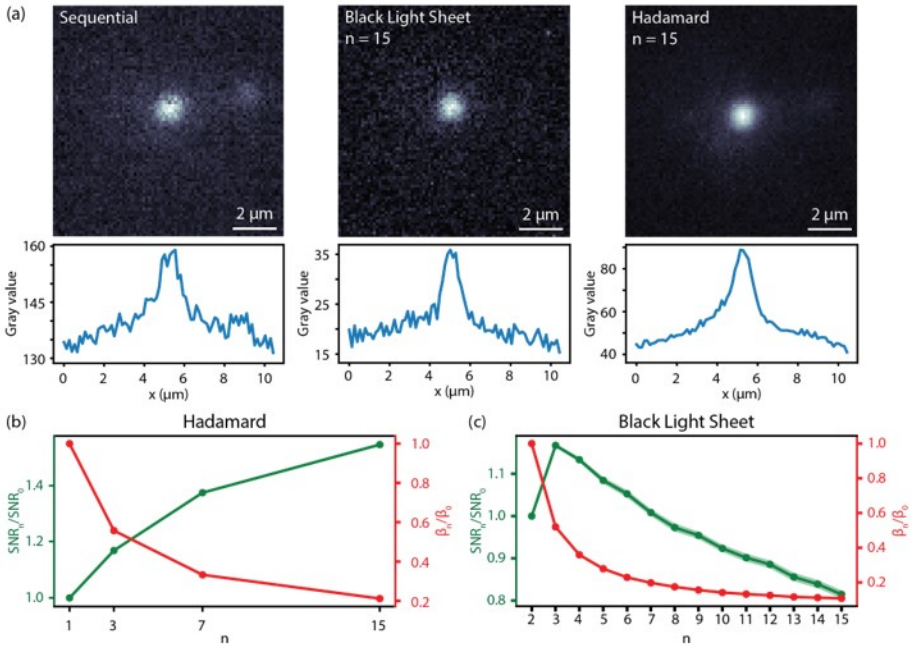

Figure 8.7. (**a**) Top: Images of the single 1 µm fluorescent bead were acquired with three different encoding methods (Sequential, Black Light-sheet, and Hadamard scan). Bottom: Corresponding intensity profile, averaged over the columns. (**b**) Quantitative analysis of the normalized SNR gain (green) and background suppression (red) was obtained with the Hadamard encoding. (**c**) Quantitative analysis of the normalized SNR gain (green) and background suppression (red) was obtained with the Black Light Sheet encoding. The error bar is shown as a shaded area when bigger than exceeding the line width. The images have been acquired with a 40×\/0.8 NA objective lens, whose DoF has been extended from 1 µm to 60 µm with the TAG lens. Image reproduced from reference (67).

8.3 Results

Sample preparation: We prepared the beads samples using solutions of 1 µm Yellow/Green beads (FluoSpheres™, Invitrogen™) diluted in 2% agarose gel at a concentration of 1:500. The pollen samples were prepared directly by harvesting the grains from the flower. We embedded them in 2% agarose gel aspirated with a capillary tube.

As a 3D model, we prepared spheroids samples using human embryonic kidney cells (HEK 293), stably transfected with the plasmid encoding for EGFP-Δ50 lamin-A (Addgene plasmid #17653). We started from a dish of confluent cells, diluted them to form a suspension of 10,000 cells/mL, and seeded them into a 96-wells microplate (Corning Spheroid Microplate). After three days of growth, we fixed the spheroids with 4% paraformaldehyde for 30 minutes at room temperature and cleared them with Rapiclear 1.47 for 10 minutes (Sun Jin Lab Co.). Subsequently, we embedded the individual spheroids in a 2% agarose gel cylinder for imaging.

8.3.1 3D Samples

As a proof of concept in a 3D sample, we imaged a fluorescently labeled spheroid of human embryonic kidney cells selecting the Hadamard scan given its superior SNR enhancement capabilities in the presence of shot noise. In **Figure 8.8** (**a**), we show the maximum intensity projections of a reconstructed volume of $278.5 \times 278.5 \times 83.7\ \mu m^3$With a voxel size of $0.5 \times 0.5 \times 5.6\ \mu m^3$ ($n = 15$). We set the camera exposure time to 100 ms, resulting in a volumetric imaging time of 1.5 s. Given the dense labeling of the spheroid and the camera exposure, the photon noise is not negligible. Consequently, the enhancement in SNR is lower in fluorescent beads. **Figure 8.8** (**b**) reports a more detailed analysis of the noise and background reduction. At the described experimental conditions, the SNR is still increasing with n, but for $n = 3$ and $n = 7$ it is lower than that of the sequential scan. However, for $n = 15$, we reached an SNR gain of about 20% and a contrast gain of about 100% with no cost for 3D imaging speed.

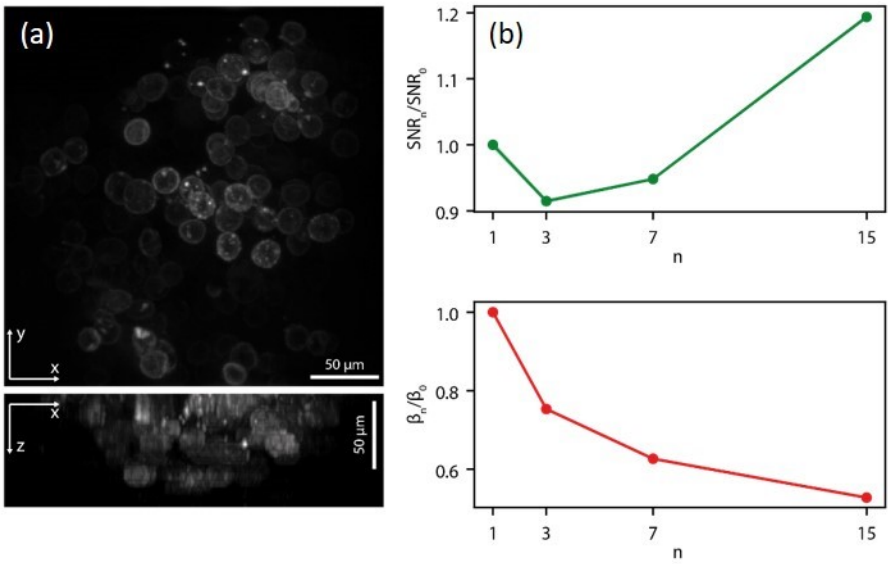

Figure 8.8. (**a**) Maximum intensity projection of the volumetric image of a spheroid acquired with Hadamard encoding. Images have been deconvolved with the Wiener filter algorithm, using a PSF simulated with **Equation 8.3** (**b**) SNR gain and background suppression versus the number of acquired frames. Images have been acquired with a $10 \times /0.3\ NA$ objective lens, whose DoF has been extended from 7 μm to 215 μm with the TAG lens. The 3D image is composed of two interdigitated stacks of 15 frames.

The values reported here regarding the enhancement in SNR could be further increased by increasing n -the SNR gain is expected to approximately scale with the square root of the number of frames. However, we must consider some practical limitations, such as the resolution and angular range of the deflector or the power of the laser source. Also, we must take some care must when using our parallelization strategy. Cross-correlation is

another potential issue: If beams are overlapping, a sample region will be illuminated by more than a single light sheet, failing the hypothesis of independent planes needed for the reconstruction. In this case, reconstruction is likely to generate artifacts. On a positive note, MELM is an extremely efficient technique for illumination. Indeed, all available power of the light source can be used – the higher the power, the higher the number of planes that can be illuminated. Thus, we can maximize the photon budget and speed of EDoF-SPIM and still preserve the very low photodamage of SPIM.

A central benefit of MELM is its compatibility with any DoF extending method and encoding matrix. To verify this aspect of the technique, we acquired images of a pollen grain with an EDoF generated by introducing spherical aberrations to our system (**Figure 8.9**, **a-b**) (182): spherical aberrations produce an elongated PSF – however, at the cost of losing uniformity, thus requiring advanced 3D deconvolution for image restoration.

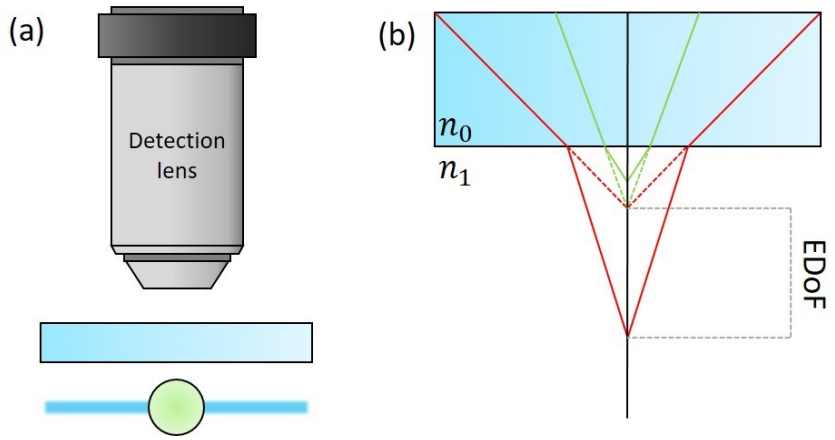

Figure 8.9. Schematic representation of Spherical aberrations assisted Extended Depth-of-field (SPED) light-sheet microscopy. A glass slab (or another material) is placed between the sample and the detection microscope (**a**). In (**b**), we can see the spherical aberration induced by the refractive index mismatch.

In this experiment, a slab of glass, placed between a $40\times/0.8\ NA$ objective lens and the sample, increases spherical aberrations, resulting in an EDoF of about $30\ \mu\mathrm{m}$. In contrast to varifocal lenses for EDoF, this technique is not tunable in real-time. **Figure 8.10** shows images of a pollen grain obtained with the sequential, Black Light Sheet and Hadamard scans for up to $n = 7$ frames, in line with those obtained with the TAG lens and in agreement with theory.

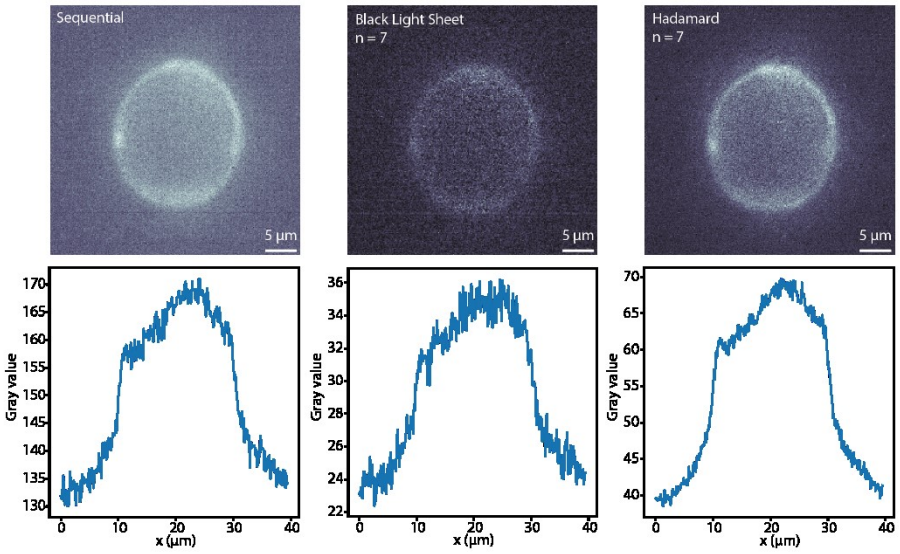

Figure 8.10. *Top*. The same image of a single pollen grain bead taken with three different encoding methods and depth-of-field extended through spherical aberration. *Bottom*. Intensity profile, averaged over the columns of the corresponding images.

8.4 Conclusions and future perspectives

Combining EDoF detection with parallelized illumination enables overcoming the tradeoff between speed and SNR in SPIM in conditions of low photon noise is likely encountered in fast volumetric imaging. Our results demonstrate that sample illumination with sequences of multiple light sheets produces enhanced SNR and contrast images. Because no moving optics are being used, the intrinsic high speed of EDoF-SPIM is preserved. This approach is *absolutely* general since the encoding sequence can be selected to address the imaging needs of a particular sample or application to any DoF extending technique. Furthermore, the increased SNR enables smaller laser doses, further decreasing the risk of photodamage and allowing the chance to work in a situation where it is impossible to raise the SNR through laser powering. It is also important to notice that this approach comes from spectroscopy (173). In **paragraph 6.2.1**, we described a PA spectroscopic system whose architecture is analogous to a SPIM. We noticed that while working a low temperatures **Figure 6.18** (**c-d**), the thermal noise becomes prominent in the signal (109). In this latter situation was not possible to increase the laser power for the photosensitivity of the tested proteins. Here we propose a theoretical description of a possible application of light encoding for thermal noise suppression in PA spectroscopy.

8.4.1 Possible application for Photoacoustic Spectroscopy

As we mentioned, PA signals are strongly affected by thermal noise. The thermal noise (Johnson–Nyquist noise) is generated by charge carriers inside the electrical conductors. Thermal noise has a nearly Gaussian amplitude distribution in a finite bandwidth, fulfilling

the hypothesis made in **paragraph 3.2.1** about standard deviation and independence from measurements. We previously described this type of noise in **paragraph 4.3.3**, where we saw that it depends mainly on the properties of the setup and the temperature. We also mentioned the evidence that reducing the temperature brings lowering SNR: If we low the temperature, both noise and signal decrease but the strong dependence of the latter on temperature (trough expansion coefficient) worsens the SNR. Here we propose a simple simulation showing this approach's benefits to a PA spectroscopic setup. We simulated our experimental data as a convolution of a damped oscillation as a response function (**Figure 8.11,** *bottom*) of the ultrasound transducer and an exponential step function representing the pressure profile of a slab. The resulting function agrees with the first slope of the experimental data acquired for BBBN (**Figure 8.11,** *top*).

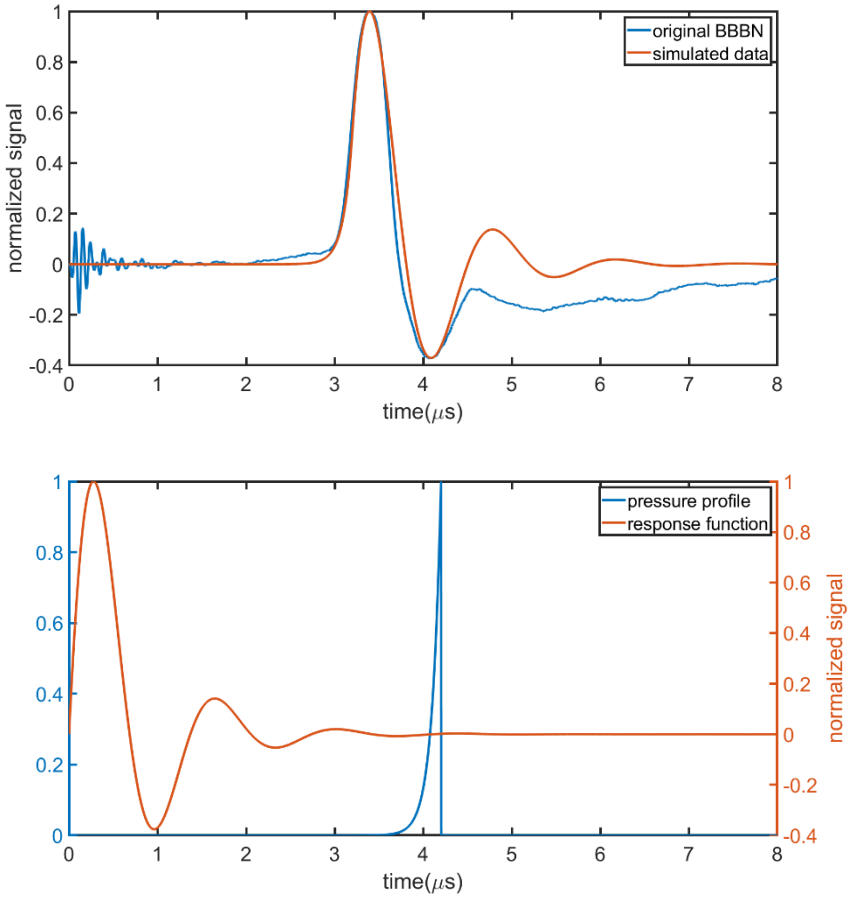

Figure 8.11. *Top*. Comparison between experimental data obtained on BBBN calorimetric reference (blue) and synthetic data (red). *Bottom*. The pressure profile and the response function of the transducer are used for convolution.

In the next step, we generate the signal matrix, following both single scan and Hadamard construction. The noise (Gaussian noise), considered dependent only on the setup used,

is added. After deconvolution, we quantify the SNR and background as we previously did for MELM. In the figures below (**Figure 8.12**, **Figure 8.13**, **Figure 8.14**, **Figure 8.15**), we compare signals obtained with both sequential and Hadamard scans and the decoded images. We generate the following synthetic data using the commercial software MatLab (The MathWorks, Inc., USA).

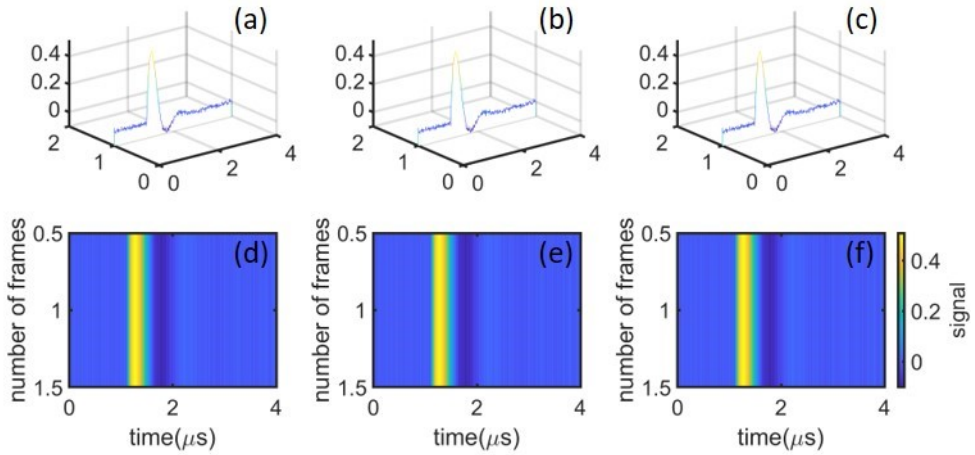

Figure 8.12. Waterfall and contour plots of (**a,d**) PA signal in sequential scan mode, (**b,e**) Hadamard encoded PA signals and (**c,f**) decoded sequential PA signals. The case for n=1.

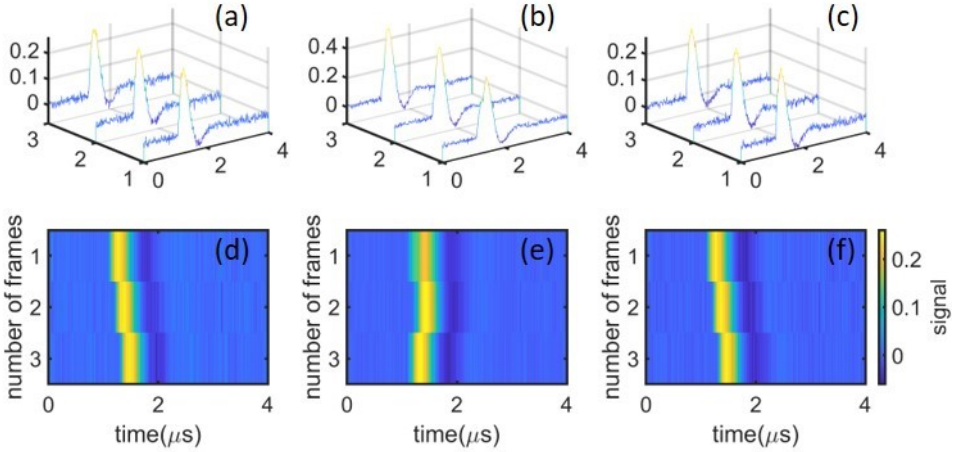

Figure 8.13. Waterfall and contour plots of (**a,d**) PA signal in sequential scan mode, (**b,e**) Hadamard encoded PA signals and (**c,f**) decoded sequential PA signals. The case for n=3.

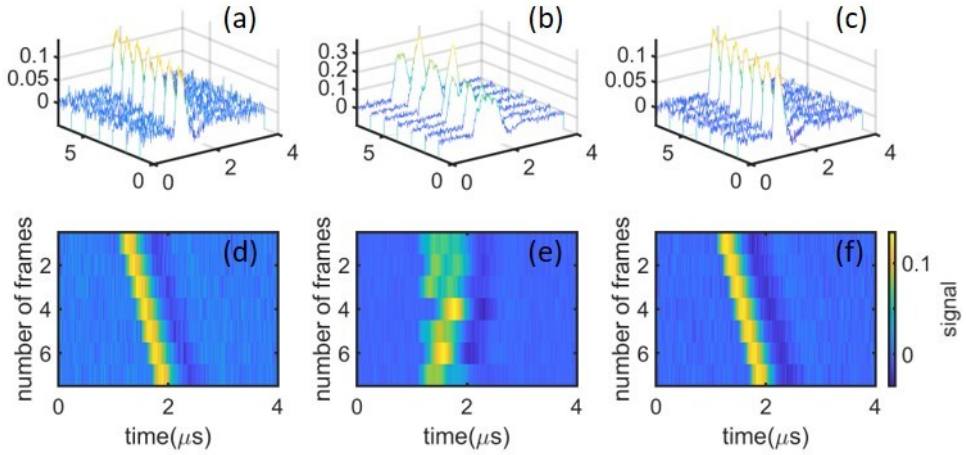

Figure 8.14. Waterfall and contour plots of (**a,d**) PA signal in sequential scan mode, (**b,e**) Hadamard encoded PA signals and (**c,f**) decoded sequential PA signals. The case for n=7.

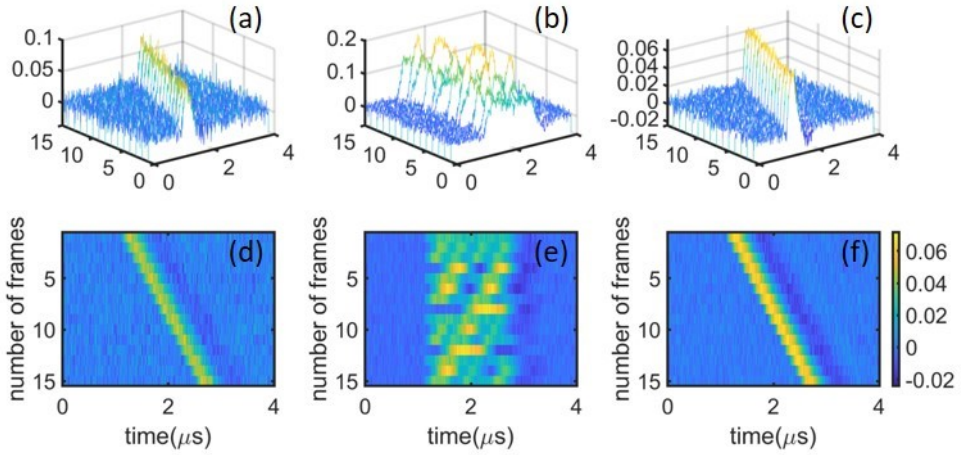

Figure 8.15. Waterfall and contour plots of (**a,d**) PA signal in sequential scan mode, (**b,e**) Hadamard encoded PA signals and (**c,f**) decoded sequential PA signals. The case for n=15. The scale bar represents the signal's intensity.

From the last image (**Figure 8.16**), we can see the analogous improvement compared to MELM, demonstrating the feasibility of light encoding theoretically for SNR (**a**) enhancement and background suppression (**b**) in the system affected by thermal noise like PA spectroscopy, which, indeed, shows analog architecture to SPIM. We report SNR and Background normalized for the corresponding value in the sequential scan (SNR_0 and β_0).

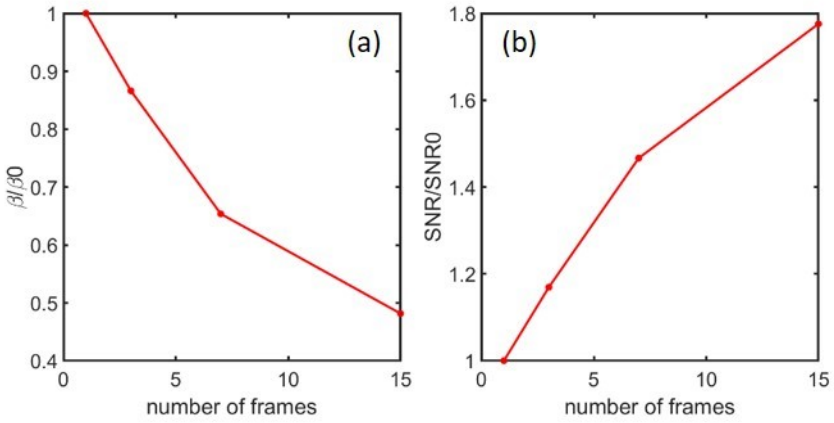

Figure 8.16. (**a**) Quantitative analysis of the normalized background suppression obtained with the Hadamard encoding. (**b**) Quantitative analysis of the normalized SNR gain obtained with the Hadamard encoding.

As we pointed out in **Chapter 6**, the application of photochromic probes to photoacoustic microscopy and spectroscopy brings advantages in terms of contrast enhancement but, as we can see from **Figure 6.8** and **Figure 6.9**, it has the main drawback of noise propagation. From this evidence, we hypnotize a combined approach of these two techniques where photochromic probes provide contrast enhancement and the possibility to extract the signal from a scattering/absorbing background, and the light parallelization allows background suppression and SNR enhancement.

Conclusions

This thesis contributes to the field of photoacoustic microscopy (PAM) with the intent to explore the application of photochromic probes and novel illumination geometries to enhance contrast and signal-to-noise ratio. We were motivated by the evidence that photoacoustic microscopy is becoming a prominent methodology in life sciences, mostly for its penetration depth and the potentially wider choice of existing contrast agents, including endogenous ones, compared to fluorescent probes. Still, PAM suffers from many technical limitations: the acoustic nature of the detected signal provides poor spatial resolution compared to light, and in general, there is a strong tradeoff between sensitivity and acquisition speed. With this work, we have explored some possible solutions to this issue.

As a first point, we have considered the possibility of applying photochromic FPs to PAM, motivated by the fact that they may allow us to improve resolution similar to those observed in fluorescence microscopy methods such as RESOLFT STORM and qOLID. We thus started developing new probes by modifying GFPs derivatives historically used as fluorescent labels in microscopy. Since strong fluorescence emission that characterizes GFPs results in low efficiency in generating PA waves through heat release, we thus developed photochromic GFPs derivatives with low fluorescence quantum yields. Our attempts allowed us to obtain GFP mutants with low fluorescence emission, but unfortunately, with poor photoconversion yields. We then moved to a different class of FPs, the cyanobacteriochromes (CBCR). CBCRs are photochromic domains found in cyanobacteria. When bound to a biliverdin chromophore, they usually display a photochromic behavior between red and far-red emitting states. In this work, we performed a photoacoustic spectroscopy characterization of the green/red photochromic CBCR slr1393 (GAF3) bound to phycocyanobilin. We determined the volume and enthalpy changes following photoexcitation of the protein and showed how the photochromic properties result in photoacoustic signals that could be exploited to increase contrast in PAM. To prove this concept, we have devised a phantom based on a capillary tube filled with a photochromic solution (purified GAF3 or bacteria overexpressing GAF3) inserted in an absorbing or scattering solution (BBBN or bacteria) to simulate a background effect. We found out that, especially under red excitation, the photochromic behavior of GAF3 allows discriminating the phantom from the environment. The next step will be then applying photochromic probes to PAM. Since PAM allows the detection of morphological features located deeper in tissues than those visualized by fluorescence microscopy, we have considered a proper excitation system to take full advantage of acoustic waves' properties. We then developed a photoacoustic microscope based on two-photon excitation (2P-PAM). This system provided unique lateral and axial resolution. Although

modulated excitation provides lower sensitivity than pulsed excitation, it provides a higher acquisition rate. To improve the sensitivity, an important contribution may come from the future application of the above photochromic probes in the same way they are used to qOLID. Using samples of biological (cerebellum slides, stained with histological stain) and non-biological (metal grids) origin, we showed that this technique holds great potential.

Finally, we have developed an illumination geometry intended to improve the signal-to-noise ratio (SNR), which is generally used and could be specialized for photochromic samples. The idea of Multiplane Light Encoded Microscopy (MELM) is based on the evidence that sharing the noise contribution over more than one plane allows for enhancing SNR. We built a SPIM setup including an acousto-optic scanning system (AOS) to generate an encoded sequence of light sheets to shine the sample and a depth-of-field (DoF) extending method to acquire more than one plane simultaneously. The general encoding matrix and DoF extension can be specialized to specific experimental needs. To prove the concept, we performed MELM experiments on a thick sample: a spheroid expressing EGFP-Δ50 lamin-A (codifying for Progeria disease). The results showed a good improvement in both SNR and background suppression provided by our methods. Since this setup shares the configuration with those used for PA spectroscopy, we foresee applications of the MELM approach and, more generally, a multiplexing approach to PA spectroscopy and microscopy. We support our conclusions with synthetic data, where we simulated the photoacoustic response of a slab of light on a transducer affected by Gaussian thermal noise. As a result, we find out the very same behavior we found for MELM applied to SPIM. We strongly believe that parallelization will then be applied to PA spectroscopy, enhancing the overall performance. In fact, the kinetic studies we performed, especially while working at low temperatures, are strongly affected by noise (we remind that the PA signal has a stronger dependence on temperature than noise). The study of protein dynamics, including structural changes, may benefit from this approach.

Bibliography

1. Diaspro A, Chirico G, Collini M. Two-photon fluorescence excitation and related techniques in biological microscopy. Q Rev Biophys. 2005 May;38(2):97–166.

2. Zipfel WR, Williams RM, Webb WW. Nonlinear magic: multiphoton microscopy in the biosciences. Nat Biotechnol. 2003 Nov;21(11):1369–77.

3. Gensch T, Viappiani C. Time-resolved photothermal methods: Accessing time-resolved thermodynamics of photoinduced processes in chemistry and biology. Photochem Photobiol Sci. 2003;2(7):699–721.

4. Tsien RY. The Green Fluorescent Protein. Annu Rev Biochem [Internet]. 1998 Jun 1;67(1):509–44. Available from: https://doi.org/10.1146/annurev.biochem.67.1.509

5. Shimomura O. Discovery of Green Fluorescent Protein, in Green Fluores- cent Protein: Properties, Applications, and Protocols, Second Edition (ed.: M. Chalfie, S. R. Kain). 2006. cap 1.

6. O. Shimomura, F. H. Johnson YS. Extraction, purification and properties of aequorin, a bioluminescent protein from the luminous hy- dromedusan, Aequorea. J Cell Comp Physiol. 2002;59:223–39.

7. Shimomura O. Nobel Lectures Discovery of Green Fluorescent Protein (GFP) (Nobel Lecture)**. 2009;5590–602.

8. Matz M V, Fradkov AF, Labas YA, Savitsky AP, Zaraisky AG, Markelov ML, et al. Fluorescent proteins from nonbioluminescent Anthozoa species. Nat Biotechnol [Internet]. 1999 Oct 1;17:969. Available from: http://dx.doi.org/10.1038/13657

9. Miyawaki A. Green Fluorescent Protein-like Proteins in Reef Anthozoa Animals. Cell Struct Funct. 2002;27(5):343–7.

10. Ikeuchi M, Ishizuka T. Cyanobacteriochromes : a new superfamily of tetrapyrrole-binding photoreceptors in cyanobacteria †. 2008;1159–67.

11. Barondeau DP, Putnam CD, Kassmann CJ, Tainer JA, Getzoff ED. Mechanism and energetics of green fluorescent protein chromophore synthesis revealed by trapped intermediate structures. Proc Natl Acad Sci [Internet]. 2003 Oct 14;100(21):12111 LP-12116. Available from: http://www.pnas.org/content/100/21/12111.abstract

12. Jung G, Wiehler J, Zumbusch A. The Photophysics of Green Fluorescent Protein: Influence of the Key Amino Acids at Positions 65, 203, and 222. Biophys J [Internet]. 2005 Mar 1;88(3):1932–47. Available from:

https://doi.org/10.1529/biophysj.104.044412

13. A. A. Pakhomov VIM. GFP Family: Structural Insights into Spectral Tuning. Chem & Biol. 2008;15:755–64.

14. Bizzarri R, Serresi M, Cardarelli F, Abbruzzetti S, Campanini B, Viappiani C, et al. Single Amino Acid Replacement Makes Aequorea victoria Fluorescent Proteins Reversibly Photoswitchable. J Am Chem Soc [Internet]. 2010 Jan 13;132(1):85–95. Available from: https://doi.org/10.1021/ja9014953

15. Butler WL, Norris KH, Siegelman HW, Hendricks SB. DETECTION, ASSAY, AND PRELIMINARY PURIFICATION OF THE PIGMENT CONTROLLING PHOTORESPONSIVE DEVELOPMENT OF PLANTS. Proc Natl Acad Sci U S A [Internet]. 1959 Dec;45(12):1703–8. Available from: https://pubmed.ncbi.nlm.nih.gov/16590561

16. Rockwell NC, Su Y-S, Lagarias JC. PHYTOCHROME STRUCTURE AND SIGNALING MECHANISMS. Annu Rev Plant Biol [Internet]. 2006;57(1):837–58. Available from: https://doi.org/10.1146/annurev.arplant.56.032604.144208

17. Sage LC. Pigment of the imagination: a history of phytochrome research. Elsevier; 2012.

18. Karniol B, Vierstra RD. Photomorphogenesis in Plants and Bacteria: Function and Signal Transduction Mechanism. Springer, Dordrecht The Netherlands; 2005.

19. Auldridge ME, Forest KT. Bacterial phytochromes: more than meets the light. Crit Rev Biochem Mol Biol. 2011 Feb;46(1):67–88.

20. Liu YC, Machuca MA, Beckham SA, Gunzburg MJ, Roujeinikova A. Structural basis for amino-acid recognition and transmembrane signalling by tandem Per-Arnt-Sim (tandem PAS) chemoreceptor sensory domains. Acta Crystallogr D Biol Crystallogr. 2015 Oct;71(Pt 10):2127–36.

21. Möglich A, Ayers RA, Moffat K. Structure and signaling mechanism of Per-ARNT-Sim domains. Structure. 2009 Oct;17(10):1282–94.

22. Hennig S, Strauss HM, Vanselow K, Yildiz Ö, Schulze S, Arens J, et al. Structural and Functional Analyses of PAS Domain Interactions of the Clock Proteins Drosophila PERIOD and Mouse PERIOD2. PLOS Biol [Internet]. 2009 Apr 28;7(4):e1000094. Available from: https://doi.org/10.1371/journal.pbio.1000094

23. Ponting CP, Aravind L. PAS: a multifunctional domain family comes to light. Vol. 7, Current biology : CB. England; 1997. p. R674-7.

24. Hefti MH, Françoijs K-J, de Vries SC, Dixon R, Vervoort J. The PAS fold. A redefinition of the PAS domain based upon structural prediction. Eur J Biochem. 2004

Mar;271(6):1198–208.

25. Takala H, Björling A, Berntsson O, Lehtivuori H, Niebling S, Hoernke M, et al. Signal amplification and transduction in phytochrome photosensors. Nature. 2014 May;509(7499):245–8.

26. Legris M, Ince YÇ, Fankhauser C. Molecular mechanisms underlying phytochrome-controlled morphogenesis in plants. Nat Commun [Internet]. 2019;10(1):5219. Available from: https://doi.org/10.1038/s41467-019-13045-0

27. Müller K, Engesser R, Timmer J, Nagy F, Zurbriggen MD, Weber W. Synthesis of phycocyanobilin in mammalian cells. Chem Commun (Camb). 2013 Oct;49(79):8970–2.

28. Rockwell NC, Lagarias JC. Phytochrome diversification in cyanobacteria and eukaryotic algae. Curr Opin Plant Biol. 2017 Jun;37:87–93.

29. Chen Y, Zhang J, Luo J, Tu J-M, Zeng X-L, Xie J, et al. Photophysical diversity of two novel cyanobacteriochromes with phycocyanobilin chromophores: photochemistry and dark reversion kinetics. FEBS J. 2012 Jan;279(1):40–54.

30. Oliinyk OS, Shemetov AA, Pletnev S, Shcherbakova DM, Verkhusha V V. Smallest near-infrared fluorescent protein evolved from cyanobacteriochrome as versatile tag for spectral multiplexing. Nat Commun [Internet]. 2019;10(1):279. Available from: https://doi.org/10.1038/s41467-018-08050-8

31. Lukyanov KA, Chudakov DM, Lukyanov S, Verkhusha V V. Photoactivatable fluorescent proteins. Nat Rev Mol Cell Biol [Internet]. 2005 Sep 15;6:885. Available from: http://dx.doi.org/10.1038/nrm1741

32. Lippincott-Schwartz J, Patterson GH. Fluorescent Proteins for Photoactivation Experiments. Methods Cell Biol [Internet]. 2008 Jan 1 [cited 2018 Oct 19];85:45–61. Available from: https://www.sciencedirect.com/science/article/pii/S0091679X08850030?via%3Dihub

33. Lippincott-Schwartz J, Patterson GH. Photoactivatable fluorescent proteins for diffraction-limited and super-resolution imaging. Trends Cell Biol [Internet]. 2009 Nov;19(11):555–65. Available from: http://www.ncbi.nlm.nih.gov/pmc/articles/PMC3663713/

34. Fron E, Van der Auweraer M, Hofkens J, Dedecker P. Excited State Dynamics of Photoswitchable Fluorescent Protein Padron. J Phys Chem B [Internet]. 2013 Dec 27;117(51):16422–7. Available from: https://doi.org/10.1021/jp409654f

35. Storti B, Margheritis E, Abbandonato G, Domenichini G, Dreier J, Testa I, et al. Role

of Gln222 in Photoswitching of Aequorea Fluorescent Proteins: A Twisting and H-Bonding Affair? ACS Chem Biol. 2018;13(8):2082–93.

36. Kao Y-T, Zhu X, Min W. Protein-flexibility mediated coupling between photoswitching kinetics and surrounding viscosity of a photochromic fluorescent protein. Proc Natl Acad Sci [Internet]. 2012;109(9):3220–5. Available from: https://www.pnas.org/content/109/9/3220

37. Xu X, Höppner A, Wiebeler C, Zhao K-H, Schapiro I, Gärtner W. Structural elements regulating the photochromicity in a cyanobacteriochrome. Proc Natl Acad Sci [Internet]. 2020 Feb 4;117(5):2432 LP-2440. Available from: http://www.pnas.org/content/117/5/2432.abstract

38. Schindelin J, Arganda-Carreras I, Frise E, Kaynig V, Longair M, Pietzsch T, et al. Fiji: an open-source platform for biological-image analysis. Nat Methods [Internet]. 2012;9(7):676–82. Available from: https://doi.org/10.1038/nmeth.2019

39. Clegg R. Förster resonance energy transfer—FRET: what is it, why do it, and how it's done". In Gadella, Theodorus W. J. FRET and FLIM Techniques. Lab Tech Biochem Mol Biol. 2009;33:1–57.

40. Parson WW. Modern optical spectroscopy. Vol. 2. Springer; 2007.

41. Valeur B, Berberan-Santos MN. Molecular fluorescence: principles and applications. John Wiley & Sons; 2012.

42. Vetschera P, Mishra K, Fuenzalida-werner JP, Chmyrov A, Ntziachristos V, Stiel AC. Characterization of Reversibly Switchable Fluorescent Proteins in Optoacoustic Imaging. Anal Chem. 2018;90:10527–35.

43. Abbandonato G, Signore G, Nifosì R, Voliani V, Bizzarri R, Beltram F. Cis-trans photoisomerization properties of GFP chromophore analogs. Eur Biophys J. 2011 Nov;40(11):1205–14.

44. Abbandonato G, Storti B, Signore G, Beltram F, Bizzarri R. Quantitative optical lock-in detection for quantitative imaging of switchable and non-switchable components. Microsc Res Tech [Internet]. 2016;79(10):929–37. Available from: https://analyticalsciencejournals.onlinelibrary.wiley.com/doi/abs/10.1002/jemt.22724

45. Oliinyk OS, Chernov KG, Verkhusha V V. Bacterial Phytochromes, Cyanobacteriochromes and Allophycocyanins as a Source of Near-Infrared Fluorescent Probes. Int J Mol Sci. 2017 Aug;18(8).

46. Shcherbakova DM, Shemetov AA, Kaberniuk AA, Verkhusha V V. Natural photoreceptors as a source of fluorescent proteins, biosensors, and optogenetic

tools. Annu Rev Biochem. 2015;84:519–50.

47. Chernov KG, Redchuk TA, Omelina ES, Verkhusha V V. Near-Infrared Fluorescent Proteins, Biosensors, and Optogenetic Tools Engineered from Phytochromes. Chem Rev. 2017 May;117(9):6423–46.

48. Shcherbakova DM, Baloban M, Verkhusha V V. Near-infrared fluorescent proteins engineered from bacterial phytochromes. Curr Opin Chem Biol. 2015 Aug;27:52–63.

49. Drobizhev M, Makarov NS, Tillo SE, Hughes TE, Rebane A. Two-photon absorption properties of fluorescent proteins. Nat Methods. 2011 May;8(5):393–9.

50. Sir ohn F rederick W illiam H erschel BJ. IV. ’Αμόρφωτα, no. I.— on a case of superficial colour presented by a homogeneous liquid internally colourless. Philos Trans R Soc London [Internet]. 1845 Dec 31 [cited 2022 Feb 28];135:143–5. Available from: https://royalsocietypublishing.org/doi/abs/10.1098/rstl.1845.0004

51. Heimstädt O. Das fluoreszenzmikroskop. Z Wiss Mikrosk. 1911;28:330–7.

52. Konen H, Braunschweig DL der G. Verzeichnis der seit 1908 erschienenen Arbeiten über Photolumineszenz. Fluoreszenz und Phosphoreszenz im Lichte der Neueren Atomtheorie. 1921;101:187.

53. Lehmann H. Das Luminszenz-Mikroskop: seine Grundlagen und seine Anwendungen. 1913.

54. Coons A, Coon Creech H, Jones R, Berliner E. The demonstration of pneumococcal antigen in tissues by the use of fluorescent antibody [Internet]. Journal of Immunology. 1942 [cited 2022 Feb 28]. p. 159–70. Available from: https://www.webofscience.com/wos/woscc/full-record/WOS:000186931900001?SID=C2JEPCS2umHijI4WTAe

55. Chalfie M, Tu Y, Euskirchen G, Ward WW, Prasher DC. Green fluorescent protein as a marker for gene expression. Science [Internet]. 1994 [cited 2022 Feb 28];263(5148):802–5. Available from: https://pubmed.ncbi.nlm.nih.gov/8303295/

56. Prasher DC, Eckenrode VK, Ward WW, Prendergast FG, Cormier MJ. Primary structure of the Aequorea victoria green-fluorescent protein. Gene. 1992 Feb 15;111(2):229–33.

57. Heim R, Tsien RY. Engineering green fluorescent protein for improved brightness, longer wavelengths and fluorescence resonance energy transfer. Curr Biol [Internet]. 1996 [cited 2022 Feb 28];6(2):178–82. Available from: https://pubmed.ncbi.nlm.nih.gov/8673464/

58. Fritschy J-M, Härtig W. Immunofluorescence [Internet]. eLS. 2001. (Major Reference Works). Available from: https://doi.org/10.1038/npg.els.0001174

59. JR L. Principles of Fluorescence Spectroscopy. 2006.

60. Tran PT, Chang F. Transmitted Light Fluorescence Microscopy Revisited. https://doi.org/102307/1543340 [Internet]. 2016 Sep 29 [cited 2022 Feb 28];201(2):235–6. Available from: https://www.journals.uchicago.edu/doi/abs/10.2307/1543340

61. K. A. Lukyanov, D. M. Chudakov, S. Lukyanov VVV. Innovation: Photoactivatable fluorescent proteins. Nat Rev Mol Cell Biol. 2005;6 (11):885–91.

62. Sheppard CJR, Choudhury A. Image Formation in the Scanning Microscope. Opt Acta Int J Opt [Internet]. 1977;24(10):1051–73. Available from: https://doi.org/10.1080/713819421

63. Stender AS, Marchuk K, Liu C, Sander S, Meyer MW, Smith EA, et al. Single Cell Optical Imaging and Spectroscopy. Chem Rev [Internet]. 2013 Apr 10;113(4):2469–527. Available from: http://www.ncbi.nlm.nih.gov/pmc/articles/PMC3624028/

64. VOIE AH, BURNS DH, SPELMAN FA. Orthogonal-plane fluorescence optical sectioning: Three-dimensional imaging of macroscopic biological specimens. J Microsc [Internet]. 1993;170(3):229–36. Available from: https://onlinelibrary.wiley.com/doi/abs/10.1111/j.1365-2818.1993.tb03346.x

65. Stelzer EHK, Lindek S. Fundamental reduction of the observation volume in far-field light microscopy by detection orthogonal to the illumination axis: confocal theta microscopy. Opt Commun. 1994;111(5–6):536–47.

66. Huisken J, Swoger J, Del Bene F, Wittbrodt J, Stelzer EHK. Optical sectioning deep inside live embryos by selective plane illumination microscopy. Science. 2004 Aug;305(5686):1007–9.

67. Zunino A, Garzella F, Trianni A, Saggau P, Bianchini P, Diaspro A, et al. Multiplane Encoded Light-Sheet Microscopy for Enhanced 3D Imaging. ACS Photonics [Internet]. 2021 Nov 17;8(11):3385–93. Available from: https://doi.org/10.1021/acsphotonics.1c01401

68. Sloane NJ. Multiplexing Methods in Spectroscopy. Math Mag [Internet]. 1979;52(2):71–80. Available from: http://www.jstor.org/stable/2689843

69. Nitzsche G, Riesenberg R. Noise, Fluctuation and HADAMARD-Transform-Spectrometry. In: Fluctuations and Noise in Photonics and Quantum Optics. 2003. p. 273–82.

70. Harwit M, Sloane NJA, Sloane I, James N. HADAMARD TRANSFORM OPTICS. 1979.

71. Murphy D, Davidson M. Fundamentals of Light Microscopy and Electronic Imaging. 2nd ed. Wiley; 2012.

72. Gustafsson MGL. Surpassing the lateral resolution limit by a factor of two using structured illumination microscopy. J Microsc [Internet]. 2000;198(2):82–7. Available from: https://onlinelibrary.wiley.com/doi/abs/10.1046/j.1365-2818.2000.00710.x

73. Abbe E. Beiträge zur Theorie des Mikroskops und der mikroskopischen Wahrnehmung. Arch für Mikroskopische Anat [Internet]. 1873;9(1):413–68. Available from: https://doi.org/10.1007/BF02956173

74. F.R.S. LR. XXXI. Investigations in optics, with special reference to the spectroscope. London, Edinburgh, Dublin Philos Mag J Sci [Internet]. 1879;8(49):261–74. Available from: https://doi.org/10.1080/14786447908639684

75. Hell SW, Wichmann J. Breaking the diffraction resolution limit by stimulated emission: stimulated-emission-depletion fluorescence microscopy. Opt Lett [Internet]. 1994;19(11):780–2. Available from: http://www.osapublishing.org/ol/abstract.cfm?URI=ol-19-11-780

76. Guerra JM. Super-resolution through illumination by diffraction-born evanescent waves. Appl Phys Lett. 1995;66(26):3555–7.

77. Vicidomini G, Moneron G, Han KY, Westphal V, Ta H, Reuss M, et al. Sharper low-power STED nanoscopy by time gating. Nat Methods. 2011 Jul;8(7):571–5.

78. Moffitt JR, Osseforth C, Michaelis J, Patterson H, Sougrat R, Lindwasser OW, et al. Time-gating improves the spatial resolution of STED microscopy. Opt Express, Vol 19, Issue 5, pp 4242-4254 [Internet]. 2011 Feb 28 [cited 2022 Feb 28];19(5):4242–54. Available from: https://opg.optica.org/viewmedia.cfm?uri=oe-19-5-4242&seq=0&html=true

79. Schwentker MA, Bock H, Hofmann M, Jakobs S, Bewersdorf J, Eggeling C, et al. Wide-field subdiffraction RESOLFT microscopy using fluorescent protein photoswitching. Microsc Res Tech [Internet]. 2007 Mar 1 [cited 2022 Feb 28];70(3):269–80. Available from: https://onlinelibrary.wiley.com/doi/full/10.1002/jemt.20443

80. Cremer C, Heintzmann R, Jovin TM. Saturated patterned excitation microscopy—a concept for optical resolution improvement. JOSA A, Vol 19, Issue 8, pp 1599-1609 [Internet]. 2002 Aug 1 [cited 2022 Feb 28];19(8):1599–609. Available from: https://opg.optica.org/viewmedia.cfm?uri=josaa-19-8-1599&seq=0&html=true

81. Hoyer P, Medeiros G De, Norlin N, Besir C, Hanne J, Engelhardt J, et al. Breaking the diffraction limit of light-sheet fluorescence microscopy by RESOLFT. 2016;1–5.

82. von Diezmann A, Shechtman Y, Moerner WE. Three-dimensional localization of single molecules for super-resolution imaging and single-particle tracking. Chem Rev. 2017;117(11):7244–75.

83. Hell SW. Far-Field Optical Nanoscopy. Science (80-) [Internet]. 2007 May 25;316(5828):1153 LP-1158. Available from: http://science.sciencemag.org/content/316/5828/1153.abstract

84. Nienhaus K, Ulrich Nienhaus G. Fluorescent proteins for live-cell imaging with super-resolution. Chem Soc Rev [Internet]. 2014;43(4):1088–106. Available from: http://dx.doi.org/10.1039/C3CS60171D

85. Rust MJ, Bates M, Zhuang X. Sub-diffraction-limit imaging by stochastic optical reconstruction microscopy (STORM). Nat Methods [Internet]. 2006;3(10):793–6. Available from: https://doi.org/10.1038/nmeth929

86. Mortensen KI, Churchman LS, Spudich JA, Flyvbjerg H. Optimized localization analysis for single-molecule tracking and super-resolution microscopy. Nat Methods [Internet]. 2010;7(5):377–81. Available from: https://doi.org/10.1038/nmeth.1447

87. Cella Zanacchi F, Lavagnino Z, Faretta M, Furia L, Diaspro A. Light-Sheet Confined Super-Resolution Using Two-Photon Photoactivation. PLoS One [Internet]. 2013 Jul 2 [cited 2022 Feb 28];8(7):e67667. Available from: https://journals.plos.org/plosone/article?id=10.1371/journal.pone.0067667

88. Lemons RA, Quate CF. Lemons and Calvin F. Quate Stanford University Stanford,. 1973;18–21.

89. Strohm EM, Moore MJ, Kolios MC. Single Cell Photoacoustic Microscopy: A Review. IEEE J Sel Top Quantum Electron. 2016;22(3).

90. Callis JB, Parson WW, Gouterman M. Fast changes of enthalpy and volume on flash excitation of Chromatium chromatophores. Biochim Biophys Acta - Bioenerg [Internet]. 1972;267(2):348–62. Available from: https://www.sciencedirect.com/science/article/pii/0005272872901223

91. Arata H, Parson WW. Enthalpy and volume changes accompanying electron transfer from P-870 to quinones in Rhodopseudomonas sphaeroides reaction centers. Biochim Biophys Acta. 1981 Jun;636(1):70–81.

92. Patel CKN, Tam AC. Pulsed optoacoustic spectroscopy of condensed matter. Rev Mod Phys [Internet]. 1981;53(3):517–50. Available from:

https://link.aps.org/doi/10.1103/RevModPhys.53.517

93. Yao D, Maslov K, Wang L V. Photoacoustic measurement of the Grüneisen parameter of tissue Photoacoustic measurement of the Grüneisen parameter of tissue. 2014;

94. Yang J-M, Favazza C, Chen R, Yao J, Cai X, Maslov K, et al. Simultaneous functional photoacoustic and ultrasonic endoscopy of internal organs in vivo. Nat Med [Internet]. 2012;18(8):1297–302. Available from: https://doi.org/10.1038/nm.2823

95. Wang L V, Yao J. A practical guide to photoacoustic tomography in the life sciences. Nat Methods [Internet]. 2016;13(8):627–38. Available from: https://doi.org/10.1038/nmeth.3925

96. Wang L V. Multiscale photoacoustic microscopy and computed tomography. Nat Photonics [Internet]. 2009;3(9):503–9. Available from: https://doi.org/10.1038/nphoton.2009.157

97. Daft CMW, Briggs GAD, O'Brien WD. Frequency dependence of tissue attenuation measured by acoustic microscopy. J Acoust Soc Am [Internet]. 1989 May 1;85(5):2194–201. Available from: https://doi.org/10.1121/1.397868

98. Yu H. Scanning acoustic microscopy for material evaluation. Appl Microsc [Internet]. 2020;50(1):25. Available from: https://doi.org/10.1186/s42649-020-00045-4

99. Yao J, Wang L V. Photoacoustic microscopy. Laser Photonics Rev. 2013;7(5):758–78.

100. Song W, Zheng W, Liu R, Lin R, Huang H, Gong X, et al. Reflection-mode in vivo photoacoustic microscopy with subwavelength lateral resolution. Biomed Opt Express [Internet]. 2014;5(12):4235–41. Available from: http://www.osapublishing.org/boe/abstract.cfm?URI=boe-5-12-4235

101. Danielli A, Maslov K, Garcia-Uribe A, Winkler AM, Li C, Wang L, et al. Label-free photoacoustic nanoscopy. J Biomed Opt. 2014 Aug;19(8):86006.

102. Calasso IG, Craig W, Diebold GJ. Photoacoustic Point Source. Phys Rev Lett [Internet]. 2001 Apr;86(16):3550–3. Available from: https://link.aps.org/doi/10.1103/PhysRevLett.86.3550

103. Kim J, Kim JY, Jeon S, BAIK JW, Cho SH, Kim C. Super-resolution localization photoacoustic microscopy using intrinsic red blood cells as contrast absorbers. Light Sci Appl [Internet]. 2019;8(1):103. Available from: https://doi.org/10.1038/s41377-019-0220-4

104. Vilov S, Arnal B, Hojman E, Eldar YC, Katz O, Bossy E. Super-resolution photoacoustic

and ultrasound imaging with sparse arrays. Sci Rep [Internet]. 2020;10(1):4637. Available from: https://doi.org/10.1038/s41598-020-61083-2

105. van Raaij ME, Lee M, Chérin E, Stefanovic B, Foster FS. Femtosecond photoacoustics: integrated two-photon fluorescence and photoacoustic microscopy. In: Oraevsky AA, Wang L V, editors. Photons Plus Ultrasound: Imaging and Sensing 2010 [Internet]. SPIE; 2010. p. 543–8. Available from: https://doi.org/10.1117/12.841021

106. Lee S-Y, Lai Y-H, Huang K-C, Cheng Y-H, Tseng T-F, Sun C-K. In vivo sub-femtoliter resolution photoacoustic microscopy with higher frame rates. Sci Rep. 2015 Oct;5:15421.

107. Murray TW, Haltmeier M, Berer T, Leiss-Holzinger E, Burgholzer P. Super-resolution photoacoustic microscopy using blind structured illumination. Optica [Internet]. 2017;4(1):17–22. Available from: http://www.osapublishing.org/optica/abstract.cfm?URI=optica-4-1-17

108. Amjadian M, Mostafavi SM, Chen J, Kavehvash Z, Zhu J, Wang L. Super-Resolution Photoacoustic Microscopy Using Structured-Illumination. IEEE Trans Med Imaging. 2021 Sep;40(9):2197–207.

109. Yao J, Wang L V. Sensitivity of photoacoustic microscopy. Photoacoustics. 2014 Jun;2(2):87–101.

110. Winkler AM, Wang L V, Winkler AM, Maslov K, Wang L V. Noise-equivalent sensitivity of photoacoustics Noise-equivalent sensitivity of photoacoustics. 2013;

111. Bartlome R, Kaučikas M, Sigrist MW. Modulated resonant versus pulsed resonant photoacoustics in trace gas detection. Appl Phys B [Internet]. 2009;96(2):561–6. Available from: https://doi.org/10.1007/s00340-009-3572-2

112. Maslov K, Wang L V. Photoacoustic imaging of biological tissue with intensity-modulated continuous-wave laser. 2008;13(April 2008):1–5.

113. Braun SG, Ewins DJ, Rao SS, Leissa AW. Encyclopedia of Vibration: Volumes 1, 2, and 3. Appl Mech Rev. 2002;55(3):B45--B45.

114. Oraevsky AA, Karabutov AA. Ultimate sensitivity of time-resolved optoacoustic detection. In: Oraevsky AA, editor. Biomedical Optoacoustics [Internet]. SPIE; 2000. p. 228–39. Available from: https://doi.org/10.1117/12.386326

115. Rhyne T. Characterizing ultrasonic transducers using radiation efficiency and reception noise figure. IEEE Trans Ultrason Ferroelectr Freq Control. 1998;45:559–66.

116. Tan Z, Tang Z, Wu Y, Liao Y, Dong W, Guo L. Multimodal subcellular imaging with microcavity photoacoustic transducer. Opt Express [Internet]. 2011;19(3):2426–31. Available from: http://www.osapublishing.org/oe/abstract.cfm?URI=oe-19-3-2426

117. Tan Z, Liao Y, Wu Y, Tang Z, Wang RK. Photoacoustic microscopy achieved by microcavity synchronous parallel acquisition technique. Opt Express. 2012 Feb;20(5):5802–8.

118. Mattison SP, Applegate BE. Simplified method for ultra high-resolution photoacoustic microscopy via transient absorption. Opt Lett [Internet]. 2014;39(15):4474–7. Available from: http://www.osapublishing.org/ol/abstract.cfm?URI=ol-39-15-4474

119. Hai P, Yao J, Maslov KI, Zhou Y, Wang L V. Near-infrared optical-resolution photoacoustic microscopy. Opt Lett [Internet]. 2014;39(17):5192–5. Available from: http://www.osapublishing.org/ol/abstract.cfm?URI=ol-39-17-5192

120. Karu TI. Multiple roles of cytochrome c oxidase in mammalian cells under action of red and IR-A radiation. IUBMB Life. 2010 Aug;62(8):607–10.

121. Zhang C, Zhang YS, Yao D-K, Xia Y, Wang L V. Label-free photoacoustic microscopy of cytochromes. Vol. 18, Journal of biomedical optics. 2013. p. 20504.

122. Kim H, Baik JW, Kim JY, Jeon S, Son M, Byun K, et al. Label-free photoacoustic expansion histopathology with enhanced temporal and spatial resolution. In: Oraevsky AA, Wang L V, editors. Photons Plus Ultrasound: Imaging and Sensing 2021 [Internet]. SPIE; 2021. p. 39–44. Available from: https://doi.org/10.1117/12.2577203

123. Yao D-K, Chen R, Maslov K, Zhou Q, Wang L V. Optimal ultraviolet wavelength for in vivo photoacoustic imaging of cell nuclei. J Biomed Opt. 2012 May;17(5):56004.

124. Baik JW, Kim H, Son M, Choi J, Kim KG, Baek JH, et al. Intraoperative Label-Free Photoacoustic Histopathology of Clinical Specimens. Laser Photon Rev [Internet]. 2021 Oct 1;15(10):2100124. Available from: https://doi.org/10.1002/lpor.202100124

125. Pan D, Kim B, Wang L V, Lanza GM. A brief account of nanoparticle contrast agents for photoacoustic imaging. Wiley Interdiscip Rev Nanomed Nanobiotechnol. 2013;5(6):517–43.

126. Jokerst J V, Gambhir SS. Molecular imaging with theranostic nanoparticles. Acc Chem Res. 2011 Oct;44(10):1050–60.

127. Strohm EM, Moore MJ, Kolios MC. High resolution ultrasound and photoacoustic imaging of single cells. Photoacoustics [Internet]. 2016;4(1):36–42. Available from:

http://dx.doi.org/10.1016/j.pacs.2016.01.001

128. Wang Y, Wang L V. Förster resonance energy transfer photoacoustic microscopy. J Biomed Opt [Internet]. 2012;17(8):1–6. Available from: https://doi.org/10.1117/1.JBO.17.8.086007

129. Wang Y, Hu S, Maslov K, Zhang Y, Xia Y, Wang L V. In vivo integrated photoacoustic and confocal microscopy of hemoglobin oxygen saturation and oxygen partial pressure. Opt Lett [Internet]. 2011 Apr;36(7):1029–31. Available from: http://www.osapublishing.org/ol/abstract.cfm?URI=ol-36-7-1029

130. Wang Y, Maslov K, Kim C, Hu S, Wang L V. Integrated photoacoustic and fluorescence confocal microscopy. IEEE Trans Biomed Eng. 2010 Oct;57(10):2576–8.

131. Liu C, Gong X, Lin R, Liu F, Chen J, Wang Z, et al. Advances in Imaging Techniques and Genetically Encoded Probes for Photoacoustic Imaging. Theranostics [Internet]. 2016;6:2414–30. Available from: https://www.thno.org/v06p2414.htm

132. Li L, Hsu H-C, Verkhusha V V, Wang L V, Shcherbakova DM. Multiscale Photoacoustic Tomography of a Genetically Encoded Near-Infrared FRET Biosensor. Adv Sci [Internet]. 2021;8(21):2102474. Available from: https://onlinelibrary.wiley.com/doi/abs/10.1002/advs.202102474

133. Yao J, Kaberniuk AA, Li L, Shcherbakova DM, Zhang R, Wang L, et al. Multiscale photoacoustic tomography using reversibly switchable bacterial phytochrome as a near-infrared photochromic probe. Nat Methods [Internet]. 2016;13(1):67–73. Available from: https://doi.org/10.1038/nmeth.3656

134. Shcherbakova DM, Baloban M, Pletnev S, Malashkevich VN, Xiao H, Dauter Z, et al. Molecular Basis of Spectral Diversity in Near-Infrared Phytochrome-Based Fluorescent Proteins. Chem Biol. 2015 Nov;22(11):1540–51.

135. Shinoda H, Ma Y, Nakashima R, Sakurai K, Matsuda T, Nagai T. Acid-Tolerant Monomeric GFP from Olindias formosa. Cell Chem Biol. 2018 Mar;25(3):330–338.e7.

136. Dale, Jeremy W. ; Schantz, Malcolm von ; Plant N. Dai geni ai genomi : principi e applicazioni della tecnologia del DNA ricombinante. 2013.

137. Dale J, Van Schantz M. Basic Molecular Biology. In: From Genes to Genomes [Internet]. John Wiley & Sons, Ltd; 2002. p. 5–20. Available from: https://onlinelibrary.wiley.com/doi/abs/10.1002/0470856912.ch2

138. Dale J, Van Schantz M. Polymerase Chain Reaction (PCR). In: From Genes to Genomes [Internet]. John Wiley & Sons, Ltd; 2002. p. 143–60. Available from:

https://onlinelibrary.wiley.com/doi/abs/10.1002/0470856912.ch9

139. Cox DLNMM. I principi di biochimica di Lehninger. 2014.

140. Murakoshi H, Lee S-J, Yasuda R. Highly sensitive and quantitative FRET-FLIM imaging in single dendritic spines using improved non-radiative YFP. Brain Cell Biol. 2008 Aug;36(1–4):31–42.

141. Porath J. Immobilized metal ion affinity chromatography. Protein Expr Purif [Internet]. 1992 Aug 1 [cited 2018 Oct 19];3(4):263–81. Available from: https://www.sciencedirect.com/science/article/pii/104659289290001D?via%3Dihub

142. Pennacchietti F, Losi A, Xu X, Zhao K, Gärtner W, Viappiani C, et al. Photochromic conversion in a red/green cyanobacteriochrome from Synechocystis PCC6803: quantum yields in solution and photoswitching dynamics in living E. coli cells. Photochem Photobiol Sci [Internet]. 2015;14(2):229–37. Available from: http://dx.doi.org/10.1039/c4pp00337c

143. Steel DG, Guenther BD. Encyclopedia of Modern Optics. First. Elsevier, editor. 2004.

144. Losi A, Bonomi HR, Michael N, Tang K, Zhao K-H. Time-Resolved Energetics of Photoprocesses in Prokaryotic Phytochrome-Related Photoreceptors. Photochem Photobiol. 2017 May;93(3):733–40.

145. Braslavsky SE, Heibel GE. Time-resolved photothermal and photoacoustic methods applied to photoinduced processes in solution. Chem Rev [Internet]. 1992 Sep 1;92(6):1381–410. Available from: https://pubs.acs.org/doi/abs/10.1021/cr00014a007

146. Small JR. Deconvolution analysis for pulsed-laser photoacoustics. Methods Enzymol. 1992;210:505–21.

147. Small JR, Libertini LJ, Small EW. Analysis of photoacoustic waveforms using the nonlinear least squares method. Biophys Chem. 1992 Jan;42(1):29–48.

148. Melton LA, Ni T, Lu Q. Photoacoustic calorimetry: a new cell design and improved analysis algorithms. Rev Sci Instrum [Internet]. 1989;60(10):3217–23. Available from: https://doi.org/10.1063/1.1140555

149. Brunker J, Yao J, Laufer J, Bohndiek SE. Photoacoustic imaging using genetically encoded reporters: a review. J Biomed Opt. 2017 Jul;22(7).

150. Mishra K, Fuenzalida-Werner JP, Ntziachristos V, Stiel AC. Photocontrollable Proteins for Optoacoustic Imaging. Anal Chem. 2019 May;91(9):5470–7.

151. Mishra K, Stankevych M, Fuenzalida Werner JP, Grassmann S., Gujrati V, Huang Y,

et al. Multiplexed whole-animal imaging with reversibly switchable optoacoustic proteins. Sci Adv. 2020;6(24).

152. Zhang J, Wu X-J, Wang Z-B, Chen Y, Wang X, Zhou M, et al. Fused-gene approach to photoswitchable and fluorescent biliproteins. Angew Chem Int Ed Engl. 2010 Jul;49(32):5456–8.

153. Zanini G, Korobchevskaya K, Deguchi T, Diaspro A. Label-Free Optical Nanoscopy of Single-Layer Graphene. 2019;

154. Instruments Z. Principles of lock-in detection and the state of the art Zurich Instruments. 2016.

155. Komuro Y, Kumada T, Ohno N, Foote KD, Komuro H. Chapter 15 - Migration in the Cerebellum. In: Rubenstein JLR, Rakic PBT-CM and F of NC, editors. Oxford: Academic Press; 2013. p. 281–97. Available from: https://www.sciencedirect.com/science/article/pii/B9780123972668000302

156. Purves D, Augustine GJ, Fitzpatrick D, Hall WC, LaMantia A-S, McNamara JO, et al., editors. Neuroscience, 4th ed. Neuroscience, 4th ed. Sunderland, MA, US: Sinauer Associates; 2008. p. xx, 857-xx, 857.

157. Wáng Y-XJ, Choi Y, Chen Z, Laurent S, Gibbs SL. Molecular Imaging: From Bench to Clinic. Biomed Res Int [Internet]. 2014;2014:357258. Available from: https://doi.org/10.1155/2014/357258

158. Parravicini J, Tomaselli A, Hasani E, Tomassini D, Manfredi N, Tartara L. Practical two-photon-absorption cross sections and spectra of eosin and hematoxylin. J Biophotonics [Internet]. 2020 Nov 1;13(11):e202000141. Available from: https://doi.org/10.1002/jbio.202000141

159. Albota MA, Xu C, Webb WW. Two-Photon Fluorescence Excitation Cross Sections of Biomolecular Probes from 690 to 960 nm. Appl Opt. 1998 Nov;37(31):7352–6.

160. Schneider M, Barozzi S, Testa I, Faretta M, Diaspro A. Two-Photon Activation and Excitation Properties of PA-GFP in the 720–920-nm Region. Biophys J [Internet]. 2005 Aug 20;89(2):1346–52. Available from: http://www.ncbi.nlm.nih.gov/pmc/articles/PMC1366619/

161. Keller PJ, Schmidt AD, Wittbrodt J, Stelzer EHK. Reconstruction of Zebrafish Early Embryonic Development by Scanned Light Sheet Microscopy. Sci (Washington, DC, U S). 2008;322(5904):1065.

162. Girkin JM, Carvalho MT. The Light-Sheet Microscopy Revolution. J Opt (Bristol, U K). 2018;20(5):53002.

163. Voleti V, Patel KB, Li W, Perez Campos C, Bharadwaj S, Yu H, et al. Real-Time Volumetric Microscopy of in Vivo Dynamics and Large-Scale Samples with SCAPE 2.0. Nat Methods. 2019;16(10):1054.

164. Chakraborty T, Chen B, Daetwyler S, Chang BJ, Vanderpoorten O, Sapoznik E, et al. Converting Lateral Scanning into Axial Focusing to Speed up Three-Dimensional Microscopy. Light Sci Appl. 2020;9(1):1.

165. Truong T V, Holland DB, Madaan S, Andreev A, Keomanee-Dizon K, Troll J V, et al. High-Contrast, Synchronous Volumetric Imaging with Selective Volume Illumination Microscopy. Commun Biol. 2020;3(1):1.

166. Wagner N, Norlin N, Gierten J, de Medeiros G, Balázs B, Wittbrodt J, et al. Instantaneous Isotropic Volumetric Imaging of Fast Biological Processes. Nat Methods. 2019;16(6):497.

167. Tomer R, Lovett-Barron M, Kauvar I, Andalman A, Burns VM, Sankaran S, et al. SPED Light Sheet Microscopy: Fast Mapping of Biological System Structure and Function. Cell. 2015;163(7):1796.

168. Olarte OE, Andilla J, Licea-Rodriguez J, Artigas D, Loza-Alvarez P. Light sheet microscopy with wavefront coding for fast volumetric imaging of biological samples. 2016 Conf Lasers Electro-Optics, CLEO 2016. 2016;1–2.

169. Quirin S, Peterka DS, Yuste R. Instantaneous Three-Dimensional Sensing Using Spatial Light Modulator Illumination with Extended Depth of Field Imaging. Opt Express. 2013;21(13):16007.

170. Fahrbach FO, Voigt FF, Schmid B, Helmchen F, Huisken J. Rapid 3D Light-Sheet Microscopy with a Tunable Lens. Opt Express. 2013;21(18):21010.

171. Duocastella M, Sancataldo G, Saggau P, Ramoino P, Bianchini P, Diaspro A. Fast Inertia-Free Volumetric Light-Sheet Microscope. ACS Photonics. 2017;4(7):1797.

172. Kang SY, Duocastella M, Arnold CB. Variable Optical Elements for Fast Focus Control. Nat Photonics. 2020;14(9):533.

173. Genchi L, Bucci A, Laptenok SP, Giammona A, Liberale C. Hadamard-transform spectral acquisition with an acousto-optic tunable filter in a broadband stimulated Raman scattering microscope. Opt Express [Internet]. 2021;29(2):2378–86. Available from: http://www.osapublishing.org/oe/abstract.cfm?URI=oe-29-2-2378

174. Ren Y, Wu J, Lai QTK, Lai HM, Siu DMD, Wu W, et al. Parallelized Volumetric Fluorescence Microscopy with a Reconfigurable Coded Incoherent Light-Sheet Array. Light Sci Appl. 2020;9(8):1.

175. Keller PJ, Schmidt AD, Wittbrodt J, Stelzer EHK. Reconstruction of zebrafish early embryonic development by scanned light sheet microscopy. Science (80-). 2008;322(5904):1065–9.

176. Trypogeorgos D, Harte T, Bonnin A, Foot C. Precise shaping of laser light by an acousto-optic deflector. 2013;21(21):8619–25.

177. Mohan K, Purnapatra SB, Mondal PP. Three dimensional fluorescence imaging using multiple light-sheet microscopy. PLoS One. 2014;9(6):1–8.

178. Dean KM, Roudot P, Welf ES, Pohlkamp T, Garrelts G, Herz J, et al. Imaging subcellular dynamics with fast and light-efficient volumetrically parallelized microscopy. Optica. 2017;4(2):263.

179. Duocastella M, Surdo S, Zunino A, Diaspro A, Saggau P. Acousto-optic systems for advanced microscopy. J Phys Photonics. 2021;3.

180. Martinez-Corral M, Hsieh PY, Doblas A, Sanchez-Ortiga E, Saavedra G, Huang YP. Fast Axial-Scanning Widefield Microscopy with Constant Magnification and Resolution. IEEE/OSA J Disp Technol. 2015;11(11):913–20.

181. McLeod E, Arnold CB. Mechanics and refractive power optimization of tunable acoustic gradient lenses. J Appl Phys. 2007;102(3):1–9.

182. Tomer R, Lovett-Barron M, Kauvar I, Andalman A, Burns VM, Sankaran S, et al. SPED Light Sheet Microscopy: Fast Mapping of Biological System Structure and Function. Cell. 2015;163(7):1796–806.

APPENDIX I: Development and characterization of a phase-plate

As we mentioned in **paragraph 3.4.1**, one strong requirement for deterministic super-resolution techniques such as RESOLFT and STED is the capability of generating a donut-shaped beam. Phase plates are generally used for this aim. Phase plates mainly work by generating a disruptive interference at the focus thanks to interference between two different media with different refractive indexes, generally air and a spin-coated polymer. This latter phase plate mainly used in STED/RESOLFT is a spiral one (vortex, **Figure AI-1**), but for our aims, we developed a linear (Halfmoon) wave plate for a SPIM setup.

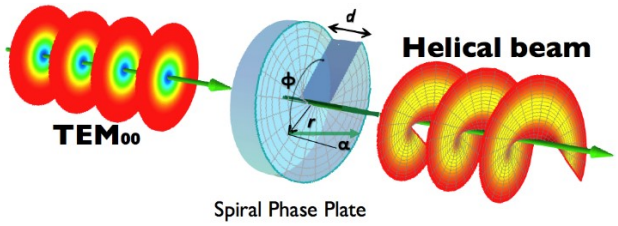

Figure AI-1. Diagram of m=1 mode of an optical vortex. It is evident in the donut shape of the beam. Image reproduced from Wikipedia, Creative Commons BY-SA 4.0

Production. We used a polymer (SU-8) spincoated onto a coverglass for the fabrication. We determined the thickness by the relation $\lambda/2(n-1)$, where n is the refractive index of the polymer (≈1.57). For a considered wavelength of 488 nm, the expected thickness is 428 nm.

Characterization. We characterized the phase-plate through a Shack-Hartmann Wavefront Sensor (Thorlabs, WFS40-7AR), a tool capable of providing information on wavefront shape and intensity distribution of incident beams. The sensor consists of a lenses array and a camera. A spot field is created on the camera when a wavefront enters the lenses array. The software analyzes and location of each spot to dynamically measure the wavefronts of laser sources or characterize the wavefront distortion caused by optical components (for example, the phase plate). As a result, we obtain the optical path of a wave traveling the medium. The optical path is the trajectory that a light ray follows as it propagates through an optical medium and is given by the product of the refractive index and the physical thickness of the step ($n \times \Delta h$). In **Figure AI-2**, we can see the 2D profile of the wavefront of raw data (**a**). In **Figure AI-2** (**b**), we plot the average projection along the axis, and the step is around 670 nm. It is possible to retrieve the physical thickness of the polymer's step (Δh=428) nm from the optical path. From simple geometry, we can retrieve the value of the phase displacement induced by the phase plate from the relation AI-1:

$$\Delta\phi = 2\pi(n-1)\Delta h/\lambda$$

Equation AI-1

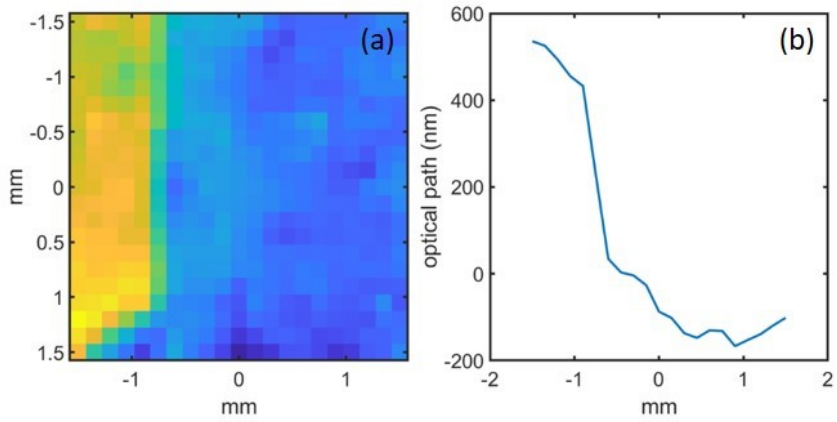

Figure AI-2. The waveform of a Gaussian beam after the phase plate. (**a**) 2D profile. (**b**) Average projection along the y-axis.

For a wavelength of 488 nm, the condition for a disruptive interference is a phase displacement of $\Delta\Phi{\sim}3.13$. For 532 nm and 647 nm excitation, the phase displacement is 2.87 and 2.32 (radian). It is possible to imagine the application also for green wavelengths. To test the functionality of the phase plate, we made a simple experiment: a laser beam, after space filtering, is sent to the phase plate on the interface between air and the polymer. A camera then acquires the output. In **Figure AI-3**, we report the results that show that the phase-plate works better in the blue/green region (**a-b**), while the red laser is less affected by its optical properties (**c**).

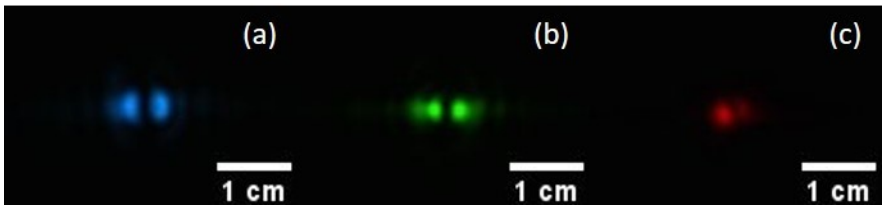

Figure AI-3. The output of a 488 nm (**a**), 532 nm (**b**) and 647 nm (**c**) beam crossing the phase plate.

As a last practical experiment, we implement the phase plate in a SPIM setup to generate a 1D STED beam. As we can see from the last figure (**Figure AI-4**), the phase plate works properly on a SPIM implementing a 488 nm excitation.

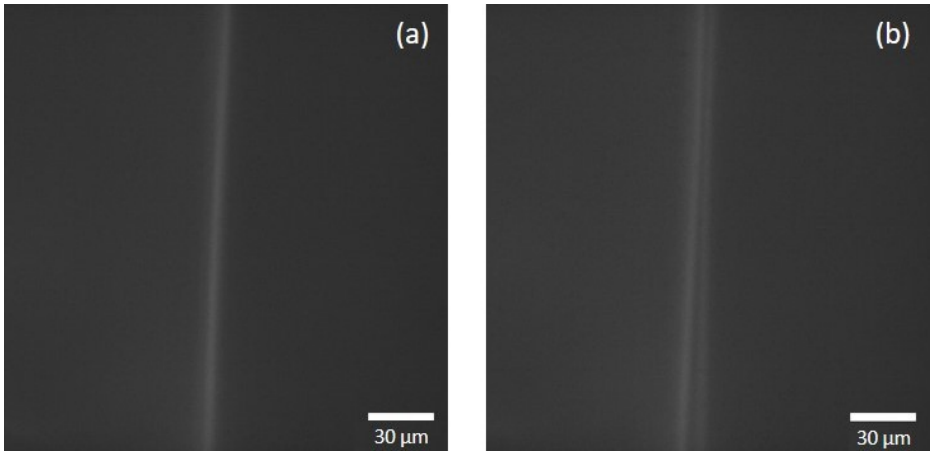

Figure AI-4. Images acquired in a SPIM setup. A single beam crosses the phase plate, placed in a focal plane. The objective focuses the light in a capillary containing fluoresceine embedded in agarose gel. (**a**) The phase plate is not placed. (**b**) The phase plate is placed.

APPENDIX II: Basis of Photolysis with transient absorption detection

We assume the protein solution undergoes a short laser pulse (1-20 s) with a wavelength close to or equal to the excitation maximum of the cis-anionic (B) or neutral-trans (A) state of the chromophore (**Figure AII-1**). This appendix is adapted from reference (35).

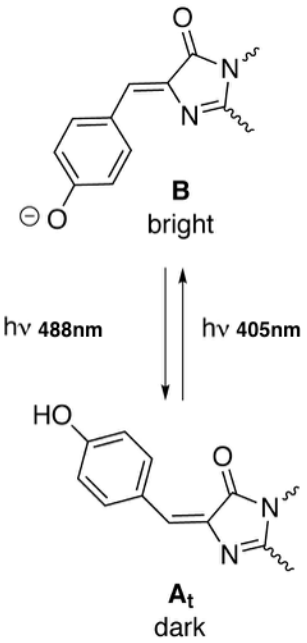

Figure AII-1. Isomerization scheme of chromophore 4-(p-hydroxybenzylidene)imidazolidin-5-one (HBI). Adapted with permission from reference (35). Copyright 2018 American Chemical Society.

We assume that the chromophore (and thus the protein) is all in one state at the beginning and that the pulses guide photoconversion in only one direction. In this condition, assuming a linear photo process, the instantaneous speed of photoconversion is:

$$dN/dt = \varphi \cdot \sigma \cdot N \cdot I$$

Equation AII-1

Where *N* is the number of molecules in the referred state, φ is the quantum yield of the process, σ is the absorption cross-section (cm^2), and I is the illumination intensity (photons/cm^2). We can rewrite **Equation AII-1** as a function of molar concentration:

$$dC/dt = 2303 \cdot \varphi \cdot \sigma \cdot C \cdot I$$

Equation AII-2

Here I is expressed in Einstein/cm^2. Integrating the **Equation AII-2** over a pulse duration of Δt we obtain:

$$\ln\left[1-\frac{\Delta C}{C^0}\right] = 2303 \cdot \varphi \cdot \varepsilon \cdot I \cdot \Delta t$$

Equation AII-3

Where ΔC and C^0 are, respectively, the variation of concentration and the initial concentration of the considered state. We convert the concentration to absorbance through Lambert-Beer Law:

$$\ln\left[1-\frac{\Delta A}{A^0}\right] = 2303 \cdot \varphi \cdot \varepsilon \cdot I \cdot \Delta t$$

Equation AII-4

We can rewrite the product of intensity and time as fluence ϕ, and we can rewrite the **Equation AII-4** for both photoprocesses (off->on and on->off) separately:

$$\ln\left[1-\frac{\Delta A_B}{A_B^0}\right] = 2303 \cdot \varphi_{off} \cdot \varepsilon \cdot \phi$$

Equation AII-5

$$\ln\left[1-\frac{\Delta A_A}{A_A^0}\right] = 2303 \cdot \varphi_{on} \cdot \varepsilon \cdot \phi$$

Equation AII-6

The target state may be back converted to the beginning form during the photoconversion process. That means that the **Equation AII-5** and **Equation AII-6** are valid only during the first stages of the process. Increasing the pulse duration, photoconversion tends to a photostationary state for which the global speed of the process tends to zero and zero is also the apparent photoconversion quantum yield. Flash-Photolysis measurements bring then to nonlinear behavior of $\ln[1-\Delta A/A_0]$ *vs*. fluence for fluence over a certain threshold. Photoconversion quantum yield is then calculated at the beginning of the graph, where back photoconversion is negligible. For both proteins were used 488 nm pulses from 0.1 s to 20 s to generate the *on* the state. The *off*-state is then recovered through a 405 nm diode laser.